CHALMERS
UNIVERSITY OF TECHNOLOGY

Soft Model Approximation of Microwave Scattering Properties of Ice Particles

Master's thesis in Earth and Space Sciences

MARYAM JAMALI

Department of Earth and Space Sciences
CHALMERS UNIVERSITY OF TECHNOLOGY
Gothenburg, Sweden 2015

MASTER'S THESIS

Soft Model Approximation of Microwave Scattering Properties of Ice Particles

MARYAM JAMALI

Department of Earth and Space Sciences
Global Environmental Measurements and Modelling Group
CHALMERS UNIVERSITY OF TECHNOLOGY
Gothenburg, Sweden 2015

Soft Model Approximation of Microwave Scattering Properties of Ice Particles
MARYAM JAMALI

Supervisor: PATRICK ERIKSSON

Master's Thesis 2015
Department of Earth and Space Sciences
Global Environmental Measurements and Modelling Group
Chalmers University of Technology
SE-412 96 Gothenburg
Telephone +46 31 772 1000

Cover: Examples of ice paricles (courtesy of Alexey Kljatov).
Typeset in LaTeX
Gothenburg, Sweden 2015

Soft Model Approximation of Microwave Scattering Properties of Ice Particles
MARYAM JAMALI
Department of Earth and Space Sciences
Chalmers University of Technology

Abstract

Clouds consisting of ice particles have a crucial role in our climate system and profoundly influence the Earth's radiation. However, these clouds are poorly constrained in climate models mainly due to uncertainties associated with estimation of their ice mass. It has been investigated by several studies that the combined microwave millimeter/submillimeter spectral region is suitable for observing the mass of ice clouds. One of the major uncertainty sources of the microwave ice mass estimation is that the shape of ice particles is poorly known. It has been shown by several studies that ice particles can take on extremely variable irregular shapes. It is therefore necessary to find shape models that can approximate and simplify the reality. Two common simple shape models frequently used are spheres and spheroids. They can be either solid (consisting of pure ice) or soft (consisting of a homogeneous mixture of ice and air).

This thesis is concerned with examining the applicability of the simple models in estimation of ice mass across the microwave spectral region. The focus is put on soft models. Three databases consisting of optical properties of some randomly oriented non-spherical ice particles and aggregates are considered as reference. The practical objective is to determine microphysical characteristics (i.e., shape, volume or mass fraction of air, and refractive index) of a soft model that mimics average optical properties of the reference data across all microwave frequencies from 90 to 874 GHz and size parameters (x) up to 6.

It is found that the volume air fraction of a soft model should vary with both size and frequency to give the best fit of the reference data. It is therefore impossible to define a soft model with a single air fraction working in a broad range of frequencies and particle sizes. It is also demonstrated that determining the volume air fraction based on size-density parameterisations results in underestimation of mean optical properties at larger size parameters ($x > 0.5$). Furthermore, it is concluded that applying the Maxwell Garnett mixing rule with ice as inclusion and air as matrix media (see section 3.4) underestimates the imaginary parts of refractive index of the soft models at lower size parameters ($x < 1$).

Overall, it is concluded that soft models can be tuned to give proper results over a narrow range of frequencies, but such a model lose its accuracy over other range of frequencies. One alternative approach to soft models is applying a sector-like snowflake model to represent the mean optical properties of the reference data. This was suggested by Geer and Baordo [2014] and confirmed by Eriksson *et al.* [2014].

Acknowledgements

First of all I would like to thank my supervisor, Patrick Eriksson, for giving the opportunity to work on such an interesting and challenging cloud remote sensing project. I am very grateful for his patience and the contentious support and guidance he has provided during this project. Further, I would like to extend my gratitude to Prof. Michael Kahnert for his invaluable comments throughout the project.

Many thanks also go out to all members of the Global Environmental Measurements and modelling group. Especially Ole Martin Christensen, Maryam Khosravi and Oscar Isoz that aside from being helpful have also encouraged me to go forward. Also, I would like to thank my dear friend Shayan Rahat for his helpful feedback on my report.

Lastly yet mostly, I would like to thank my husband, Hamed, who always cheer me up by his love, kindness and support.

Maryam Jamali
Gothenburg, February 2015

Contents

1 Introduction

Clouds are crucial components of the climate system and have a strong impact on the Earth's energy budget. They reflect incoming shortwave solar radiation and absorb outgoing longwave terrestrial radiation, and hence they have both negative (cooling) and positive (heating) impacts [Harries, 2000]. The magnitude and sign of the cloud radiative impact depend highly on the cloud's horizontal extent, vertical position, and microphysical properties. According to the IPCC's fifth assessment report, 'Climate models now include more cloud and aerosol processes, and their interactions, than at the time of the AR4 (IPCC's Fourth Assessment Report), but there remains low confidence in the representation and quantification of these processes in models'. Therefore, there is a strong demand for a better representation of clouds in the climate models.

To improve the global climate models, proper observations of clouds are required. Clouds can be observed either through remote sensing techniques or in-situ measurements. However, good spatial coverage can be achived only by polar orbiting, satellite-borne, remote-sensing instruments. In many climate models the radiative impact of clouds is represented as a function of their mass content. It has been suggested by Evans and Stephens [1995] and Buehler *et al.* [2007] that the combined microwave millimeter/submillimeter spectral region is suitable for retrieving the mass of clouds (see section 1.3). At these wavelengthes, cloud droplets or particles are large enough to scatter the radiation in the Mie regime (The reader is referred to Mishchenko *et al.* [2002] for details). In this regime, the shape of each particle should be known to determine its optical properties, and accordingly avoid a related mass estimation error (see section 1.1).

The radiative impact of clouds that consist of pure liquid water droplets can be estimated fairly well since the shape of liquid particles is well known. However, there are large uncertainties surrounding clouds consisting partially or entirely of ice particles. These type of clouds are referred to as ice clouds. The main uncertainty surrounding ice clouds arises from the fact that ice particles can take on highly variable shapes.

The aim of this study is to enhance the mass estimation of ice clouds by examining some simple shape models that represent mean optical properties of ice particles more realistically. Although a cloud may consist of any mixture of solid, gas, and liquid phases, this study is only concerned with ice clouds in the pure ice phase or a mixture of ice and air. Investigating the mixed phase clouds is more complex and beyond the scope of this project.

1.1 Mass retrieval

The mass of clouds can not be measured directly by observation and an inversion process (that is, a so-called retrieval) is required. Mass retrieval of ice clouds is a complex process. The mass of ice clouds is commonly given in terms of IWC (Ice Water Content; the total mass of ice in a unit volume of cloud) or IWP (Ice Water Path; the column integrated IWC through the depth of the cloud). Diagram 1.1 is a schematic representation of a IWC retrieval model. As shown in this diagram, there are observations of cloud signals (CS_{observed}) and the goal is to simulate those observations (calculate $CS_{\text{simulated}}$). In this retrieval model, firstly, initial assumptions of IWC, particle size distribution (PSD), and microphysical state of particles (i.e. phase (refractive index), size, shape, and orientation) are required. Then, single scattering properties of particles are calculated through solving the Maxwell equation, either by the Lorenz-Mie theory, T-Matrix method, or by DDA method, that are explained in the dedicated chapter later. Afterwards, to calculate bulk scattering properties of a volume of the cloud, the single scattering properties are integrated over the given PSD. The next step is deriving the cloud signal ($CS_{\text{simulated}}$) through the radiative transfer equation, that is briefly described in section 5.2. Then, this simulated signal ($CS_{\text{simulated}}$) is iteratively compared to the observed one (CS_{observed}) by adjusting the IWC value. The principle of this retrieval algoritem is to minimise the differences between the simulated and the observed CS. As soon as $|CS_{\text{simulated}} - CS_{\text{observed}}|$ fits within the desired accuracy (ε), the IWC is retrieved.

The accuracy of the mass retrieval, in term of IWC, depends on the accuracy of the background assumptions. For instance, one of the retrieval uncertainties is connected to unavoidable assumptions on the PSD. Furthermore, the limitation of the radiative transfer equation directly affects the reliability of the results. A major error source of mass retrieval is associated with uncertain assumptions on physical properties of particles. In particular, one of the physical properties that we have a significant lack of knowledge about is particle shape. Therefore, to enhance the accuracy of the retrieved IWC, assumptions of particle shapes should be improved. This study is concerned with finding the best simple assumption on particle shape which leads to likely accurate estimation of ice mass.

1.2 Problem description and solutions

Several studies, like the ones by Heymsfield and Miloshevich [1995, 2003], reveal that ice particles can take on highly variable and complex shapes depending on the conditions they are formed in. The left column of Figure 1.2 shows an example of different ice particle shapes as a function of particle size and temperature for a type of ice cloud (cirrus cloud), that were measured by air craft. Generally, the simpler and more spherical shapes tend to exist at cloud-top, while more complicated aggregates are present towards cloud-bottom due to ice crystals sedimentation. Heymsfield and Miloshevich [1995] showed that ice particle shapes can vary considerably even within two

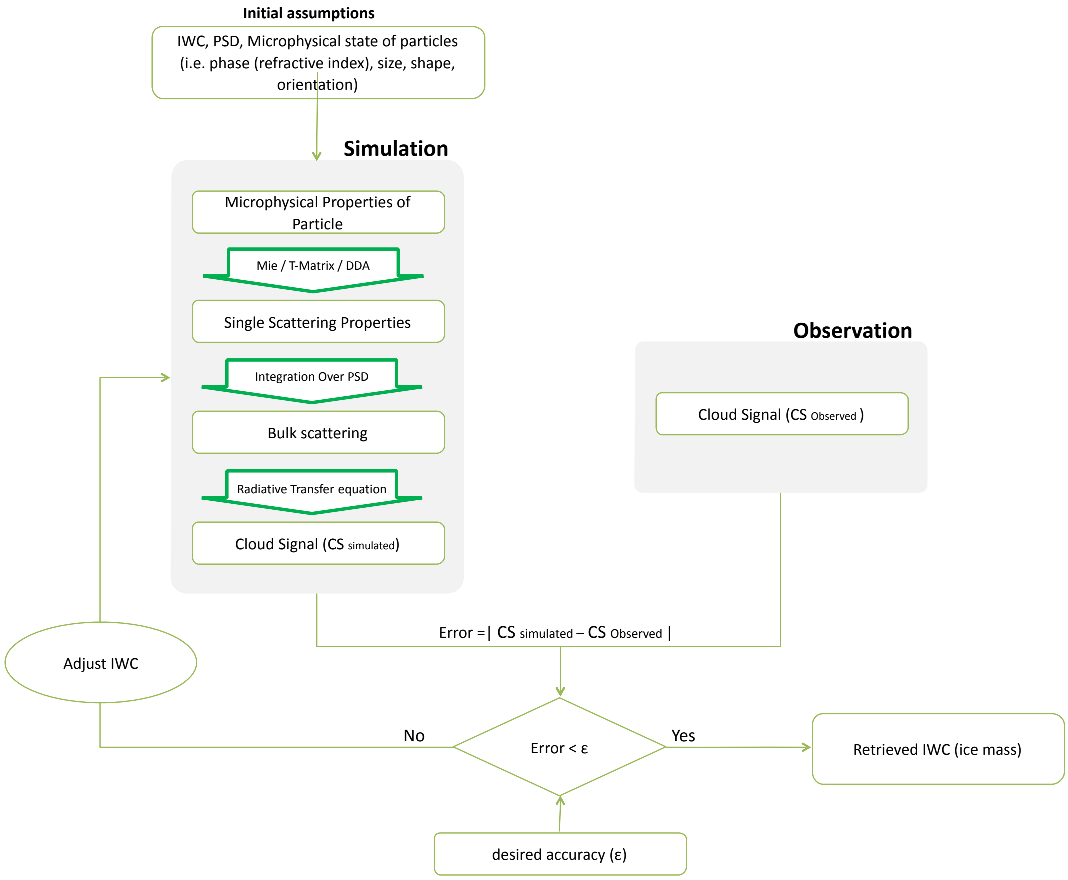

Figure 1.1: A schematic diagram of a naive ice cloud mass retrieval.

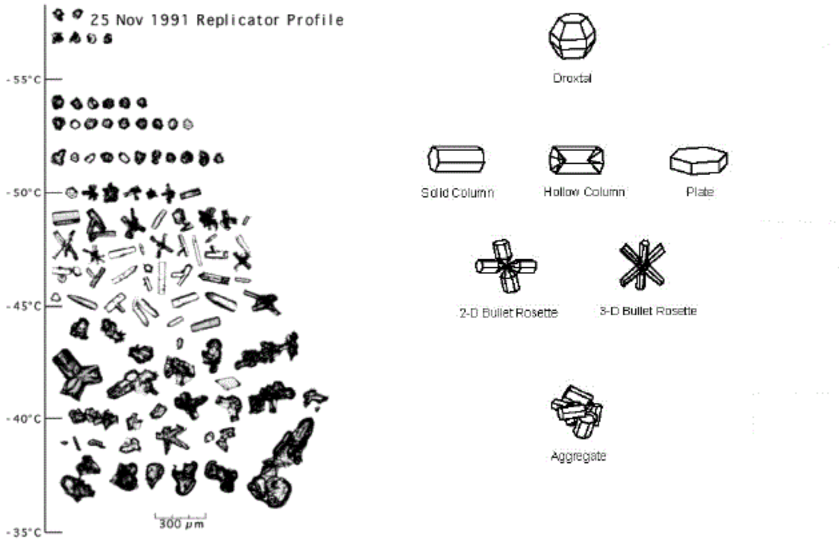

Figure 1.2: (left column) A vertical sampling of crystals and aggregates collected by a replicator during the First ISCCP field experiment. (right column) The suggested ice crystal geometries to estimate the light scattering and radiative transfer of cirrus clouds. Figure taken from http://www.ssec.wisc.edu/ baum/Cirrus/MidlatitudeCirrus.html

clouds with the same type. It is therefore not feasible to know the exact shape of each particle in ice clouds. However, in principle the shape of each particle should be known to avoid a related mass retrieval error.

To simulate the real ice particle shapes, some non-spherical geometries are suggested in the right column of Figure 1.2 (Yang *et al.* [2003]). Scattering properties of these simulated non-spherical ice particles can be estimated by solving the Maxwell equation numerically through the finite difference time domain (FDTD) or the discrete dipole approximation (DDA). The DDA [Draine and Flatau, 2000] is an accurate method to calculate the scattering properties of a particle with an arbitrary shape. The main advantage of this method is its flexibility to the geometry of the particle, but it is a computationally costly method (see section 5.1).

The DDA method has been used to compute the scattering properties for some particle shapes and sizes at different frequencies and temperatures, and these results are available as databases. These databases are likely the most accurate representative of scattering properties of the real ice particles. The properties of these DDA databases are presented in chapter 6.

To simplify the single scattering computations, some simple shape models have been frequently applied to represent real ice particles. From the perspective of mass retrieval, these simple models are spheres or spheroids that have the same mass as corresponding real ice particles. These simple models are treated to consist of pure ice (referred as solid models) or a homogeneous mixture of ice and air (referred as soft models). The main advantage of these simple models is that

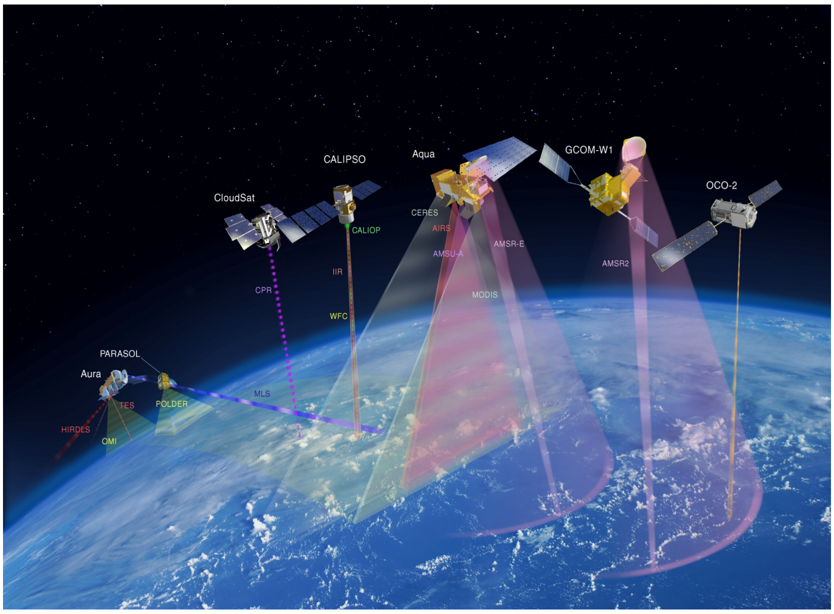

Figure 1.3: Polar orbiting satellites, called A-train, flying with a minutes intervals in a sun synchronous orbit ©NASA.

their scattering properties can be calculated by models such as the Lorenz-Mie theory and T-matrix which are computationally efficient methods contrasted with the DDA. However, the validity of theses simple shape models for retrieving the ice mass, needs to be tested thoroughly.

In this study, to assess the accuracy of these simple shape models for retrieving the mass , we consider three publicly available DDA databases as references. Then, the physical properties of a simple shape model (sphere/spheroid, solid/soft) that can mimic the average scattering properties of the three considered reference data over a range of frequencies and size particles, is determined.

1.3 Cloud ice mass remote sensing

There are plenty of satellites, working in the microwave, optical, and infrared wavelength regions. Figure 1.3 shows the international Afternoon Constellation, called A-train, including precisely engineered satellites that make observations of clouds, aerosols, and atmospheric chemistry. Active instruments are aboard CALIPSO and CloudSat. AMSR, AMSU-A, CPR, and MLS measure in the microwave spectral region. Optical wavelengths are observed by POLDER, OMI, and OCO-2. MODIS and CERES are working at both optical and infrared wavelengths. IIR, AIRS, TES, and HIRDLS measure the atmosphere in the infrared spectral region.

Satellite-borne instruments operating in the visible and IR spectral region are not ideal to retrieve the bulk mass of ice clouds, because at these high frequencies radiation interacts mainly with small particles, carrying only a small fraction of the mass. However instruments operating in the IR region are able to retrieve the mass of thin clouds, and are also suited to observe cloud top altitude and provide information of humidity in the upper troposphere. The best frequencies to retrieve the mass of clouds should be millimeter/ submillimeter, partly due to good cloud penetration capability. The measured signal in millimeter/ submillimeter spectral region is mainly generated by the cloud ice particles that constitute a dominant fraction of the mass. Active and passive systems have their own pros and cons in estimating the ice mass. Radars (active instrument), such as CloudSAT and EarthCARE, have high vertical resolution, contrasted to their horizontal coverage. In short, inevitable assumptions about the PSD (particle size distribution) are needed in the active retrieval of ice mass. It has been suggested that a passive submillimeter microwave sensor is suitable to observe cloud ice mass (Evans and Stephens [1995]; Buehler *et al.* [2007]). These frequencies penetrate clouds and interact with particles consisting the bulk mass. Furthermore, an estimation of PSD can be obtained by combining observations at different frequencies and good spatial coverage can be provided with this kind of sensor. A first instrument of this type, dedicated to ice cloud observations, is planned: ICI (Ice Cloud Imager) on the Metop Second Generation satellites, with first planned launch 2020. Metop is the European set of polar orbiting weather satellites. During the closest years the activities focus on the airborne prototype ISMAR (International Sub Millimetre Airborne Radiometer). The ISMAR data will be used to develop retrieval algorithms for ICI.

1.4 Outline

The following study is divided into six chapters. Chapter 2 explains a list of the concepts essential for understanding of this thesis. Chapter 3 discusses the variables determining the physical properties of a simple shape model and explains how those variables are related. Chapter 4 is a literature survey, that reviews two soft models and clarifies how variables of Chapter 3 are derived. When all the required physical properties of a particle are determined, the next step is to compute its single scattering properties through different models, which is investigated in Chapter 5. Later on, a general explanation about relative importance of different components of the scattering properties, are reviewed. The major discussion of applying simple shape models to approximate the scattering properties of ice particles, is presented in Chapter 6. Finally, Chapter 7 presents the conclusions of this study and discusses the necessity of future work to be conducted.

This study formed the basis of the submitted manuscript (Eriksson *et al.* [2014]) that is attached in the appendix part. Eriksson *et al.* [2014] investigated the soft particle approximation (SPA) and proposed an alternative to the SPA, i.e., using a particle shape of the Liu database that can mimic the average optical properties of the DDA data. Eriksson *et al.* [2014] also presented radiative transfer simulations as a way of measuring the discrepancy between the reference DDA data and the SPA model and the proposed proxy particle shape.

2 Variables

This chapter provides a brief explanation of the variables that are used in the following chapters.

$\boldsymbol{d}_{\mathrm{e}}$: Mass equivalent diameter

The diameter of a mass-equivalent solid ice sphere is

$$d_{\mathrm{e}} = \sqrt[3]{\frac{6m}{\pi\rho_{\mathrm{ice}}}}, \tag{2.1}$$

where m is the particle's mass and ρ_{ice} is the ice density ($917\ \mathrm{kg\,m^{-3}}$).

$\boldsymbol{d}_{\mathrm{max}}$ and $\boldsymbol{d}_{\mathrm{short}}$: Maximum and minimum diameters

Maximum and minimum diameters are the maximum and minimum lengths of a particle, respectively.

$\boldsymbol{d}_{\mathrm{mean}}$: Mean diameter

Mean diameter of a particle was originally used by Brown and Francis [1995]. Hogan *et al.* [2012] defined the d_{mean} as:

$$d_{\mathrm{mean}} = \frac{d_{\mathrm{max}} + d_{\mathrm{short}}}{2}. \tag{2.2}$$

$\boldsymbol{\alpha}$: Axial ratio

It is defined as

$$\alpha = \frac{d_{\mathrm{max}}}{d_{\mathrm{short}}}, \tag{2.3}$$

which results in $\alpha \geq 1$.

$\boldsymbol{x}$: Size parameter

Size parameter is a dimensionless quantity, here throughout defined based on d_{e}

$$x = \frac{\pi d_{\mathrm{e}}}{\lambda}, \tag{2.4}$$

where λ is the wavelength.

C_{ext} : Extinction cross section

It is interpreted as the effective area of a particle presented to the incident beam, resulting in some of the beam being absorbed or scattered into other directions. In other words, C_{ext} is defined as the amount of electromagnetic energy which get extincted over the incoming electromagnetic flux intensity [Knoll, 2010]. The extinction is caused by both scattering and absorption of the electromagnetic energy, therefore:

$$C_{\text{ext}} = C_{\text{sca}} + C_{\text{abs}}, \tag{2.5}$$

where C_{sca} and C_{abs} are the scattering and absorption cross section, respectively. The cross section's SI unit is m^2.

C^I_{ext}, C^v_{ext}, and C^h_{ext} are the extinction cross sections when we consider the total intensity, vertical polarisation state, and horizontal polarisation state of the extincted radiation, respectively.

C_{bac} : Backscattering cross section

It is interpreted as the effective area of a particle presented to the incident beam, resulting in some of the beam being scattered into the backward direction. In other words, C_{bac} is the rate of scattering of the electromagnetic energy in the backward direction, divided by the incident electromagnetic energy flux over a complete sphere (i.e., $4\pi\, steradian$).

Q_{ext} : Extinction efficiency

It is here defined as the ratio of a particle's extinction cross section (C_{ext}) to the geometrical cross section of the equal-mass ice spherical particle

$$Q_{\text{ext}} = \frac{4C_{\text{ext}}}{\pi d_{\text{e}}^2}. \tag{2.6}$$

Regarding to equation 2.5, the Q_{ext} is:

$$Q_{\text{ext}} = Q_{\text{sca}} + Q_{\text{abs}}, \tag{2.7}$$

where Q_{sca} and Q_{abs} are the scattering and absorption efficiencies, respectively.

Q^I_{ext}, Q^v_{ext}, and Q^h_{ext} are the extinction efficiencies when we consider the total intensity, vertical polarisation state, and horizontal polarisation state, respectively.

Q_{bac} : Backscattering efficiency

It is here defined as the ratio of a particle's backscattering cross section (C_{bac}) to the geometrical cross section of the equal-mass ice spherical particle

$$Q_{\text{bac}} = \frac{4C_{\text{bac}}}{\pi d_{\text{e}}^2}. \tag{2.8}$$

g : Asymmetry parameter

The $(1,1)$ element of scattering matrix (**P** in equation 5.1), represents the phase function that shows the angular distribution of the scattered energy. The first Legendre moment of the phase function, is the asymmetry parameter, and it represents the degree of asymmetry of the angular scattering.

$$g = \frac{1}{2} \int_{0}^{\pi} cos\,\Theta\, P_{11}(\Theta)\, sin\,\Theta\, d\Theta, \tag{2.9}$$

while the phase function (P_{11}) is supposed to be normalised by the following condition

$$\frac{1}{2} \int_{0}^{\pi} P_{11}(\Theta)\, sin\,\Theta\, d\Theta \;=\; 1, \tag{2.10}$$

where Θ is the scattering angle.

The value of g varies between -1 and 1 and its interpretation is that $g > 0$ for particles that scatter mainly in the forward direction and $g < 0$ otherwise. The scattering is isotropic with respect to the plane perpendicular to the incident radiation, if $g = 0$. For details, the reader is referred to Thomas and Stamnes [2002].

ε_{eff} : Effective dielectric constant of a mixture

Dielectric constant (ε_{eff}) of a homogeneous mixture composed of media 1 (matrix) of dielectric constant ε_{mat} and media 2 (inclusion) of dielectric constant ε_{inc}.

n_{eff} : Effective refractive index of a mixture

Refractive index (n_{eff}) of a mixture composed of media 1 (matrix) and media 2 (inclusion).

ρ_{eff} : Effective density of a homogeneous mixture

Density of a homogeneous mixture composed of a number of distinct materials with mass and volume of m_{i} and v_{i}.

V_{eff} : Effective density of a mixture

Volume of a mixture composed of a number of distinct materials with mass and volume of m_{i} and v_{i}.

3 Simple shape models

An essential requirement to study the effect of ice clouds is the capability of calculation the single scattering properties of ice particles. The scattering and absorption properties of a single ice particle, depend on the particle's shape, size, orientation, refractive index and the frequency of radiation [Mishchenko *et al.*, 2002]. Therefore, different variables must be considered to parameterize the single scattering properties. As mentioned in chapter 1, ice particles are known to have highly varying shapes. They have different forms, such as hexagons, plates, columns or irregular aggregates. However, it is not feasible to represent the physical properties of each individual particle, the important aspect is if the combined scattering properties are sufficiently well covered. For computational reasons, this must be achieved by a relatively small set of particles having a shape for which is easy to calculate single scattering properties.

The most common simple model is to consider the non-spherical ice particles to be solid spheres. In this model, the solid spheres have the density of pure ice ($0.917\ \mathrm{g\,cm^{-2}}$) and the same mass as the corresponding non-spherical ice particle. This approach is applied in cloud ice retrievals based on limb sounding data [Rydberg *et al.*, 2009; Wu *et al.*, 2008]. The single scattering properties of this shape model are simply calculated by the computationally efficient Lorenz-Mie method (see section 5.1).

Another common simplified model is the "soft particle approximation" where a single non-spherical ice particle is approximated by a soft sphere or spheroid. Generally, a soft particle model is assumed to consist of ice and air that are mixed homogeneously, and the effective density (ρ_{eff}) of the particle is less than the density of the pure ice. This approach requires that ρ_{eff}, and hence the volume (or mass) fraction of air and the corresponding refractive index of the ice-air mixture are determined (see sections 3.2 and 3.3). The scattering properties of spheroids can be calculated by the T-matrix method [Mishchenko *et al.*, 1996] that is a computationally efficient method likewise the Lorenz-Mie one. A soft spheroid model is applied in e.g. Hogan *et al.* [2012] for radar retrievals of ice clouds. The physical properties of this soft model are discussed in section 4.1.

Figure 3.1 is a schematic drawing that shows how a non-spherical particle is approximated by a solid ice sphere (red circle), a soft sphere with a diameter of the particle's maximum dimension (d_{max}), and by a soft spheroid.

This chapter, firstly, presents some of the typical relationships between size and mass of ice

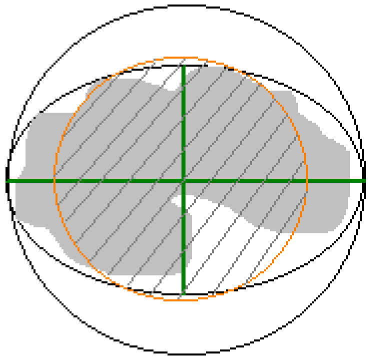

Figure 3.1: An irregular ice aggregate (grey area) that is approximated by a solid ice sphere (red circle), a soft sphere, and a spheroid. Perpendicular green lines are D_{max} and D_{short} of the spheroid.

particles. Later on it gives a general overview of the variables required to define the soft particle model.

3.1 Mass-size relationship

Deriving a relationship between the mass and size of the ice particles, has been studied since the early 20th century (e.g. Nakaya and Terada Jr [1935], Locatelli and Hobbs [1974], Mitchell *et al.* [1990], Brown and Francis [1995], Delanoë and Hogan [2010], , Baran *et al.* [2011a], and Delanoë *et al.* [2014]). Three examples on such mass-size relationships are

1) Brown and Francis [1995] :

$$\begin{aligned} m &= 480 d_{\text{mean}}^{3}; & d_{\text{mean}} &< 97 \cdot 10^{-6}\, m \\ m &= 0.0185 d_{\text{mean}}^{1.9}; & d_{\text{mean}} &\geq 97 \cdot 10^{-6}\, m \end{aligned} \tag{3.1}$$

2) Baran *et al.* [2011a] :

$$\begin{aligned} m &= 480 d_{\text{max}}^{3}; & d_{\text{max}} &\leq 100 \cdot 10^{-6}\, m \\ m &= 0.04 d_{\text{max}}^{2}; & d_{\text{max}} &> 100 \cdot 10^{-6}\, m \end{aligned} \tag{3.2}$$

3) Delanoë *et al.* [2014] :

$$\begin{aligned} m &= 407.604\, d_{\text{max}}^{2.91}; & d_{\text{max}} &\leq 10^{-4}\, m \\ m &= 0.546\, d_{\text{max}}^{1.91}; & 10^{-4} &< d_{\text{max}} \leq 3 \cdot 10^{-4}\, m \\ m &= 0.604\, d_{\text{max}}^{1.9}; & d_{\text{max}} &> 3 \cdot 10^{-4}\, m \end{aligned} \tag{3.3}$$

Note that some parameterisations use d_{mean}, while other use d_{max}. Based on in situ mass measurements of ice particles, Locatelli and Hobbs [1974] and Mitchell *et al.* [1990] presented different mass-size relationships as a function of d_{max} for some specific particle shapes (for more details see their Table 1).

Table 3.1: Effective density (ρ_{eff}) parameterisations.

Label	Parameterisation	Details
MF_1	$\rho_{\mathrm{eff}} = 0.15 d_{\mathrm{mean}}^{-1}$	From Mitchell *et al.* [1990] mass-size relationship and Fabry and Szyrmer [1999] assumption that the d_{mean} is related to d_{max} by $d_{\mathrm{mean}}^3 = 0.15 d_{\mathrm{max}}^3$.
MF_2	$\rho_{\mathrm{eff}} = 0.12 d_{\mathrm{mean}}^{-1}$	Same mass-size relationship as above and Fabry and Szyrmer [1999] assumption that $d_{\mathrm{mean}}^3 = 0.22 d_{\mathrm{max}}^3$.
LF	$\rho_{\mathrm{eff}} = 0.065 d_{\mathrm{mean}}^{-1.18}$	From Locatelli and Hobbs [1974] mass-size relationship and Fabry and Szyrmer [1999] assumption that $d_{\mathrm{mean}}^3 = 0.22 d_{\mathrm{max}}^3$.
BA	$\rho_{\mathrm{eff}} = 0.076 d_{\mathrm{mean}}^{-1}$	From Baran *et al.* [2011a] mass-size relationship.

3.2 Effective density

3.2.1 From volume or mass fraction

When a homogeneous mixture is composed of a number (n) of distinct materials, with mass and volume of m_{i} and v_{i}, the density of those materials, taken together, is called the effective density (ρ_{eff}) of the mixture. It is defined as

$$\rho_{\mathrm{eff}} = \frac{\sum_{i=1}^{n} m_{\mathrm{i}}}{\sum_{i=1}^{n} v_{\mathrm{i}}}. \tag{3.4}$$

If f_{i}^{v} is the volume fraction of each component material, ρ_{eff} is

$$\rho_{\mathrm{eff}} = f_1^v \rho_1 + f_2^v \rho_2 + \ldots + f_{\mathrm{n}}^v \rho_{\mathrm{n}}, \tag{3.5}$$

and if f_{i}^{m} represents the mass fraction of each component material, ρ_{eff} is

$$\rho_{\mathrm{eff}} = \frac{\rho_1 \rho_2 \ldots \rho_{\mathrm{n}}}{f_1^m \rho_2 \ldots \rho_{\mathrm{n}} + f_2^m \rho_1 \rho_3 \ldots \rho_{\mathrm{n}} + \ldots + f_{\mathrm{n}}^m \rho_1 \ldots \rho_{\mathrm{n}-1}} \tag{3.6}$$

where $f_1^v + f_2^v + \ldots + f_{\mathrm{n}}^v = 1$, $f_1^m + f_2^m + \ldots + f_{\mathrm{n}}^m = 1$, and ρ_{i} is the density of each component of the mixture.

According to equation 3.5 and 3.6, ρ_{eff} of a soft particle (consisting of ice and air) can be computed as either

$$\rho_{\mathrm{eff}} = (1 - f_{\mathrm{a}}^v)\rho_{\mathrm{ice}} + f_{\mathrm{a}}^v \rho_{\mathrm{air}} \tag{3.7}$$

or

$$\rho_{\mathrm{eff}} = \frac{\rho_{\mathrm{ice}} \rho_{\mathrm{air}}}{f_{\mathrm{a}}^m \rho_{\mathrm{ice}} + (1 - f_{\mathrm{a}}^m)\rho_{\mathrm{air}}} \tag{3.8}$$

where f_{a}^v and f_{a}^m are the volume and mass fractions of air; ρ_{ice} and ρ_{air} are, respectively, the density of ice and air.

3.2.2 From size-density relationship

Another approach to estimate ρ_{eff} is considering a power-law size-density relationship. Four examples on such relationships found in the literature, are summarised in Table 3.1. The parameterisations presented in this table, are derived from the Mitchell *et al.* [1990], Locatelli and Hobbs

[1974], or Baran *et al.* [2011a] mass-size relationships. Differences in the mass-size relationships lead to a noticeable variety of the ρ_{eff} values. For example, for a particle with a given d_{mean}, MF_1 and LF models estimate the highest and the lowest ρ_{eff}, respectively. Furthermore, Figure 4.1 in Chapter 4 compares the four examples of ρ_{eff}, that are presented in Table 3.1, with ρ_{eff}, that is applied in Hogan *et al.* [2012].

3.3 Air fraction

The volume air fraction (f_{a}^{v}) of a soft particle can be calculated through equation 3.7 as

$$f_{\text{a}}^{v} = \frac{\rho_{\text{ice}} - \rho_{\text{eff}}}{\rho_{\text{ice}} - \rho_{\text{air}}}, \tag{3.9}$$

where ρ_{ice} and ρ_{air} values are independent of particle size. There are two approaches to determine the value of ρ_{eff}. First, it can be set to follow a size-density relationship, which leads to a variation of ρ_{eff} with particle size (see table 3.1). Second, ρ_{eff} can be assumed as a constant value at all particle sizes. These two approaches give the two following variations of f_{a}^{v}:

Variable air fraction
When ρ_{eff} of soft particles is estimated from a size-density relationship, the f_{a}^{v} computed through equation 3.9, varies as a function of particle size.
Fixed air fraction
f_{a}^{v} is fixed if ρ_{eff} is set to be constant at all particle sizes.

Assuming any of these approaches of air fraction has a significant impact on the soft particle model results. These impacts are discussed in chapter 6.

3.4 Refractive index

The refractive index (n) of a medium is a dimensionless number that describes how radiation propagates through the medium. The (complex) refractive index is related to (complex) dielectric constant (ε) through

$$n = \sqrt{\varepsilon}, \tag{3.10}$$

where it is assumed that the magnetic permeability of the medium equals unity.

The real part of refractive index (n') determines the propagation speed, and the imaginary part (n'') is responsible for the absorption. Therefore, both the real and imaginary parts of the refractive index must be known to model the scattering properties of a particle.

The refractive index (n) of pure ice has been parameterized according to laboratory measurements and been empirically modelled by several studies (e.g. Warren [1984]; Liebe *et al.* [1993]; Zhang *et al.* [2001]; Jiang and Wu [2004]; Mätzler *et al.* [2006]; Warren and Brandt [2008]). Figure 3.2 shows a comparison of these parameterisations. In contrast to n', n'' varies highly with

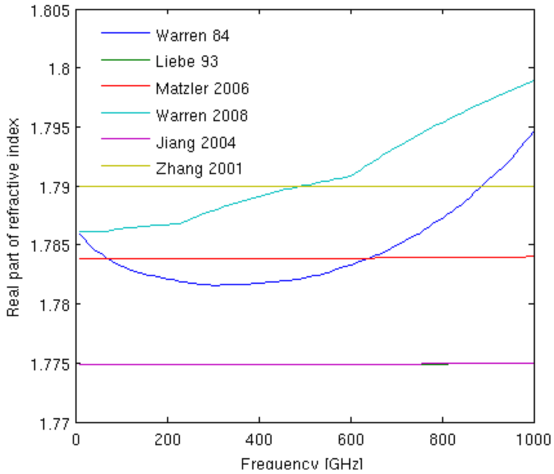

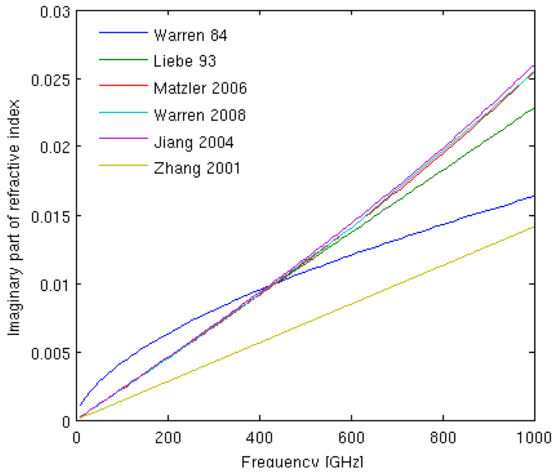

Figure 3.2: Real (left) and imaginary (right) parts of the refractive index of pure ice as a function of frequency. Both real and imaginary parts are derived through parameterisations from Warren [1984], Liebe *et al.* [1993], Zhang *et al.* [2001], Jiang and Wu [2004], Mätzler *et al.* [2006], and Warren and Brandt [2008]. The temperature is set to 266 K.

frequency. n'' estimated from Warren [1984] and Zhang *et al.* [2001] shows deviation compared to other three parameterisations. On the other hand, Jiang and Wu [2004], Mätzler *et al.* [2006], and Warren and Brandt [2008] estimate quite similar n''. A more detailed discussion about differences of these refractive index parameterisations is found in the section 2.1 of Eriksson *et al.* [2014].

3.4.1 Mixing rules

The refractive index (n) of a mixture can be obtained either through a numerical model or a simplified method, a so called mixing rule. This section provides a brief explanation of commonly used mixing rules and compare their result regarding estimation of dielectric constant (ε), and then consequently also n.

Mixing rules are algebraic formulas which calculate the "effective" dielectric constant (ε_{eff}) of an uniformly distributed mixture as a function of its constituent dielectric constants, where the microstructure of the mixture is characterised by fractional volumes of components and possibly some other parameters [Sihvola, 2000]. The three most commonly used mixing formulas are Maxwell Garnett [Garnett, 1906], Bruggeman [Bruggeman, 1935], and Debye [Debye, 1929].

Debye:

$$\frac{\varepsilon_{\text{eff}}-1}{\varepsilon_{\text{eff}}+2}=\frac{f^{v}_{inc}(\varepsilon_{\text{inc}}-1)}{\varepsilon_{\text{inc}}+2}+\frac{(1-f^{v}_{inc})(\varepsilon_{\text{mat}}-1)}{\varepsilon_{\text{mat}}+2}, \tag{3.11}$$

Bruggeman:

$$\frac{f^{v}_{inc}(\varepsilon_{\text{inc}}-\varepsilon_{\text{eff}})}{\varepsilon_{\text{inc}}+2\varepsilon_{\text{eff}}}+\frac{(1-f^{v}_{inc})(\varepsilon_{\text{mat}}-\varepsilon_{\text{eff}})}{\varepsilon_{\text{mat}}+2\varepsilon_{\text{eff}}}=0, \tag{3.12}$$

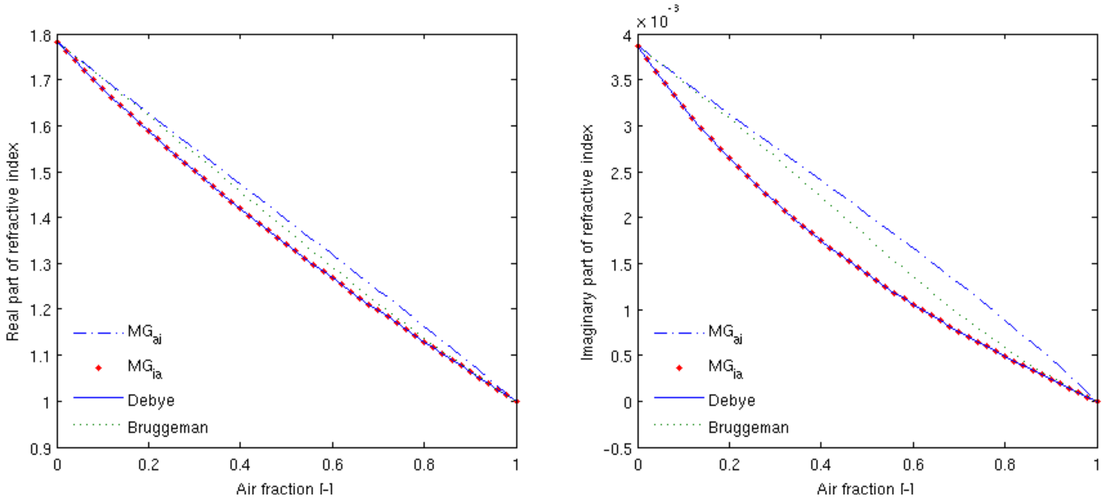

Figure 3.3: Real (left) and imaginary (right) parts of the effective refractive index in a mixture of ice-air as a function of air fraction through applying different mixing rules. The refractive index of ice is set to $1.7831 + 0.0039i$, (valid for 183 GHz and 263 K), and refractive index of air is set to 1.

Maxwell Garnett (MG):

$$\varepsilon_{\mathrm{eff}} = \varepsilon_{\mathrm{mat}} + 3 f^{v}_{inc} \varepsilon_{\mathrm{mat}} \frac{(\varepsilon_{\mathrm{inc}} - \varepsilon_{\mathrm{mat}})}{\varepsilon_{\mathrm{inc}} + 2\varepsilon_{\mathrm{mat}} - f^{v}_{inc}(\varepsilon_{\mathrm{inc}} - \varepsilon_{\mathrm{mat}})}, \tag{3.13}$$

where f^{v}_{inc} is the volume fraction of the inclusion in a mixture, and $\varepsilon_{\mathrm{mat}}$ and $\varepsilon_{\mathrm{inc}}$ are the dielectric constants of the matrix and inclusion media in a mixture, respectively.

Unlike Debye and Bruggeman, the MG formula is asymmetric regarding to order of matrix and inclusion medias [Meneghini and Liao, 1996]. For example, an ice matrix with air inclusion returns a different dielectric constant compared to an air matrix with ice inclusion:

$$MG_{\mathrm{ai}} \neq MG_{\mathrm{ia}}. \tag{3.14}$$

It is not physically clear how to select among the various mixing formulas. Several studies have reviewed the available mixing rule models and investigated their impact on calculation of scattering properties of a homogeneous mixed-phase particles, compared to properties measured or derived through other numerical methods. Bohren and Battan [1980] derived the refractive indices of ice-water mixtures by three mentioned mixing rules and examined their result on backscattering cross sections and showed that applying MG (with ice included in a water matrix) compares best with backscattering measurements at the wavelength of 5.05 cm, especially when the volume fraction of water is higher than 0.5. Meneghini and Liao [1996] insisted that the characterisation of the mixed-phased hydrometeors dielectric properties is a critical part in the modelling of the partially melting layer properties. Liao *et al.* [2013] concluded that the result of applying the Bruggeman mixing rule to estimate scattering properties for oblate/prolate spheroidal mixed-phase mixtures exhibits fairly good agreement with those of properties derived by the conjugate-gradient and fast Fourier transform (CGFFT) numerical method up to size parameters of 4. Johnson *et al.* [2012]

conducted a sensitivity analysis for frequencies between 2.8 and 150 GHz regarding the choice of mixing rule. The differences when using MG_{ai} or MG_{ia} were found to be $\sim$2 dB for radar reflectivity and at least 10 K for brightness temperature. We examine the impact of applying the different mixing rules for soft particles in section 6.2.2, to see if any of the mixing rules gives the soft particle model the best chance to approximate realistically shaped particles.

An example comparison between the mixing rules is shown in Figure 3.3. This figure presents the variation of the real and imaginary parts of refractive index as a function of air fraction. The refractive indices calculated by the MG_{ia} mixing rule are equal to those derived from the Debye one, so hereafter only MG_{ai}, MG_{ia} , and Bruggeman are considered. The refractive index values derived by the Bruggeman mixing rule fall between those of MG_{ai} and MG_{ia} at all air fractions. In other words applying MG_{ai} and MG_{ia} result in the highest and lowest refractive indices, respectively. In Figure 3.3, the refractive index of pure ice is calculated at only one frequency and one temperature. The results at other frequencies and temperatures are very similar to those presented in this figure. This is actually expected, because the real part of the refractive index of ice does not depend on frequency. Although the imaginary part has frequency dependency, the pattern between mixing rules are the same when other frequencies and temperatures were tested.

4 Review of some soft particle models

This chapter reviews the physical properties of two examples of soft particle models that have been applied to represent the ice particle properties. Liu [2004] used a soft spherical model and Hogan *et al.* [2012] applied a soft spheroidal model.

4.1 Hogan *et al.* [2012]

Using coincident radar and aircraft observations, Hogan *et al.* [2012] concluded that a soft horizontally-aligned-oblate-spheroid shape model works well in most ice clouds and suggested that there is no need to use more sophisticated ice particle shapes to estimate the IWC for radar measurements. Following sections derive the physical properties of the soft horizontally-aligned-oblate-spheroidal particle that is used in Hogan *et al.* [2012] (hereafter denoted as HSP).

4.1.1 Dimensions

The Brown and Francis [1995] mass-size relationship (equation 3.1) was applied by Hogan *et al.* [2012] to estimate the d_{mean} of the HSP.

Using aircraft measurements, Hogan *et al.* [2012] also estimated $d_{\text{short}}/d_{\text{max}}$ to be 0.6 for irregular particles larger than 97 μm. This value according to equation 2.3 gives

$$\alpha = \tfrac{d_{\text{max}}}{d_{\text{short}}} = 1.66; \quad d_{\text{max}} \geq 97 \cdot 10^{-6}\, m. \tag{4.1}$$

Figure 4.2 shows that the HSP smaller than 66 μm are assumed to be spherical solid ice with axial ratio of 1. For particles with d_{max} between 66 μm and 97 μm, α increases linearly up to d_{max} equal to 97 μm, whereafter the axial ratio is set to 1.66.

The relation between d_{mean}, d_{short}, and d_{max} through equation 2.2 and equation 4.1, is

$$d_{\text{mean}} = \frac{1.66 d_{\text{short}} + d_{\text{short}}}{2} = 1.33 d_{\text{short}} = 0.8 d_{\text{max}}, \tag{4.2}$$

and furthermore, through equations 3.1, 2.2, and 4.1, d_{e}, d_{max}, and d_{short} are related as

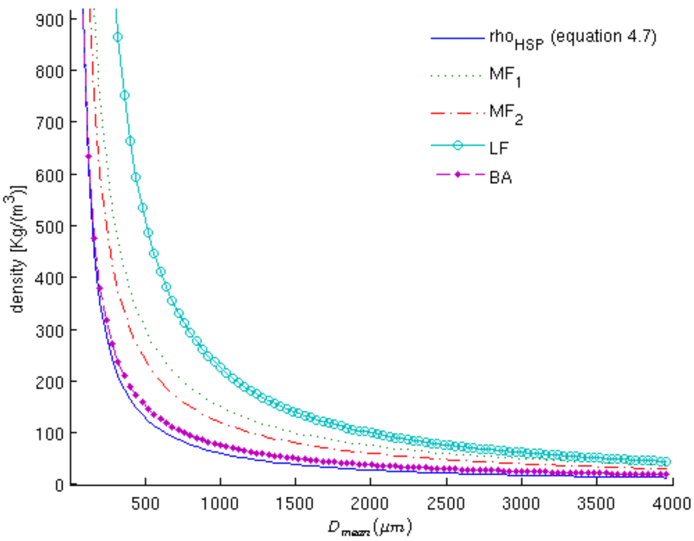

Figure 4.1: The effective density of particles as a function of d_{mean}, derived from the power-law size-density relationships of Table 3.1 and equation 4.7.

$$
\begin{aligned}
m_{\text{ice}} &= m_{\text{HSP}} \\
\rho_{\text{ice}} \cdot \frac{\pi d_e^3}{6} &= 0.0185 d_{\text{mean}}^{1.9}; \quad d_{\text{mean}} \geq 97 \cdot 10^{-6}\, m \\
d_{\text{mean}} &= \left(\rho_{\text{ice}} \cdot \frac{\pi d_e^3}{6 \cdot (0.0185)}\right)^{\frac{1}{1.9}} \\
&= 210.47 \cdot d_e{}^{1.58}; \\
d_{\text{max}} &= 263.09 \cdot d_e{}^{1.58}; \\
d_{\text{short}} &= 157.85 \cdot d_e{}^{1.58};
\end{aligned}
\tag{4.3}
$$

where m_{HSP} and m_{ice} represent mass of the HSP and corresponding solid ice sphere, respectively.

4.1.2 Effective density

The dimensions of the HSP (d_{max}, d_{short}) were calculated in section 4.1.1, and its volume is

$$V_{\text{HSP}} = \frac{\pi}{6} d_{\text{max}}^2 d_{\text{short}}. \tag{4.4}$$

It should be noted that the V_{eff} of an ice particle such as the HSP, is easily estimated when it is assumed to be spherical or spheroidal, while for arbitrary shaped particle different definitions are used. The most common definition is to assume the volume of the smallest surrounding sphere, as V_{eff}.

As mentioned earlier, $m_{\text{HSP}} = m_{\text{ice}}$ (the mass of air is negligible), therefore the ρ_{eff} is

$$\rho_{\text{eff}} = \frac{m}{V_{\text{HSP}}} = \frac{480 d_e^3}{\frac{\pi}{6} D_{\text{max}}^2 d_{\text{short}}}, \tag{4.5}$$

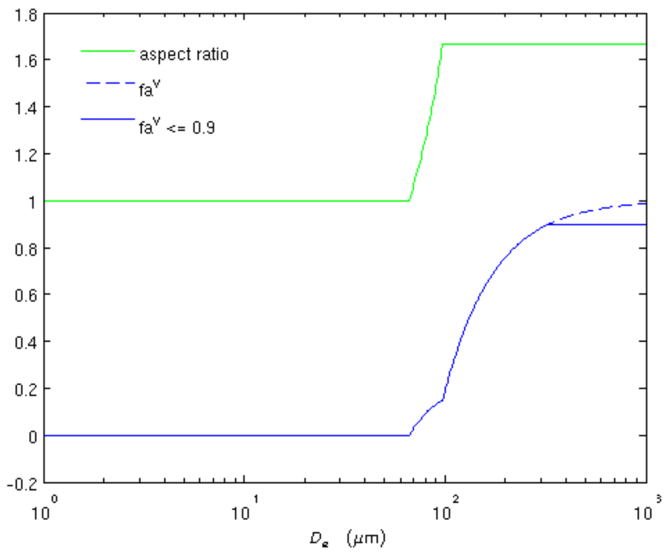

Figure 4.2: The axial ratio (α) and the fraction of air in the soft-spheroidal particles (applied by Hogan *et al.* [2012]), as a function of mass equivalent diameter d_e. Dashed blue line presents no limitation for volume air fraction and solid green line shows an example of an upper limit (0.9) for volume of air fraction.

then by applying equation 4.3, the ρ_{eff} is derived as a function of d_e

$$\rho_{eff} = \frac{8.39 \cdot 10^{-5}}{d_e^{1.74}}. \tag{4.6}$$

As the ρ_{eff} of a particle that consisting of only ice and air, can not be less than 1 Kg/m^3 (density of air), the equation 4.5 and 4.6 is valid when $d_e \leq 4 \cdot 10^{-3}\, m$. This is due to neglecting the air mass in equation 4.5.

By applying equations 4.1, 4.2, and Brown and Francis [1995] mass-size relationship from equation 3.1, we derived a power-law size-density relationship for the HSP as

$$\begin{aligned} &\rho_{eff} = \frac{0.0185 d_{mean}^{1.9}}{\frac{\pi}{6} \cdot (d_{max})^2 d_{short}} = \frac{0.0185 d_{mean}^{1.9}}{\frac{\pi}{6} \cdot (1.66 d_{short})^2 d_{short}} = \frac{0.0185 d_{mean}^{1.9}}{1.44 \cdot \left(\frac{d_{mean}}{1.33}\right)^3} = 0.03 d_{mean}^{-1.1}; \\ &d_{mean} \geq 97 \cdot 10^{-6}\, m \end{aligned} \tag{4.7}$$

Figure 4.1 compares this power-law size-density relationship with those of Table 3.1. The result shows that the soft-spheroidal particles (HSP) applied in Hogan *et al.* [2012] have lower density compared with other parameterisations.

4.1.3 Air fraction

The air fraction (f_a^v) of the HSP can be derived through equation 3.9. Figure 4.2 shows f_a^v as a function of d_e. The particles smaller than 66 μm are assumed as spherical solid ice with air fraction of 0. For particles with d_{max} larger than 66 μm, f_a^v increases gradually up to 1 (dashed blue line), but for the reason discussed in section 6.2.3, we set an upper limit for the air fraction. The f_a^v with a limitation of 0.9 is presented by the solid blue line.

4.2 Liu [2004]

Liu [2004] used soft spheres to approximate the single scattering properties of three randomly-oriented types of non-spherical ice particles: bullet rosettes, sector-like snowflakes, and dendrite snowflakes, for frequencies between 85 and 220 GHz.

The approximation steps were: First, Liu applied the Discrete Dipole Approximation method (DDA, which is reviewed in section 5.1) to calculate the single scattering properties of the three randomly-oriented non-spherical particle types mentioned. Then he showed that the single scattering properties of non-spherical particles estimated by the DDA method, have a magnitude between those of the mass equivalent solid ice sphere with diameter of d_e, and the soft sphere with a diameter of the particle's maximum dimension (d_max). The single scattering properties of the spheres were calculated by the Lorenz-Mie method (see section 5.1). Finally, to reach the best fit of DDA results by soft spheres, Liu [2004] defined a softness parameter as

$$SP = \frac{d - d_\mathrm{e}}{d_\mathrm{max} - d_\mathrm{e}}, \tag{4.8}$$

where the SP varies between 0 (i.e., $d = d_\mathrm{e}$) and 1 (i.e., $d = d_\mathrm{max}$).

According to the procedure above, Liu [2004] concluded that the best-fit soft sphere has a SP value between 0.2 and 0.5, depending on frequency and particle shape. It indicates that the best soft sphere to substitute the scattering properties of non-spherical ice particles, has a diameter larger than the solid ice sphere, and smaller than maximum dimension of the particle.

5 Calculation of single scattering properties

Modelling of the single scattering properties (such as absorption and scattering efficiencies, and phase function) of ice particles has always been a difficult task, due to the huge variety of unknown variables, such as particle shape, density, and orientation. On the other hand, if all mentioned physical and geometrical properties are properly defined, the complexity of solving the Maxwell equations is another restriction to model the single scattering properties.

This chapter briefly reviews three general models of solving Maxwell equations: Lorenz-Mie theory, T-matrix, and Discrete Dipole Approximation (DDA) and describes their advantages and limitations to calculate the single scattering properties of ice particles. Then, the radiative transfer equation is presented to give an overview of required inputs to solve it. The closing section examines the stability of T-matrix results in comparison with Mie function for spherical particles.

5.1 Calculation methods

There are several published models for calculating a particle's single scattering properties. All models compute the electromagnetic scattering, based on solving the differential Maxwell equations in either analytical or numerical approaches. For details, the reader is referred to Mishchenko *et al.* [2002] and Liou [2002].

Generally, the calculations models take the particle refractive index and physical properties as input, and calculate the particle single scattering properties: absorption, scattering, and extinction cross sections (C_{abs}, C_{sca}, and C_{ext}), as well as phase function. Three of those models are briefly reviewed in following.

1) **Lorenz-Mie theory**

For spherical particles, Lorenz-Mie theory provides an exact solution for Maxwell equations [Liou, 2002]. The Lorenz-Mie code developed by Mätzler [2002] is applied in this project.

2) **T-matrix**

For non-spherical particles that are rotationally symmetric, such as spheroidal (oblate or prolate) and cylindrical particles, T-matrix provides a numerical solution for Maxwell equations to compute the single scattering. The T-matrix code by Mishchenko *et al.* [2002] is applied in this project.

3) **Discrete Dipole Approximation (DDA)**

The Discrete Dipole Approximation (DDA) is a flexible method which calculates the single scattering properties of arbitrarily shaped and inhomogeneous ice particles [Draine and Flatau, 2012]. In the DDA method, a particle is represented as an array of dipoles in a cubic lattice with a given interdipole spacing. Consequently, the DDA method is suitable for ice crystals with highly varying shapes. The interdipole spacing must be adequately small relative to the incident wavelength in order to obtain desired accuracy, which requires large computer memory and long calculation time for large particles.

5.2 Radiative transfer equation

Particle single scattering properties must be derived to obtain the requested input for the radiative transfer equation. Figure 1.1 briefly illustrates the relation between particle physical properties, single scattering, bulk scattering and final outputs.

The radiative transfer equation describes the transfer of radiation through a medium (in our case, atmosphere which includes clouds) between the radiation source (the Earth's surface or atmosphere) and a sensor.

The vector radiative transfer equation (where vector implies that the complete polarisation state is considered) in a cloudy media can be written as [Eriksson *et al.*, 2011b]

$$\frac{d\mathbf{I}(\nu,r,n)}{ds} = -\mathbf{K}(\nu,r,n)\mathbf{I}(\nu,rn) + \mathbf{a}(\nu,r,n)B(\nu,r) + \int_{4\pi} \mathbf{P}(\nu,r,n,n')\mathbf{I}(\nu,r,n')dn', \tag{5.1}$$

where $\mathbf{I}$ is the Stokes vector, ds a path length along n, ν the frequency, r and n are positions in the atmospheric and propagation direction, respectively; $\mathbf{K}$ the extinction matrix, $\mathbf{a}$ the absorption vector, $\mathbf{P}$ the phase matrix or scattering matrix, and B is the Planck function.

5.3 Extinction

5.3.1 Theory

The structure of the extinction matrix (K) in the radiative transfer equation (equation 5.1) for a horizontally aligned particle, with its rotational axis (axis of symmetry) coinciding with the vertical z-axis [Mätzler *et al.*, 2006], is

$$K(\theta) = \begin{bmatrix} k_{11}(\theta) & k_{12}(\theta) & 0 & 0 \\ k_{12}(\theta) & k_{11}(\theta) & 0 & 0 \\ 0 & 0 & k_{11}(\theta) & k_{34}(\theta) \\ 0 & 0 & -k_{34}(\theta) & k_{11}(\theta) \end{bmatrix}, \tag{5.2}$$

where θ is the zenith angle. Unlike the case for spherical particles, the extinction matrix of an axially oriented particle is not diagonal, therefore both the intensity and the polarisation state of the incident beam are changed by this kind of particle. According to 5.2, the extinction matrix (K) is defined by only three different elements that are $k_{11}(\theta)$, $k_{12}(\theta)$, and $k_{34}(\theta)$. This full extinction matrix is needed when the vector radiative transfer equation (5.1) is applied, i.e., when all polarisation states are considered in parallel. In the case of applying the scalar radiative transfer equation, only one scalar extinction value (C_{ext}) is needed in the equation. Depending on which polarisation state is observed, following equations explain which value of the extinction matrix (K) should be used in the scalar radiative transfer equation.

The attenuation of the unpolarized radiation ($[1 \quad 0 \quad 0 \quad 0]^T$) over the small path length of Δl, is

$$\Delta l \cdot \begin{bmatrix} k_{11}(\theta) & k_{12}(\theta) & 0 & 0 \\ k_{12}(\theta) & k_{11}(\theta) & 0 & 0 \\ 0 & 0 & k_{11}(\theta) & k_{34}(\theta) \\ 0 & 0 & -k_{34}(\theta) & k_{11}(\theta) \end{bmatrix} \cdot \begin{bmatrix} 1 \\ 0 \\ 0 \\ 0 \end{bmatrix} = \Delta l \cdot \begin{bmatrix} k_{11}(\theta) \\ k_{12}(\theta) \\ 0 \\ 0 \end{bmatrix}. \tag{5.3}$$

This shows that the extinction cross section (C^I_{ext}) in the scalar radiation transfer is presented by k_{11}.

The attenuation of the vertically polarised radiation ($[1 \quad 1 \quad 0 \quad 0]^T$) over the small path length of Δl, is

$$\Delta l \cdot \begin{bmatrix} k_{11}(\theta) & k_{12}(\theta) & 0 & 0 \\ k_{12}(\theta) & k_{11}(\theta) & 0 & 0 \\ 0 & 0 & k_{11}(\theta) & k_{34}(\theta) \\ 0 & 0 & -k_{34}(\theta) & k_{11}(\theta) \end{bmatrix} \cdot \begin{bmatrix} 1 \\ 1 \\ 0 \\ 0 \end{bmatrix} = \Delta l \cdot \begin{bmatrix} k_{11}(\theta)+k_{12}(\theta) \\ k_{12}(\theta)+k_{11}(\theta) \\ 0 \\ 0 \end{bmatrix}. \tag{5.4}$$

In this case, $k_{11}+k_{12}$ represents the extinction cross section (C^v_{ext}) in the scalar radiation transfer.

The attenuation of the horizontally polarised radiation ($[1 \quad -1 \quad 0 \quad 0]^T$) over the small path length of Δl, is

$$\Delta l \cdot \begin{bmatrix} k_{11}(\theta) & k_{12}(\theta) & 0 & 0 \\ k_{12}(\theta) & k_{11}(\theta) & 0 & 0 \\ 0 & 0 & k_{11}(\theta) & k_{34}(\theta) \\ 0 & 0 & -k_{34}(\theta) & k_{11}(\theta) \end{bmatrix} \cdot \begin{bmatrix} 1 \\ -1 \\ 0 \\ 0 \end{bmatrix} = \Delta l \cdot \begin{bmatrix} k_{11}(\theta)-k_{12}(\theta) \\ k_{12}(\theta)-k_{11}(\theta) \\ 0 \\ 0 \end{bmatrix}. \tag{5.5}$$

This equation implies that C^h_{ext} is determined by $k_{11}-k_{12}$ in the scalar radiation transfer.

Using the similar transformation for ± 45 linear polarisation ($[1 \quad 0 \quad \pm 1 \quad 0]^T$), and left/right-hand circular polarisation ($[1 \quad 0 \quad 0 \quad \pm 1]^T$), shows that C_{ext} in these cases are k_{11} [Eriksson *et al.*, 2011b].

5.3.2 Absorption vs. Scattering

Extinction includes both scattering out of the line-sight and absorption. To study scattering, the absorption effect should be removed from the extinction cross section. Figure 5.1 and Figure 5.2

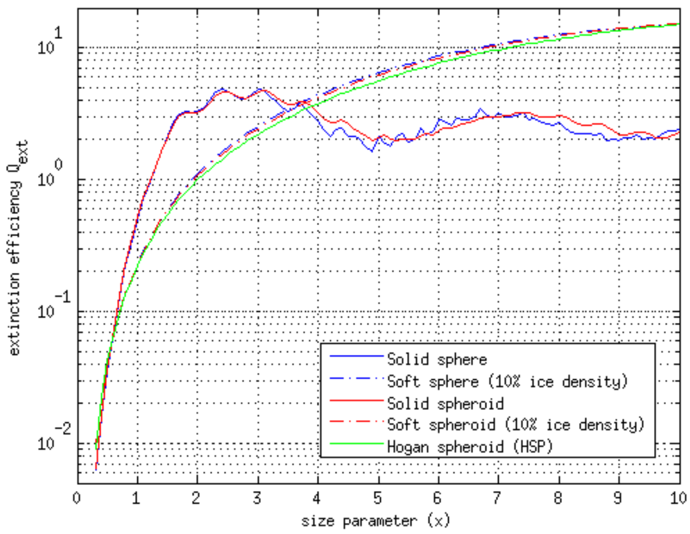

Figure 5.1: Extinction efficiency (Q^I_{ext}) of solid ice spheres, soft spheres, solid ice spheroids, soft spheroids (with $\rho_{\mathrm{eff}} = 10\%$ of ice density), and HSP (with ρ_{eff} derived in section 4.1.2). The results are valid for 183.31 GHz. The air fraction (f^v_a) is set to 0.9 for HSP, and the $\mathrm{MG_{ai}}$ is applied to compute the refractive index.

show the extinction and scattering efficiencies for an identical set of particles. As seen in Figure 5.2, the scattering efficiencies are marginally lower than the extinction efficiencies in Figure 5.1 and generally these two figures are quite similar. This resemblance implies that the absorption efficiencies are low and can be neglected. This is in fact expected, as the imaginary part of the refractive index, that is responsible for absorption, is low for ice particles throughout the microwave region (see section 3.4). The overall consequence is that scattering dominates the extinction, or reversely, the absorption has no significant effect on the extinction and can largely be ignored for ice particles. However, the importance of absorption increases with optical thickness. When radiation passes through a cloud that is optically thick, the amount of absorption by particles increases due to multiple scattering. Eriksson *et al.* [2014] conducted a test to investigate the importance of absorption for passive microwave measurements, and concluded that the absorption becomes more pronounced in the case of an optically thick cloud.

5.3.3 Examples

Figure 5.3 shows the extinction cross section (C^I_{ext}) as a function of zenith angle (θ) at two frequencies. All three particles (solid spherical, solid spheroidal, and the Hogan soft spheroidal particle (HSP)) have the same ice mass.

As shown in this figure, C^I_{ext} of solid sphere is independent of θ, while the solid spheroid and the soft spheroid (HSP) cross sections show variation as a function of θ. In Figure 5.3a, the HSP cross section is higher than both the solid ice spherical and spheroidal cases, however in

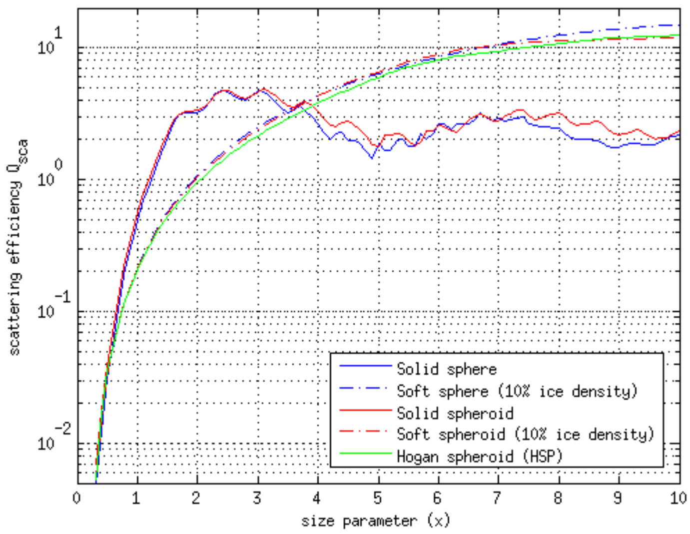

Figure 5.2: Scattering efficiency (Q^I_{sca}) of the same particles as Figure 5.1.

Figure 5.3b, the HSP cross section is lower than two other cases. The reason for this, as discussed in following, can be understood by considering how the extinction or scattering cross section is estimated relative to the refractive index (n) and the size parameter (x). Note that scattering dominates the extinction (see section 5.3.2).

In the Rayleigh regime ($x \ll 1$), the scattering cross section is related to $x^6\,|1-n|$. For a given frequency, if the particle becomes softer, its refractive index n decreases and gets closer to 1, while its dimensions and consequently its size parameter x increases. So, there are two competing values, x^6 and $|1-n|$. According to the power of x, the size parameter effect is more important in the Rayleigh regime and it is expected that the scattering or the extinction cross section of the soft spheroid is higher than the solid cases. Figures 5.3a, and 5.4a confirm this fact and show that for particles with $d_{\text{e}} = 200\,\mu$m at 90 GHz (corresponding to $x \approx 0.18$) , the cross section of HSP is higher than those of solid particles.

In the geometrical-optics regime where the particles are larger than the wavelength ($x \gg 1$), the scattering cross section is proportional to $x^2|1-n|$. So the dependency of the scattering cross section on the size parameter decreases, and it is expected that the value $|1-n|$ is more pronounced. Consequently, the scattering or the extinction cross section of the soft particles is less than the scattering or the extinction cross section of the solid ones. Figures 5.3b, 5.4b, and 5.4c confirm what is discussed above and show that for particles with $d_{\text{e}} = 200\,\mu$m at 500 GHz (corresponding to $x \approx 1.05$), the cross section of HSP is lower than those of solid particles.

C^I_{ext} is shown in Figure 5.4 for three different frequencies, as a function of d_{e}. For a given frequency, the value of the extinction cross sections is governed by the size of the particle and its refractive index. The refractive index is a function of frequency and temperature. As shown in Figure 3.2, the real part of the refractive index is basically constant relative to the frequency and

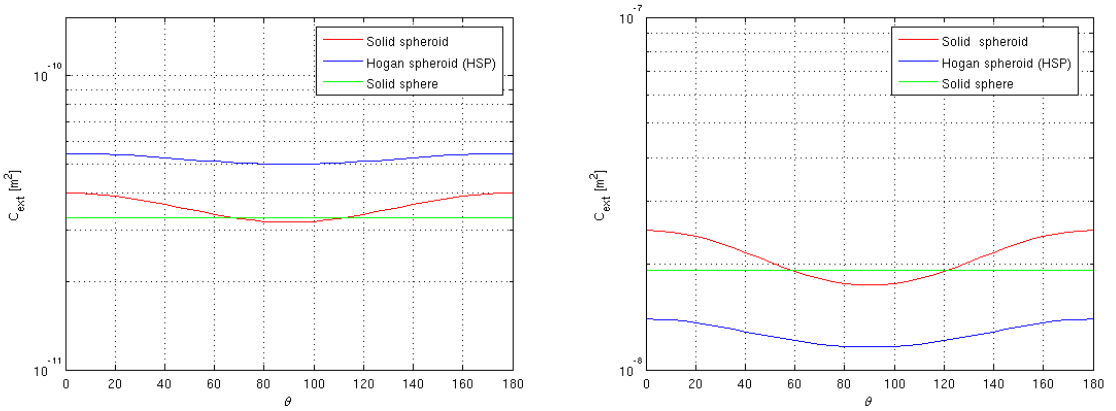

(a) $f = 90$ GHz, $d_e = 200\,\mu$m (b) $f = 500$ GHz, $d_e = 200\,\mu$m

Figure 5.3: Extinction cross section (C^I_{ext}) of a solid ice spherical particle, a solid ice spheroidal particle, and HSP as a function of zenith angle (θ). All three types of particles have the same mass ($d_e = 200\,\mu$m). The frequency is (a) 90 and (b) = 500 GHz. For HSP particles, the air fraction (f^v_a) is set to 0.9 and α is 1.66. MG_{ai} is applied to compute the refractive index.

only the imaginary part, which causes the absorption, is sensitive to the frequency. According to section 5.3.2, the absorption is generally low for ice particles.

The effect of particle size is determined with respect to the wavelength of the radiation and can be described by x. For instance, the value of x for a particle with $d_e = 500\,\mu$m at frequency of 90 GHz, is 0.47. More or less the same x is obtained for $d_e = 230\,\mu$m at 200 GHz, and $d_e = 110\,\mu$m at 500 GHz. This resemblance of x and general insensitivity of the refractive indices to the frequency lead to a repeated pattern in three panels of Figure 5.4. The cross sections of solid ice spherical, solid ice spheroidal and HSP particles at the frequency of 90 GHz, are repeated as patterns in 200 GHz for particles with d_e smaller than about 230 μm, and in 500 GHz for particles with d_e smaller than about 110 μm.

5.4 Examination of stability of T-matrix results

All the single scattering properties for spherical particle above, have been calculated by the Mie function of Mätzler [2002], and all the properties for spheroidal particles, have been derived by the T-matrix method Mishchenko *et al.* [2002]. This section provides a short examination of T-matrix test results. To examine the stability of T-matrix results, the simplest approach is to consider spherical particles and compare the results of the T-matrix function with results of the Mie function. To do this comparison, six different refractive indices were picked to consider the outcome for low to high absorption. The results are found in Figure 5.5 and show significant deviation in scattering and absorption efficiencies when the size parameter (x) is larger than about 5. There should be no absorption when the refractive index has no imaginary part, however, according to Figure 5.5d ($n = 2 + 0i$) and Figure 5.5j ($n = 5 + 0i$), Tmatrix gives some absorption efficiencies

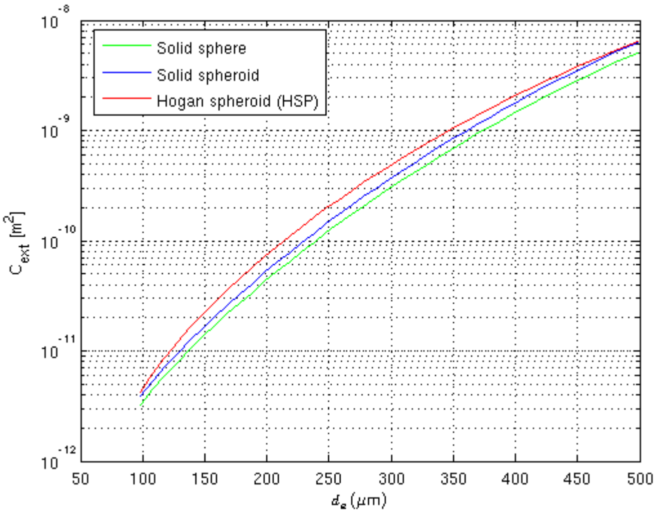

(a) 90 GHz

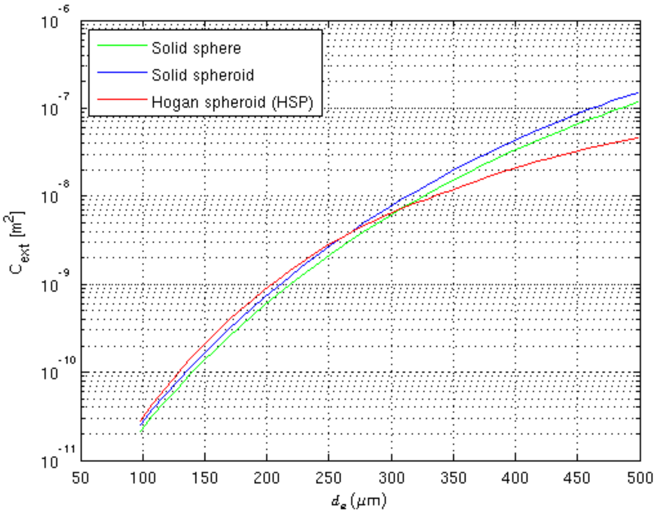

(b) 200 GHz

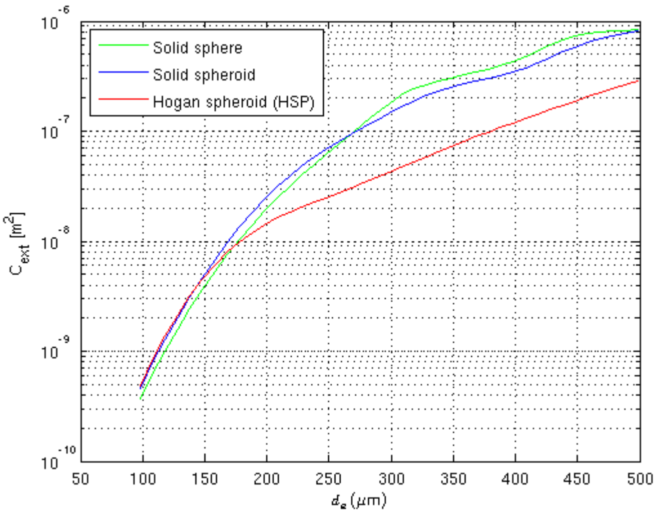

(c) 500 GHz

Figure 5.4: Extinction cross section (C^I_{ext}) as a function of mass equivalent diameter (d_{e}). The zenith angle (θ) is 0. For Hogan spheroid (HSP), the air fraction (f^v_{a}) is set to 0.9 and α is 1.66. $\mathrm{MG_{ai}}$ is applied to compute the refractive index of soft particles (HSP).

for larger particles. Given these results, it seems there is a limitation to use the Tmatrix method for large size parameters. As shown in Figure 5.5, the extinction efficiencies of the mentioned six different refractive indices present the same results for both the Mie and T-matrix functions. It indicates that the absorption and scattering efficiencies compensate their deviation in terms of the extinction efficiencies. However, as discussed in Eriksson *et al.* [2011b], when thermal emission is considered by the radiative transfer equation, both absorption and scattering efficiencies should have the correct values since they have different impacts. Nevertheless, if the Beer–Lambert law is valid, i.e., the total attenuation is of special importance, then it wouldn't matter if we only have the correct extinction values.

Different axial ratios were tested (1.0001, 1.001, 1.01, 0.999) with no clear impact. Note that the axial ratio of exactly 1, is not recommended for T-matrix.

The absorption and scattering efficiencies of ice and water spherical particles at 90 GHz and 500 GHz from the Mie and T-matrix functions, are depicted in Figure 5.6, again confirming the deviation between Mie and T-matrix results. That is, the figure shows that T-matrix estimates too low scattering and too high absorption for size parameters larger than around five.

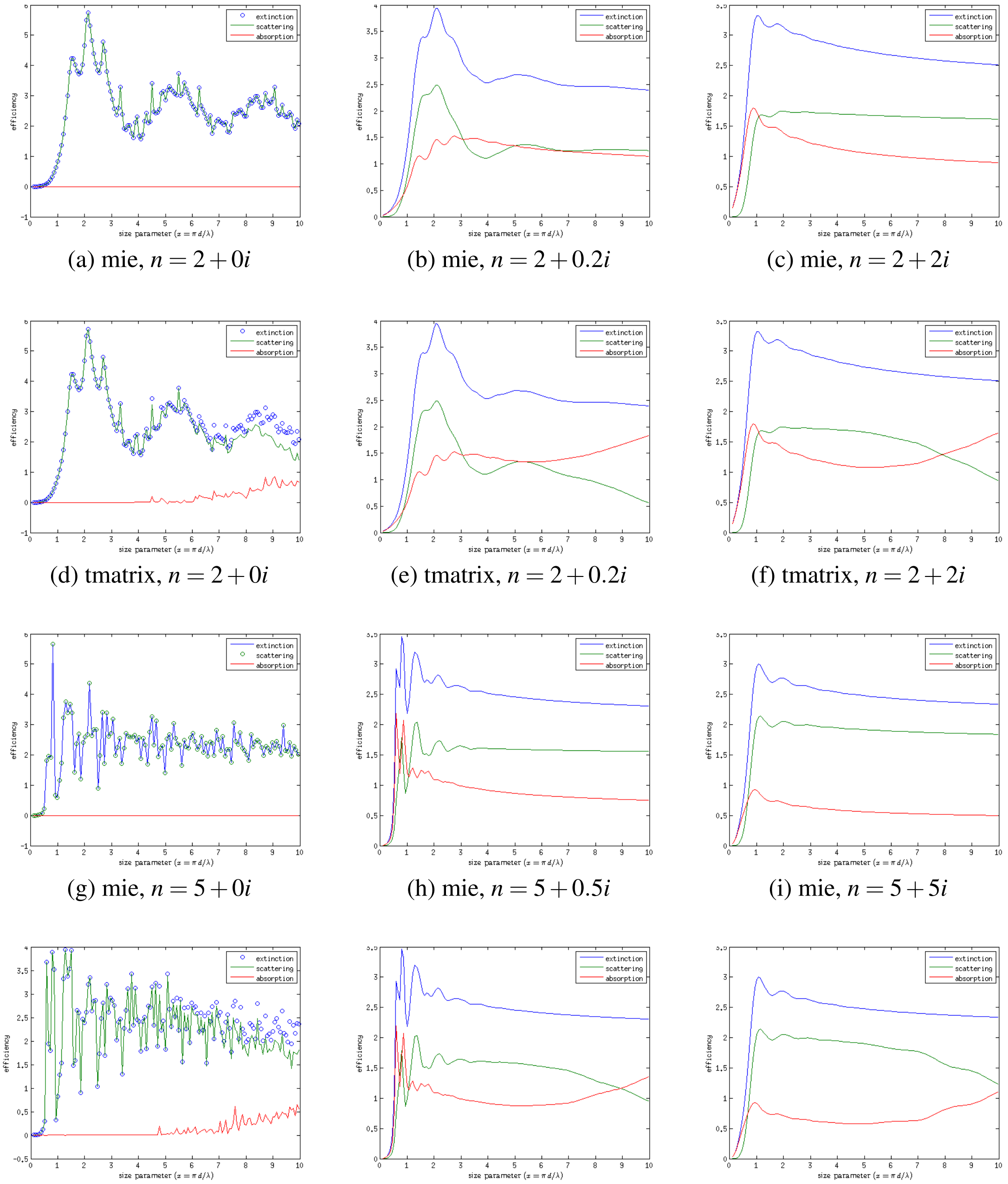

(a) mie, $n = 2 + 0i$
(b) mie, $n = 2 + 0.2i$
(c) mie, $n = 2 + 2i$
(d) tmatrix, $n = 2 + 0i$
(e) tmatrix, $n = 2 + 0.2i$
(f) tmatrix, $n = 2 + 2i$
(g) mie, $n = 5 + 0i$
(h) mie, $n = 5 + 0.5i$
(i) mie, $n = 5 + 5i$
(j) tmatrix, $n = 5 + 0i$
(k) tmatrix, $n = 5 + 0.5i$
(l) tmatrix, $n = 5 + 5i$

Figure 5.5: Absorption and scattering efficiencies as a function of the parameter x for spherical particles of the mentioned refractive indices, calculated with the Mie and T-matrix functions.

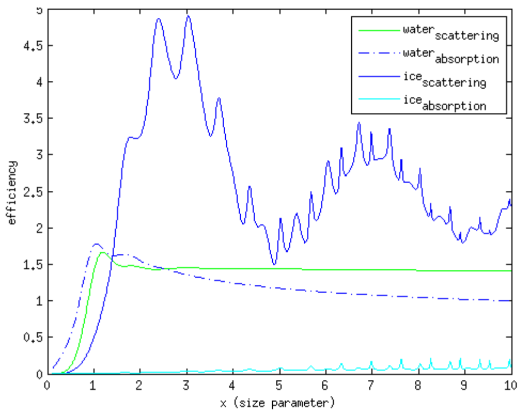

(a) Mie- 90 GHz

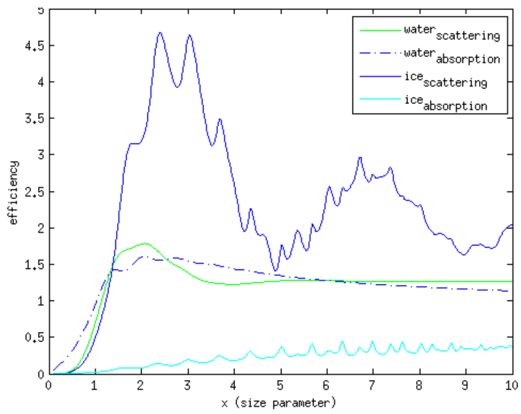

(b) Mie- 500 GHz

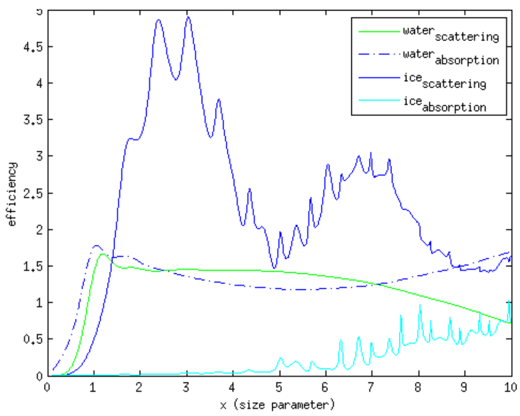

(c) tmatrix- 90 GHz

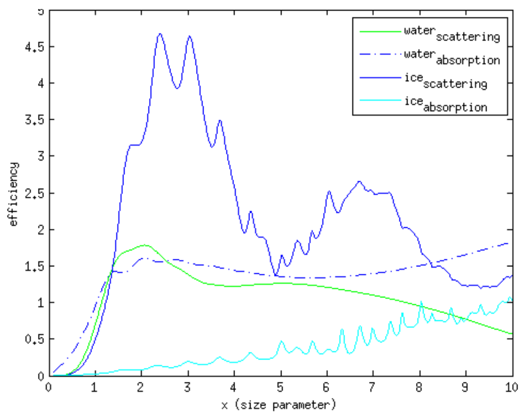

(d) tmatrix- 500 GHz

Figure 5.6: Absorption and scattering efficiencies as a function of x comparing results of the Lorenz-Mie and T-matrix methods. The temperature is set to 250 K.

6 Approximation by simple shape models

This chapter provides a comparison between single scattering properties of realistic ice particle shapes, such as different crystals and aggregates, with those of solid and soft spheres and spheroids. As mentioned earlier, the scattering properties of the realistic ice particle shapes considered throughout this study are from three publicly available DDA databases. The scattering properties inside three databases were derived by the DDA method, while the Lorenz-Mie and T-matrix methods are applied for sphere and spheroids (see section 5.1). Herein, all particles are compared based on their mass equivalent diameter (d_e) and size parameter (x) that are derived through equations 2.1 and 2.4. This implies that particles with the same mass are compared.

Similar comparisons between DDA results and simple shape models have been performed in several studies, like Liu [2004]; Kim [2006]; Nowell *et al.* [2013]; Liao *et al.* [2013]. Throughout these studies, a few frequencies and DDA shapes were considered and there is no comprehensive evaluation of simple shape models over a large range of particle sizes and frequencies.

In this study, we simultaneously compare a large set of DDA data from three databases (i.e., Liu [2008], Nowell *et al.* [2013], and Hong *et al.* [2009]) with the result of simple shape models in a broad range of frequency (90-874 GHz) and size parameters. Soft spheres and spheroids including various values of air fractions (f_{a}^{v}) are considered and different mixing rules are applied to see in what extent the average scattering properties of the DDA data can be approximated by simple shape models.

The single scattering properties considered in this chapter are absorption (Q_{abs}), scattering (Q_{sca}), and backscattering (Q_{bac}) efficiencies, and asymmetry parameter (g). The efficiencies are normalised with respect to the area of corresponding mass equivalent sphere (see equation 2.6 to 2.8). As the main focus of this study is on the passive microwave measurements, Q_{sca} and Q_{abs} parts are more pronounced and Q_{bac} (applied in active measurements) is less emphasised throughout this chapter. All the reference DDA databases assume completely random orientation for the particles. Accordingly this study is only concerned with particles that are completely randomly oriented.

This chapter provides a brief introduction of the DDA databases that are considered as reference. Then, comparisons of the reference data with simple shape models are presented.

6.1 DDA databases

Liu

Liu [2008] applied the DDA model developed by Draine and Flatau [2000] and computed single scattering properties (scattering cross section (C_{sca}), absorption cross section (C_{abs}), backscattering cross section (C_{bac}), asymmetry parameter (g), and phase function) of 11 types of randomly orientated ice particle crystal shapes for frequencies between 3 and 340 GHz, and for five different temperatures. The phase function (P_{11} in the scattering matrix) shows the angular distribution of the scattered energy in terms of 37 elements for every 5 degrees of zenith angle in range of $0-\pi$.

The scattering properties of particles are orientationally averaged at 16 β, 17 θ, and 16 φ. β, θ, and φ are three angles to describe the orientation of ice particles in Draine and Flatau [2000] DDA model.

The refractive index of ice applied in the DDA calculation is set by the Mätzler *et al.* [2006] model.

Nowell

A new snowflake aggregation model was developed by Nowell *et al.* [2013] and single scattering properties at different particle sizes are calculated through the DDA method developed by Draine and Flatau [2009], for 10 frequencies (10.65, 13.6, 18.7, 23.8, 35.6, 36.5, 89, 94, 165.5, and 183.31 GHz) at 263 K. The results provided are C_{sca}, C_{abs}, C_{bac}, and g. Note that there is neither information of phase function nor scattering matrix, consequently this DDA database can not be applicable in all radiative transfer equations (For details about an example of atmospheric radiative transfer simulator, the reader is referred to Eriksson *et al.* [2011a]).

The 6-bullet rosette is stated to be the most frequently observed crystal shape at the top of clouds and therefore was selected by Nowell *et al.* [2013] as constituent crystals to simulate three dimensional snowflake aggregates. These aggregates were allowed to grow in three dimensions and consequently they are quite spherical and follow Brandes *et al.* [2007] diameter-density parameterisation.

The refractive index of ice, that is applied in the DDA calculation, is derived by Mätzler *et al.* [2006] model.

Hong

Hong *et al.* [2009] applied the DDA model developed by Draine and Flatau [2004] to compute the scattering properties (extinction efficiency (Q_{ext}), absorption efficiency (Q_{abs}), single scattering albedo (ω), asymmetry parameter (g), and 8 elements of scattering phase matrix) of six randomly oriented nonspherical ice particles at 21 frequencies (90, 118, 157, 166, 183.3, 190, 203, 220, 243, 325, 340, 380, 425, 448, 463, 487, 500, 640, 664, 683, and 874 GHz) for a temperature of 243 K. The 8 elements of the scattering phase matrix are P_{11}, P_{12}, P_{21}, P_{22}, P_{33}, P_{34}, P_{43}, and P_{44} that each of them are estimated at 181 zenith angles from 0 to π.

The geometrical information of the six ice particle shapes is detailed in the Table 1 of Hong [2007]. To have the properties of a randomly oriented particle, β, θ, and φ are assumed in ranges of $0-2\pi$, $0-\pi$, and $0-2\pi$, and scattering quantities are averaged over different combinations of orientations. Refractive index of ice is taken from Warren [1984]. Eriksson *et al.* [2014] compared different ice refractive index parameterisations and concluded that the Warren [1984] is not a proper choice to calculate the ice refractive index. According to Figure 3.2, applying Warren [1984] leads to the overestimation of imaginary part and consequently absorption at frequencies up to 400 GHz, and underestimation of absorption at frequencies higher than 400 GHz. This should be noted when absorption data from Hong database is compared with the data from the Nowell and Liu ones.

6.2 Simple shape models

The possibly simplest shape to approximate the single scattering of randomly oriented ice crystals and aggregates, is by solid spheres. Other common simple models are soft sphere or spheroid, that are introduced in earlier chapters. Scattering properties of soft particles are affected by volume air fraction (f_{a}^{v}) of the components, and the mixing rule formula that is applied to calculate the refractive indices (n_{eff}). Generally, soft particles, regardless of f_{a}^{v} or the type of applied mixing rule, follow the general trend detected in the DDA data better than the solid ice particles. This is illustrated in Figure 6.1 where f_{a}^{v} is set to 0.7 and $\mathrm{MG}_{\mathrm{ai}}$ is applied to derive n_{eff}. All efficiencies and asymmetry parameter in Figure 6.1 are calculated at 183 GHz and for 243 K and plotted against x. The results for Q_{sca}, Q_{bac}, and g at other frequencies are quite similar to those of 183 GHz. This is due to the independence of the real part of the refractive index of ice particles to frequency. However, the imaginary part of the refractive index, that is responsible for absorption (Q_{abs}), shows a frequency dependency (see section 3.4). Throughout the microwave region, absorption is most pronounced for smaller particles (Eriksson *et al.* [2011b]). However, Eriksson *et al.* [2014] showed that the importance of absorption should be considered even for larger particles in the case of optically thick clouds. Furthermore, Kim [2006] indicated that the temperature dependency of refractive indices, makes only a trivial difference in single scattering properties at the microwave frequency range. In short, soft models likely provide a better representation of the DDA data compared to the solid sphere models at the microwave frequencies, for any temperature.

In following, firstly, the best fitting shape (sphere or spheroid) of soft models is selected. Secondly, the impact of different mixing models is examined. Finally, the impacts of choosing different air fractions (f_{a}^{v}), either the fixed or variable ones, are considered.

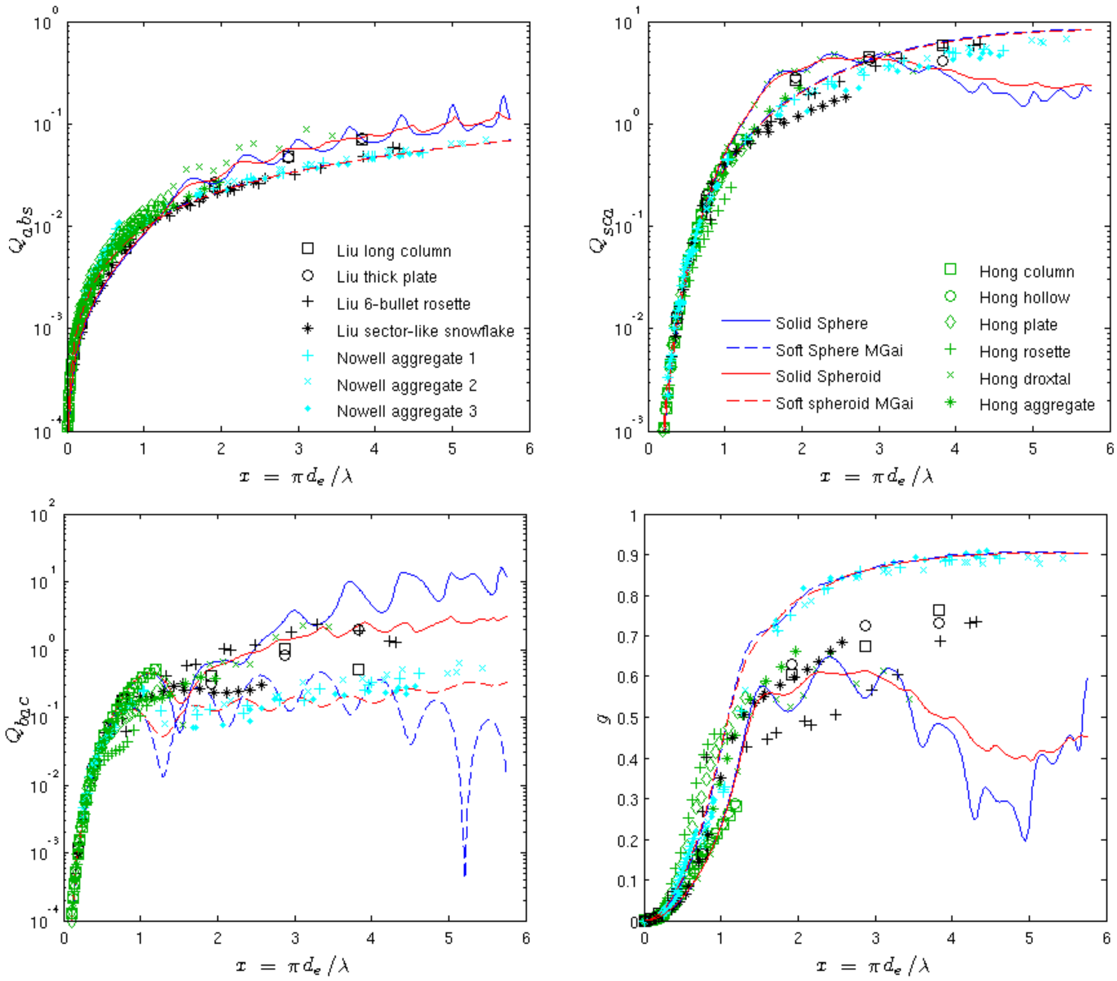

Figure 6.1: Single scattering properties calculated by the DDA method from Liu [2008], Hong *et al.* [2009], and Nowell *et al.* [2013] databases, compared with solid and soft spheres. f_a^v is set to 0.7 for soft models. The refractive indices of soft spheres and spheroids following Mätzler *et al.* [2006], are derived by MG_{ai} mixing rule. The results are computed for 183 GHz and 243 K, except Nowell *et al.* [2013] which are for 263 K.

6.2.1 Selection of shape

As a first step, we examined if the choice of a specific shape (sphere or spheroid) results in a better approximation of the DDA data. As shown in Figure 6.1, soft spheres and spheroids resulting in quite similar values in Q_{sca}, Q_{abs} and g. The main difference is discerned in Q_{bac}, where the DDA data are better followed by soft spheroids compared to soft spheres. Particularly, at $x > 1$, the soft spheres show a strong resonance phenomenon, that are dampened when soft spheroids are considered. Accordingly, soft spheroids are a better choice to represent the DDA data, mainly due to the Q_{bac} part. Liao *et al.* [2013] compared the DDA data from the Nowell database with soft models, at frequencies less than 183 GHz, and concluded that a randomly oriented spheroidal soft model is preferred over the spherical one.

Following Hogan *et al.* [2012], only oblate spheroids with axial ratio of 1.66 ($\alpha = 1.66$) are considered in this study. Northworthy, selection of α is not critical where a randomly oriented spheroid is considered. However, the ripple phenomenon appears in Q_{bac} part if a spheroid with a specific orientation (such as horizontally or vertically aligned) is considered.

6.2.2 Selection of mixing rule

As mentioned in section 3.4.1, three mixing rules (i.e., MG_{ai}, MG_{ia} and Bruggeman) are considered in this study. The soft spheroid models are compared to the DDA data in order to find out if choosing a particular mixing rule is preferred over the other types.

It is mentioned in section 6.1 that the three DDA databases used different ice refractive index parameterisations in their calculations. The Liu and Nowell databases applied Mätzler *et al.* [2006] and the Hong database used Warren [1984]. To homogenise these reference databases and make them comparable, we normalised all the DDA data with respect to mass-equivalent solid ice sphere as

$$r = \frac{C}{C^{solid}}, \tag{6.1}$$

where C is the cross section of concern (C_{sca}, C_{abs}, C_{bac}) of each DDA particle and C^{solid} is the corresponding cross section of the mass-equivalent solid ice sphere whose refractive index is derived by the same parameterisation as used for the calculation of C.

An example comparison of the normalised DDA data is shown in Figure 6.2. The results are presented for scattering ($r_{\text{sca}} = C_{\text{sca}}/C_{\text{sca}}^{Solid}$) and absorption ($r_{\text{abs}} = C_{\text{abs}}/C_{\text{abs}}^{Solid}$). Note that the dotted black lines with $r = 1$ represent scattering and absorption properties of solid ice spheres and all other data are normalised with respect to it. As shown in this figure, there is a spread in the DDA results with respect to the reference line (solid ice sphere). For example, r_{abs} of most of the DDA data are above 1 at $x < 1$, and this is reversed for $x > 1$. In the case of r_{sca}, the DDA data are above 1 for $x < 0.5$ and $x > 3.2$, and below 1 at $0.5 < x < 3.2$.

The scattering and absorption properties of the soft spheroid models are also normalised with respect to the mass-equivalent solid ice sphere and are included in Figure 6.2. The refractive in-

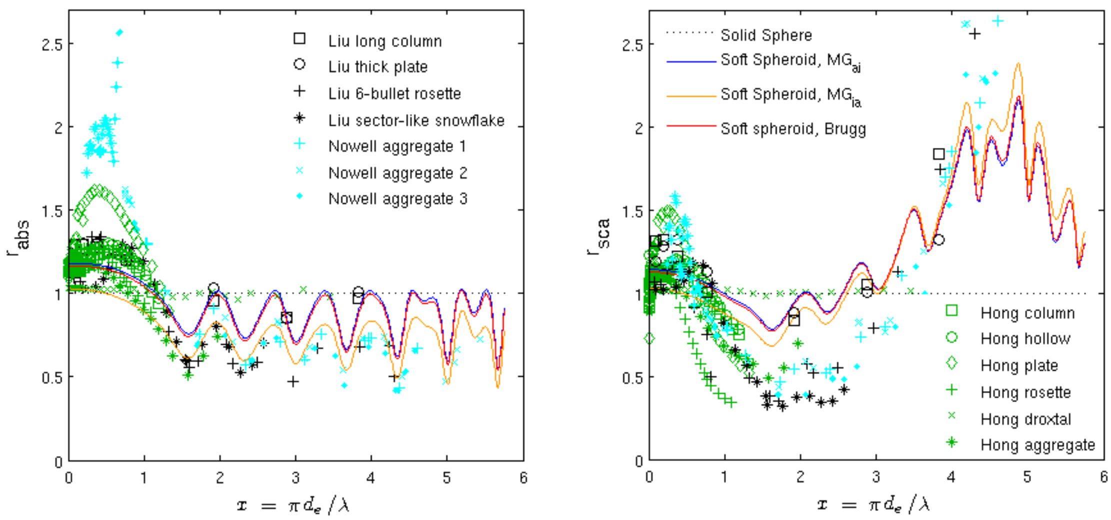

Figure 6.2: Absorption (left) and scattering (right) cross sections of the DDA data and soft spheroids, that are normalised by corresponding cross sections of solid ice spheres with the equivalent mass and the same refractive index applied for the generation of the DDA data. For soft spheroids (colored lines), f_a^v is set to 0.25 and their refractive indices are derived by three different mixing rules. Results are plotted for 183 GHz. Note that the dotted black line at 1, represents our reference of mass-equivalent solid ice spheres.

dices of the soft models are derived by the three different mixing rules. According to this figure, the scattering properties of the soft spheroids are throughout lower than the DDA data when $\mathrm{MG_{ia}}$ (Maxwell Garnett with ice inclusion in air matrix) is used. While, applying either $\mathrm{MG_{ai}}$ (air inclusion in ice matrix) or the Bruggeman mixing rules lead to a better representation of the average values of the DDA data. This remark is valid for both absorption and scattering parts, but it is more clear for r_{abs}. At $x < 1$, the average values of the DDA data for r_{abs} is about 1.2, but the r_{abs} obtained throughout applying the $\mathrm{MG_{ia}}$ is 1 or below 1.

To draw a general conclusion regarding the mixing rule selection, it is required to see if the differences between mixing rules can be compensated by adjusting the air fraction (f_a^v). A simple test of this type is found in Figure 6.3. The absorption ratios (r_{abs}) of soft spheroids of Figure 6.2 are computed as a function of f_a^v, and presented in the three left panels of Figure 6.3. The three right panels represent the same ratio with respect to both f_a^v and x. This figure confirms that r_{abs} of soft spheroids with their n_{eff} obtained by $\mathrm{MG_{ia}}$, is always below 1 at $x < 1$, independently of f_a^v. The same patterns (not shown) are found for other frequencies, as well as for r_{sca}.

That is, $\mathrm{MG_{ia}}$ is not a proper option to derive the n_{eff} of soft spheroids, as it results in an underestimated approximation of the average DDA absorption cross sections at $x < 1$.

Ratios reach values above 1 when the Bruggeman mixing rule is used. However, applying this mixing rule can not mimic the DDA data with high r_{abs}. As an example, the highest ratio reached by Bruggeman is about 1.27, while applying $\mathrm{MG_{ai}}$ leads to the values higher than 1.9. If we only consider the Nowell database (cyan points in Figure 6.2) at $x > 1$, the average ratio value for r_{abs}

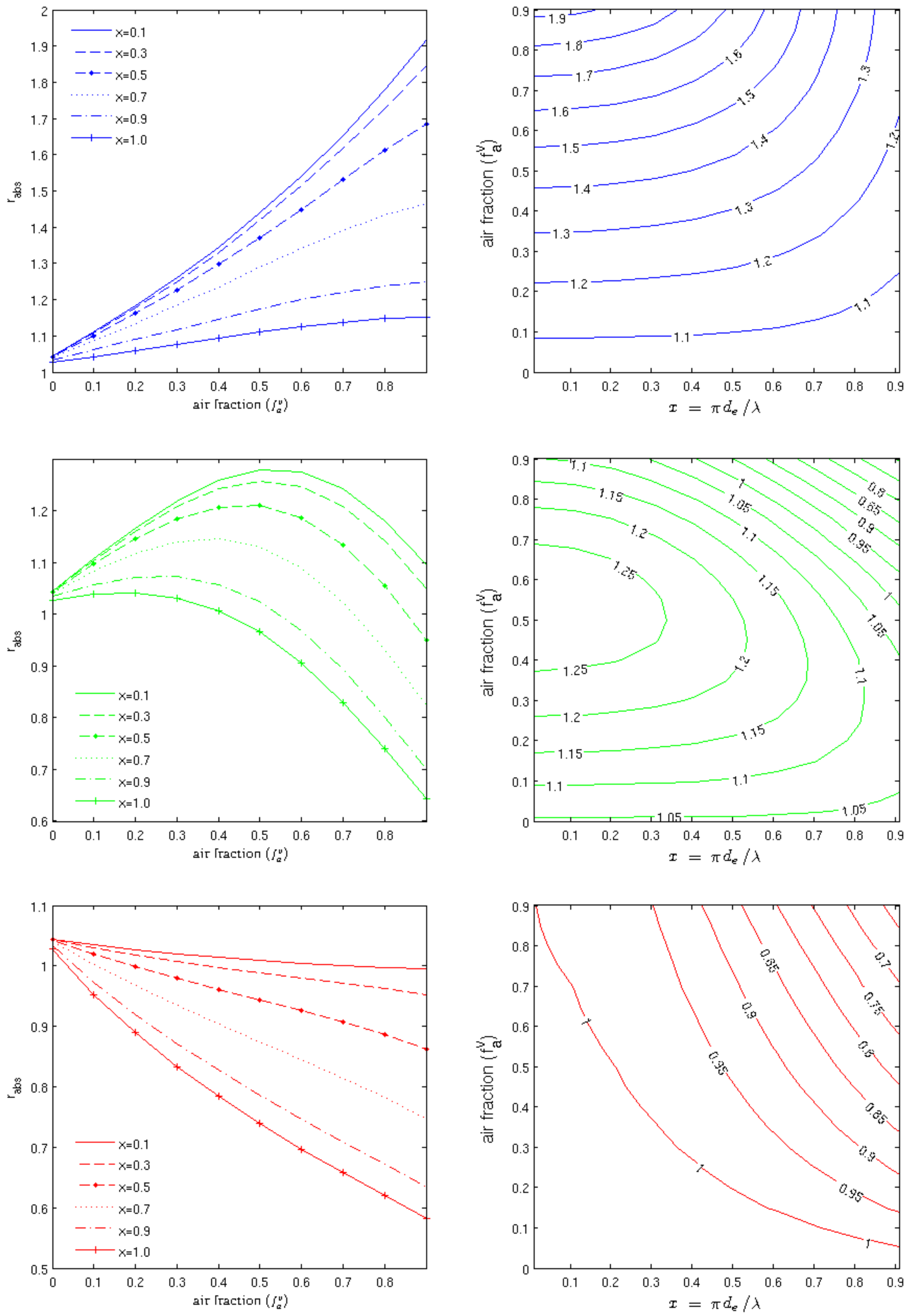

Figure 6.3: (left) absorption ratio (r_{abs}) of soft spheroids, for six size parameters, as a function of f_a^v and (right) r_{abs} contours as functions of both x and f_a^v for (blue) MG_{ai}, (green) Bruggeman, and (red) MG_{ia}. Results are for 183 GHz and for 243 K.

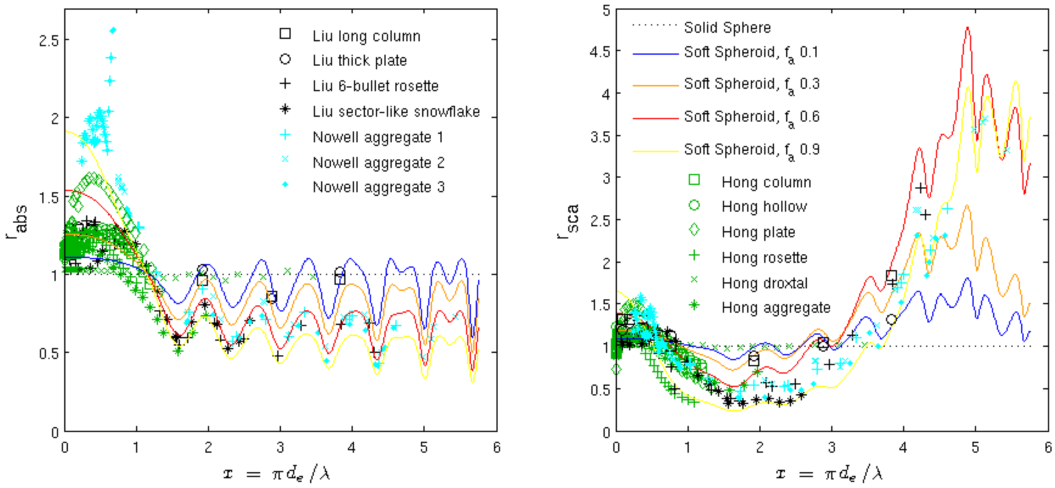

Figure 6.4: Scattering cross sections calculated by DDA from Liu [2008], Hong *et al.* [2009], and Nowell *et al.* [2013] databases database (points), and soft spheroids of different air fractions (f_a) (colored lines), normalised by corresponding properties of solid spheres with equivalent mass. The refractive indices of the soft spheres are derived by the MG_{ai} mixing rule. Results are plotted for 183 GHz and 263 K. Note that the dotted black line, represents our reference of mass-equivalent solid ice spheres.

and r_{sca} are respectively about 2 and 1.4, and therefore applying the Bruggeman mixing rule would not be a proper choice to approximate the average of the Nowell DDA data. So, the Bruggeman is not as satisfying as the MG_{ai}.

From what is discussed above, it can be concluded that, for $x \leq 1$, applying MG_{ai} leads to the best possible approximation of the DDA data, while using MG_{ia} results in an underestimation of optical properties, particularly for absorption. Accordingly, MG_{ai} is selected as mixing rule to mimic the average properties of the DDA results throughout this study.

6.2.3 Selection of air fraction

As discussed in section 3.3, air fraction (f_a^v) of a soft particle can be defined in two main ways, to be fixed and variable. Both approaches are investigated in following to find a f_a^v that gives the soft spheroid models the best fitting of the average properties of the DDA data.

Fixed air fraction

Absorption and scattering ratios (r_{abs} and r_{sca}) of soft spheroids, including four different f_a^v (ranging $0.1-0.9$), are shown along with r_{abs} and r_{sca} of the DDA data in Figure 6.4. Based on the conclusion of section 6.2.2, n_{eff} of the soft spheroids is derived by MG_{ai}. This figure confirms that to represent the average properties of the DDA data, f_a^v of the soft spheroid models must vary with size (x). In other words, it is not possible to consider a single air fraction for a soft spheroid model and mimic the average properties at a broad range of x. For example, the DDA results at smaller

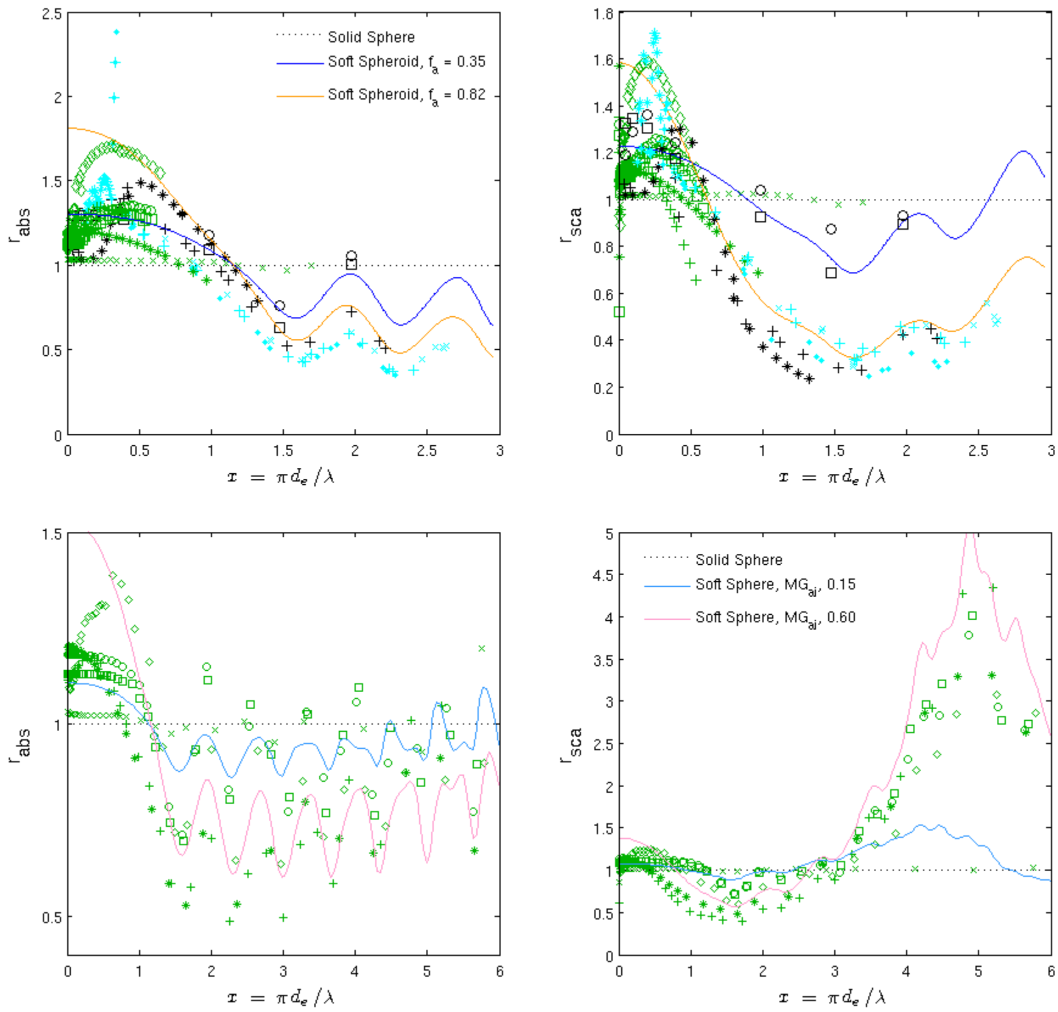

Figure 6.5: Scattering cross sections calculated by DDA from Liu [2008], Hong *et al.* [2009], and Nowell *et al.* [2013] databases database (points), and soft spheroids of two air fractions (f_a) (colored lines), normalised by corresponding properties of solid spheres with equivalent mass. The refractive indices of the soft spheres are derived by the MG_{ai} mixing rule. Results are plotted (above panels) for 94 GHz and (below panels) 874 GHz. Note that the dotted black line, represents our reference of mass-equivalent solid ice spheres.

size parameters ($x < 1$), can be approximated by soft spheroids whose air fraction is $0.1 - 0.3$. At larger x, larger air fractions ($f_a^v > 0.6$) are required. This is expected because smaller particles should have low air fraction as they tend to be closer to solid ice spheres. The particles become softer as they become larger. This trend promotes an idea of using a set of two air fractions, i.e., one lower air fraction at smaller x, and one higher air fraction at larger x.

Example results of applying a set of two air fractions are found in Figure 6.5. This figure shows two facts. Firstly, both absorption and scattering properties (together are referred as extinction that is applied in passive measurement) can not be simultaneously approximated by a single air fraction. For example, $f_a^v = 0.35$ gives an acceptable fit for r_{abs} at 94 GHz at $x < 1$, but for r_{sca} this f_a^v results in too high values at $0.6 < x < 1$. Therefore, at e.g. $0.6 < x < 1$, if the f_a^v that gives the best fit with respect to absorption properties is selected for the soft model, the scattering part would be overestimated; and reversely, if the f_a^v that matches best with respect to scattering properties is assumed for the model, the absorption properties would be overestimated. Furthermore, considering backscattering (applied in active measurements) and asymmetry properties, Eriksson *et al.* [2014] showed that a single air fraction can not work concurrently for all four optical properties.

Secondly, the best air fraction fit has a frequency dependence. At 874 GHz, $f_a^v = 0.6$ mimics the average scattering properties of the DDA data at $0.7 < x < 3$, but at e.g. 94 GHz this f_a^v overestimates the scattering properties at the same particle size. The frequency dependency of air fraction implies a limitation to apply a soft model in a broad range of frequencies. For example to retrieve the IWC from a cloud signal that is simultaneously observed by CloudSat (at 94 GHz) and Odin-SMR (at 500 GHz), two different soft spheroid models should be considered as the initial assumption on the microphysical properties of particles (see diagram 1.1). Due to the differences of the initial assumptions, the IWC that is retrieved from CloudSat data can not be used to constrain the retrieval of the IWC profiles from Odin-SMR data and vice versa (The reader is referred to Rydberg *et al.* [2009] for more details).

Variable air fraction

As discussed in section 3.3, the air fraction of a soft model can be varied as a function of x, if the effective density (ρ_{eff}) of the particle is derived by a size-density parameterisation.

Example results of two soft models with variable air fractions are found in Figure 6.6. The soft spheroid model of Hogan *et al.* [2012] (referred as HSP) follows the density parameterisation of Brown and Francis [1995], that leads to air fractions close to 1 at $d_e \geq 350\,\mu$m (see Figure 4.2). It implies that the HSP becomes too soft already at $x \simeq 0.7$ ($d_e = 350$ corresponds to $x = 0.7$ at 183 GHz) and results deviations of the scattering properties from the average DDA data already at $x \simeq 0.7$ (see right panel of Figure 6.6). The soft spheroidal model of Baran, that follows density parameterisation of Baran *et al.* [2011b], also generates too soft particles at $x \geq 0.7$.

Furthermore, the air fraction based on some size-density parameterisations is independent of frequency, but as discussed earlier, the best fitted air fraction should vary with respect to frequency.

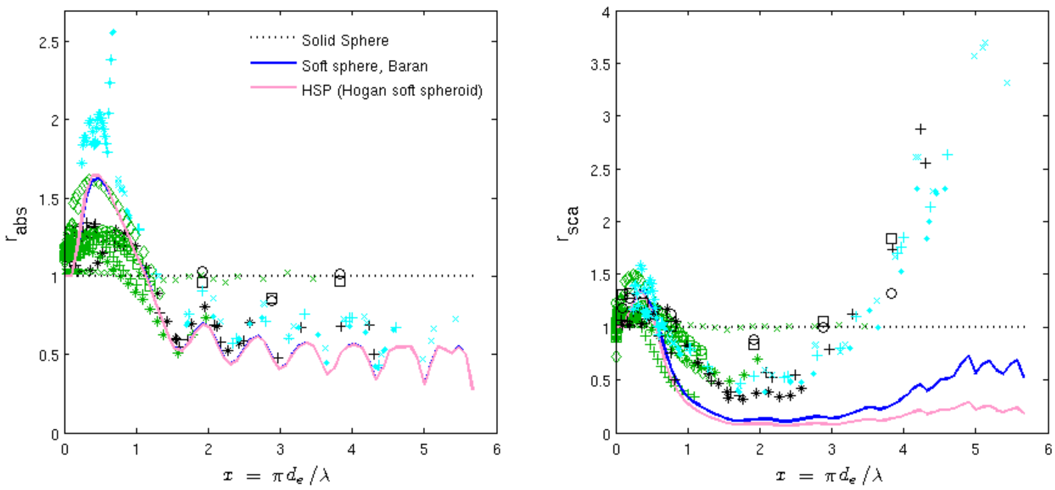

Figure 6.6: Scattering cross sections of DDA data set as Figure 6.4 along with two soft models from Baran *et al.* [2011a] and Hogan *et al.* [2012] assuming the variable air fraction based on the size-density parameterisations. Results are plotted for 183 GHz and 263 K. Note that the dotted black line, represents our reference of mass-equivalent solid ice spheres.

This signifies that a single soft model whose air fraction follows some size-density parameterisations can not mimic the average of the DDA data in a broad range of frequencies. In fact, Eriksson *et al.* [2014] examined the soft models at other frequencies and concluded that setting the variable air fraction can in the best case work only in frequency ranges up to 35 GHz.

Eriksson *et al.* [2014] investigated the impact of applying different air fractions (f_{a}^{v}) on the soft spheroid models in a broad range of frequencies and also presented the results for backscattering properties ($r_{\mathrm{bac}} = C_{\mathrm{bac}}/C_{\mathrm{bac}}^{Solid}$) and concluded that the soft spheroid models with a $f_{\mathrm{a}}^{v} \simeq 0.25$ can mimic the average optical properties of the three reference DDA data up to $x \approx 0.5$. At $x > 0.5$, the air fractions of the soft models require to vary with x and frequencies to match with the average of the DDA data.

7 Summary and Conclusion

The optical properties of some ice crystals and aggregates from three publicly available DDA databases (i.e., Liu [2008], Hong *et al.* [2009], and Nowell *et al.* [2013]) were compared in order to find a simple shape model that can approximately represent the average properties of the considered reference data. Since this study was concerned with improving the ice mass retrieval, all particles were compared with respect to their equivalent mass ice sphere diameter, d_e. In the context of this study, solid (consisting of pure ice) and soft (homogeneous mixture of ice and air) sphere and spheroid models were considered.

The main focus of this study was to investigate the applicability of soft particle models in representing the real microphysical state of ice particles with respect to retrieving the ice mass by microwave observation. The impacts of applying different mixing rules and air fractions, to adjust the refractive indices of the soft particle models in a way that they can mimic the average optical properties of the reference DDA data, were examined.

Firstly, it was concluded that soft spheroid models are preferred over soft sphere models, mainly due to the differences in Q_bac (backscattering). The backscattering properties of the DDA data are better followed by soft spheroids compared to soft spheres.

Secondly, it was found that irrespective of the value chosen for the air fraction, the Maxwell Garnett mixing rule with ice as inclusion and air as matrix media (referred as $\mathrm{MG_{ia}}$) tended to underestimate the imaginary part of the refractive indices and accordingly underestimate the absorption and scattering properties at lower size parameters ($x < 1$). Therefore, the Maxwell Garnett mixing rule with air as inclusion and ice as matrix ($\mathrm{MG_{ai}}$) was selected throughout this study.

Thirdly, it was concluded that a soft spheroidal model with a single fixed air fraction could not represent the average properties of the DDA data. Particularly, at larger size parameters ($x > 0.5$), the air fraction should vary with x. At least two air fractions are required, one at $x < 0.5$, and another at $x > 0.5$.

It was found that a soft spheroidal model with an air fraction on the order of 0.1 to 0.3 can approximate the average extinction properties of the DDA data at $x < 0.6$ across the considered frequencies (90 - 874 GHz). At $x > 0.5$, the best fitting air fraction showed a frequency dependence. This implies a drawback on applying a soft spheroid model in a broad range of frequencies.

Furthermore, the Baran and Hogan soft models were compared to the DDA data. The air fractions of these two soft models were respectively set to follow Brown and Francis [1995] and

Baran *et al.* [2011a] size-density parameterisations, implying that their air fractions vary as a function of x. It was shown that these soft models were too soft at already $x \approx 0.7$ (at 183 GHz) to mimic the average extinction properties of the reference data. Eriksson *et al.* [2014] examined the Hogan soft model at other frequencies and concluded that the selection of air fraction based on size-density parameterisations can in the best case only work in frequency ranges up to 35 GHz.

In line with the discussion above, it can be concluded that soft spheroidal models can be tuned to work only in a narrow scope and they are not proper choices for representing the average optical properties in a broad range of x and frequencies. The reason of this is that the best fitted air fraction should vary with both x and frequencies at $x > 0.5$. Eriksson *et al.* [2014] confirmed that soft spheroid models work quite well at $x < 0.5$ across the broad range of frequencies.

In this study three DDA databases consisting optical properties of completely oriented ice particles were compared. Several studies, like Hogan *et al.* [2012] revealed that ice particles have a preference to be horizontally oriented. Therefore, new DDA databases consisting optical properties of oriented ice crystals and aggregates should be generated to get a more accurate and statistically sound results for future studies like this.

Overall, since the usage of the soft models is problematic, it can be said that the future work of approximation of the DDA data should focus on finding another particle shape to represents the mean optical properties. According to both Geer and Baordo [2014] and Eriksson *et al.* [2014], the sector-like snowflake particles of the Liu database can roughly mimic the average optical properties of the DDA data, and accordingly can provide a better representation of the real case in the atmosphere.

Bibliography

Baran, A., Bodas-Salcedo, A., Cotton, R., Lee, C., *et al.* (2011a). Simulating the equivalent radar reflectivity of cirrus at 94 GHz using an ensemble model of cirrus ice crystals: a test of the met office global numerical weather prediction model. *Quarterly Journal of the Royal Meteorological Society*, **137**(659), 1547–1560.

Baran, A. J., Connolly, P. J., Heymsfield, A., and Bansemer, A. (2011b). Using in situ estimates of ice water content, volume extinction coefficient, and the total solar optical depth obtained during the tropical active campaign to test an ensemble model of cirrus ice crystals. *Quarterly Journal of the Royal Meteorological Society*, **137**(654), 199–218.

Bohren, C. F. and Battan, L. J. (1980). Radar backscattering by inhomogeneous precipitation particles. *Journal of the Atmospheric Sciences*, **37**(8), 1821–1827.

Brandes, E. A., Ikeda, K., Zhang, G., Schönhuber, M., and Rasmussen, R. M. (2007). A statistical and physical description of hydrometeor distributions in Colorado snowstorms using a video disdrometer. *Journal of applied meteorology and climatology*, **46**(5), 634–650.

Brown, P. R. and Francis, P. N. (1995). Improved measurements of the ice water content in cirrus using a total-water probe. *Journal of Atmospheric and Oceanic Technology*, **12**(2), 410–414.

Bruggeman, V. D. (1935). Berechnung verschiedener physikalischer konstanten von heterogenen substanzen. i. dielektrizitätskonstanten und leitfähigkeiten der mischkörper aus isotropen substanzen. *Annalen der physik*, **416**(7), 636–664.

Buehler, S., Jimenez, C., Evans, K., Eriksson, P., Rydberg, B., Heymsfield, A., Stubenrauch, C., Lohmann, U., Emde, C., John, V., *et al.* (2007). A concept for a satellite mission to measure cloud ice water path, ice particle size, and cloud altitude. *Quarterly Journal of the Royal Meteorological Society*, **133**(S2), 109–128.

Debye, P. (1929). *Polar molecules*. New York : The Chemical Catalog Company, inc.

Delanoë, J. and Hogan, R. J. (2010). Combined cloudsat-calipso-modis retrievals of the properties of ice clouds. *Journal of Geophysical Research: Atmospheres (1984–2012)*, **115**(D4).

Draine, B. T. and Flatau, P. J. (2000). User guide for the discrete dipole approximation code DDSCAT (version 5a10). *arXiv preprint astro-ph/0008151*.

Draine, B. T. and Flatau, P. J. (2004). User guide for the discrete dipole approximation code DDSCAT 6.1. *(available at:http://arXiv.org/abs/astro-ph/0409262v2)*.

Draine, B. T. and Flatau, P. J. (2009). User guide for the discrete dipole approximation code DDSCAT 7.0. *(available at:http://arXiv.org/abs/0809.0337v5)*.

Draine, B. T. and Flatau, P. J. (2012). User Guide for the Discrete Dipole Approximation Code DDSCAT 7.2. *ArXiv e-prints*.

Eriksson, P., Buehler, S., Davis, C., Emde, C., and Lemke, O. (2011a). ARTS, the atmospheric radiative transfer simulator, version 2. *Journal of Quantitative Spectroscopy and Radiative Transfer*, **112**(10), 1551–1558.

Eriksson, P., Rydberg, B., and Buehler, S. A. (2011b). On cloud ice induced absorption and polarisation effects in microwave limb sounding. *Journal of Atmospheric Measurement Techniques*, **4**(6), 1305–1318.

Eriksson, P., Jamali, M., Mendrok, J., and Buehler, S. (2014). On the microwave optical properties of randomly oriented ice hydrometeors. *Atmospheric Measurement Techniques Discussions*, **7**(12), 12873–12927.

Evans, K. F. and Stephens, G. L. (1995). Microwave radiative transfer through clouds composed of realistically shaped ice crystals. part II. remote sensing of ice clouds. *Journal of the atmospheric sciences*, **52**, 2058–2072.

Fabry, F. and Szyrmer, W. (1999). Modeling of the melting layer. Part II: Electromagnetic. *Journal of Atmospheric Sciences*, **56**(20), 3593–3600.

Garnett, J. M. (1906). Colours in metal glasses, in metallic films, and in metallic solutions. ii. *Philos. Trans. Roy. Soc. London*, pages 237–288.

Geer, A. and Baordo, F. (2014). Improved scattering radiative transfer for frozen hydrometeors at microwave frequencies. *Atmospheric Measurement Techniques*, **7**(6), 1839–1860.

Harries, J. E. (2000). Physics of the Earth's radiative energy balance. *Contemporary Physics*, **41**, 309–322.

Heymsfield, A. J. and Miloshevich, L. M. (1995). Relative humidity and temperature influences on cirrus formation and evolution: Observations from wave clouds and FIRE II. *Journal of the atmospheric sciences*, **52**(23), 4302–4326.

Heymsfield, A. J. and Miloshevich, L. M. (2003). Parameterizations for the cross-sectional area and extinction of cirrus and stratiform ice cloud particles. *Journal of the atmospheric sciences*, **60**(7), 936–956.

Hogan, R. J., Tian, L., Brown, P. R., Westbrook, C. D., Heymsfield, A. J., and Eastment, J. D. (2012). Radar scattering from ice aggregates using the horizontally aligned oblate spheroid approximation. *Journal of Applied Meteorology and Climatology*, **51**(3), 655–671.

Hong, G. (2007). Parameterization of scattering and absorption properties of nonspherical ice crystals at microwave frequencies. *Journal of Geophysical Research: Atmospheres (1984–2012)*, **112**(D11).

Hong, G., Yang, P., Baum, B. A., Heymsfield, A. J., Weng, F., Liu, Q., Heygster, G., and Buehler, S. A. (2009). Scattering database in the millimeter and submillimeter wave range of 100–1000 GHz for nonspherical ice particles. *Journal of Geophysical Research: Atmospheres (1984–2012)*, **114**(D6).

Jiang, J. H. and Wu, D. L. (2004). Ice and water permittivities for millimeter and sub-millimeter remote sensing applications. *Atmospheric Science Letters*, **5**(7), 146–151.

Johnson, B. T., Petty, G. W., and Skofronick-Jackson, G. (2012). Microwave properties of ice-phase hydrometeors for radar and radiometers: Sensitivity to model assumptions. *Journal of Applied Meteorology and Climatology*, **51**(12), 2152–2171.

Kim, M.-J. (2006). Single scattering parameters of randomly oriented snow particles at microwave frequencies. *Journal of Geophysical Research: Atmospheres (1984–2012)*, **111**(D14).

Knoll, G. F. (2010). *Radiation detection and measurement*. John Wiley & Sons.

Liao, L., Meneghini, R., Nowell, H. K., and Liu, G. (2013). Scattering computations of snow aggregates from simple geometrical particle models. *Selected Topics in Applied Earth Observations and Remote Sensing, IEEE Journal of*, **6**(3), 1409–1417.

Liebe, H., Hufford, G., and Cotton, M. (1993). Propagation modeling of moist air and suspended water/ice particles at frequencies below 1000 GHz. In *In AGARD, Atmospheric Propagation Effects Through Natural and Man-Made Obscurants for Visible to MM-Wave Radiation 11 p (SEE N94-30495 08-32)*, volume 1.

Liou, K. (2002). *An Introduction to Atmospheric Radiation*. International Geophysics. Elsevier Science.

Liu, G. (2004). Approximation of single scattering properties of ice and snow particles for high microwave frequencies. *Journal of the atmospheric sciences*, **61**(20), 2441–2456.

Liu, G. (2008). A database of microwave single-scattering properties for nonspherical ice particles. *Bulletin of the American Meteorological Society*, **89**(10), 1563–1570.

Locatelli, J. D. and Hobbs, P. V. (1974). Fall speeds and masses of solid precipitation particles. *Journal of Geophysical Research*, **79**, 2185–2197.

Mätzler, C. (2002). Matlab functions for Mie scattering and absorption, version 2. *IAP Res. Rep*, **8**.

Mätzler, C., of Engineering, I., and Technology (2006). *Thermal Microwave Radiation: Applications for Remote Sensing*. IET electromagnetic waves series. Institution of Engineering and Technology.

Meneghini, R. and Liao, L. (1996). Comparisons of cross sections for melting hydrometeors as derived from dielectric mixing formulas and a numerical method. *Journal of Applied Meteorology*, **35**(10), 1658–1670.

Mishchenko, M. I., Travis, L. D., and Mackowski, D. W. (1996). T-matrix computations of light scattering by nonspherical particles: a review. *Journal of Quantitative Spectroscopy and Radiative Transfer*, **55**(5), 535–575.

Mishchenko, M. I., Travis, L. D., and Lacis, A. A. (2002). *Scattering, absorption, and emission of light by small particles*. Cambridge university press.

Mitchell, D. L., Zhang, R., and Pitter, R. L. (1990). Mass-dimensional relationships for ice particles and the influence of riming on snowfall rates. *Journal of applied meteorology*, **29**(2), 153–163.

Nakaya, U. and Terada Jr, T. (1935). Simultaneous observations of the mass, falling velocity and form of individual snow crystals. *Journal of the Faculty of Science, Hokkaido Imperial University. Ser. 2*, **1**(7), 191–200.

Nowell, H., Liu, G., and Honeyager, R. (2013). Modeling the microwave single-scattering properties of aggregate snowflakes. *Journal of Geophysical Research: Atmospheres*, **118**(14), 7873–7885.

Rydberg, B., Eriksson, P., Buehler, S., and Murtagh, D. P. (2009). Non-gaussian bayesian retrieval of tropical upper tropospheric cloud ice and water vapour from Odin-SMR measurements. *Journal of Atmospheric Measurement Techniques*, **2**(2), 621–637.

Sihvola, A. (2000). Mixing rules with complex dielectric coefficients. *Journal of Subsurface Sensing Technologies and Applications*, **1**, 393.

Thomas, G. E. and Stamnes, K. (2002). *Radiative transfer in the atmosphere and ocean*. Cambridge University Press.

Warren, S. G. (1984). Optical constants of ice from the ultraviolet to the microwave. *Applied optics*, **23**(8), 1206–1225.

Warren, S. G. and Brandt, R. E. (2008). Optical constants of ice from the ultraviolet to the microwave: A revised compilation. *Journal of Geophysical Research: Atmospheres (1984–2012)*, **113**(D14).

Wu, D. L., Jiang, J. H., Read, W. G., Austin, R. T., Davis, C. P., Lambert, A., Stephens, G. L., Vane, D. G., and Waters, J. W. (2008). Validation of the Aura MLS cloud ice water content measurements. *Journal of Geophysical Research: Atmospheres (1984–2012)*, **113**(D15).

Yang, P., Baum, B. A., Heymsfield, A. J., Hu, Y. X., Huang, H.-L., Tsay, S.-C., and Ackerman, S. (2003). Single-scattering properties of droxtals. *Journal of Quantitative Spectroscopy and Radiative Transfer*, **79**, 1159–1169.

Zhang, C., Lee, K.-S., Zhang, X.-C., Wei, X., and Shen, Y. (2001). Optical constants of ice ih crystal at terahertz frequencies. *Applied Physics Letters*, **79**(4), 491–493.

Appendix A Paper A

On the microwave optical properties of randomly oriented ice hydrometeors

P. Eriksson, M. Jamali, J. Mendrok, and S. A. Buehler.

Received: 2 December 2014 – Accepted manuscript: 3 December 2014 – Published in Atmospheric Measurement Techniques Discussion: 21 December 2014

Correspondence to: P. Eriksson (patrick.eriksson@chalmers.se)

Published by Copernicus Publications on behalf of the European Geosciences Union.

Atmos. Meas. Tech. Discuss., 7, 12873–12927, 2014
www.atmos-meas-tech-discuss.net/7/12873/2014/
doi:10.5194/amtd-7-12873-2014

Atmospheric Measurement Techniques
Discussions
Open Access

This discussion paper is/has been under review for the journal Atmospheric Measurement Techniques (AMT). Please refer to the corresponding final paper in AMT if available.

On the microwave optical properties of randomly oriented ice hydrometeors

P. Eriksson[1], M. Jamali[1], J. Mendrok[2], and S. A. Buehler[3]

[1]Earth and Space Sciences, Chalmers University of Technology, 41296 Gothenburg, Sweden
[2]Division of Space Technology, Lulea University of Technology, 98128 Kiruna, Sweden
[3]Meteorological Institute, Center for Earth System Research and Sustainability, University of Hamburg, Bundesstrasse 55, 20146 Hamburg, Germany

Received: 2 December 2014 – Accepted: 3 December 2014 – Published: 21 December 2014

Correspondence to: P. Eriksson (patrick.eriksson@chalmers.se)

Published by Copernicus Publications on behalf of the European Geosciences Union.

Abstract

Microwave remote sensing is important for observing the mass of ice hydrometeors. One of the main error sources of microwave ice mass retrievals is that approximations around the shape of the particles are unavoidable. One common approach to represent particles of irregular shape is the soft particle approximation (SPA). We show that it is possible to define a SPA that mimics mean optical particles of available reference data over narrow frequency ranges, considering a single observation technique at the time, but SPA does not work in a broader context. Most critically, the required air fraction varies with frequency and application, as well as with particle size. In addition, the air fraction matching established density parameterisations results in far too soft particles, at least for frequencies above 90 GHz. That is, alternatives to SPA must be found.

One alternative was recently presented by Geer and Baordo (2014). They used a sub-set of the same reference data and simply selected as "shape model" the particle type giving the best overall agreement with observations. We present a way to perform the same selection of a representative particle shape, but without involving assumptions on particle size distribution and actual ice mass contents. Only an assumption on the occurrence frequency of different particle shapes is still required. Our analysis leads to the same selection of representative shape as found by Geer and Baordo (2014). In addition, we show that the selected particle shape has the desired properties also at higher frequencies as well as for radar applications.

Finally, we demonstrate that in this context the assumption on particle shape is likely less critical when using mass equivalent diameter to characterise particle size, compared to using maximum dimension, but a better understanding of the variability of size distributions is required to fully characterise the advantage.

Further advancements on these subjects are presently difficult to achieve due to a lack of reference data. One main problem is that most available databases of pre-calculated optical properties assume completely random particle orientation, while for certain conditions a horizontal alignment is expected. In addition, the only database

covering frequencies above 340 GHz has a poor representation of absorption as it is based on outdated refractive index data, as well as only covering particles having a maximum dimension below 2 mm and a single temperature.

1 Introduction

Microwave techniques are gaining in importance for satellite observations of hydrometeors, i.e. clouds and precipitation. The main measurement target of microwave sensors is mass content estimates, possibly in the form of a precipitation rate. The detection mechanism used (absorption or scattering) depends on phase (liquid, ice or mixed), frequency, and on whether the instrument is active or passive. For example, for non-precipitating liquid droplets passive measurements rely on absorption, while radars rely on back-scattering. The signature of ice hydrometeors in passive data is a mix of scattering and absorption features, where in general the scattering part dominates (Sect. 4).

The accuracy of the retrievals depends on technique applied and a number of variables, including observational noise and limitations in the radiative transfer code used. However, the main retrieval error sources are frequently uncertainties associated with the microphysical state of the particles, i.e. phase, size, shape and orientation. This study focuses on the impact of assumed shape, that is probably the microphysical quantity with least hope of being retrievable based on microwave data alone. Information on particle size can be obtained by combining data from different frequencies (Evans and Stephens, 1995a; Buehler et al., 2007; Jiménez et al., 2007), while the phase of the particles is largely determined by the atmospheric temperature. Measuring horizontal and vertical polarisation simultaneously reveals if the particles have a tendency to horizontal alignment or if their orientation is completely random (e.g. Hall et al., 1984; Hogan et al., 2003; Davis et al., 2005; Eriksson et al., 2011b).

Shape is normally not a critical aspect for purely liquid particles, as they are throughout quasi-spherical. The deviation from a strict spherical shape increases with droplet

size and fall speed. On the other hand, the shape of frozen hydrometeors is highly variable, both as single crystals (needles, plates, columns, rosettes, dendrites, etc.) and as aggregates (see reviews by Heymsfield and McFarquhar, 2002; Baran et al., 2011). The shape is frequently denoted as the habit. It is unlikely that the air volume sampled contains a single ice particle shape, i.e. a habit mix can be expected. Furthermore, this mix normally varies with particle size. In principle, the shape of each particle should be known to avoid a related retrieval error, but this is not a feasible goal. Instead some “shape model” must be applied and the main aim of this study is to examine such models for microwave sounding of pure ice hydrometeors.

Considering the ice particles to be solid spheres is probably still the main microwave shape model. This approach is for example used in the standard 2B-CWC-O CloudSat retrievals by Austin et al. (2009). It is also applied in e.g. the Community Radiative Transfer Model (CRTM, Liu et al., 2013). Accordingly, retrieval systems (e.g. Boukabara et al., 2013; Gong and Wu, 2014) and radiance assimilation based on CRTM inherit the assumption of solid spheres. Furthermore, this particle type has throughout been assumed in cloud ice retrievals based on limb sounding data (Wu et al., 2008; Rydberg et al., 2009; Millán et al., 2013). A main reason for the popularity of this shape model is that the single scattering properties are simply calculated by well-established Mie codes.

Another common model is the “soft particle approximation” (SPA) where the particles are treated to consist of a homogeneous mix of ice and air. This approach requires that the volume or mass fraction of air and the corresponding refractive index of the ice-air mix are determined, see Sects. 2 and 5. SPA could in principle be used with a range of simplified particle forms, but it seems that only spheres and spheroids have been used so far. Spheroids are not treated by Mie theory, but are covered by the also computationally efficient T-matrix method (Mishchenko et al., 1996). One application of SPA for practical retrievals is Zhao and Weng (2002). A more recent example is Hogan et al. (2012), arguing for using a soft spheroid model for cloud radar inversions. In addition, SPA has widely been used in studies to mimic measured radiances by radiative transfer tests (e.g. Bennartz and Petty, 2001; Skofronick-Jackson et al., 2002; Doherty et al., 2007; Meirold-Mautner et al., 2007; Kulie et al., 2010) where the air fraction is either set to be fixed or derived from some parametric relationship between particle size and effective density.

Single scattering properties for arbitrary particle shapes can be calculated by e.g. the Discrete Dipole Approximation (DDA, Draine and Flatau, 1994). For example, DDA is used for incorporating realistic particle shapes in the retrievals presented by Evans et al. (2012). This study is likely the most ambitious microwave retrieval set-up with regards to particle shape, but it deals only with a specific measurement campaign and it does not provide any general conclusions. Publicly available databases of DDA results for common particle shapes are reviewed in Sect. 3. These databases were used by Kulie et al. (2010) to test if simulations could recreate some collocated radar and passive microwave data when applying different particle shapes. In a similar study by Geer and Baordo (2014) only passive data were considered but a more wide set of frequencies and atmospheric conditions were investigated. They found that a sector-like snowflake model gave the smallest overall error for the simulations performed. This choice will replace a SPA treatment as the default for the snow hydrometeor category in the RTTOV-SCATT (Bauer et al., 2006) package (Geer and Baordo, 2014). In Sect. 6 an alternative version of the approach of Geer and Baordo (2014) is tested, that does not involve any assumption on PSD or actual ice masses.

DDA calculations have also been used in a more direct manner to investigate shape aspects. For example, Kim (2006) compared DDA and solid sphere results and claimed that particle shape is less critical for size parameters below 2.5 (see Eq. 2 for the definition), but only a few DDA shapes and frequencies were considered, radar back-scattering was ignored, and no quantitative error estimate was given. Comparisons between DDA and corresponding SPA data are found in e.g. Liu (2008); Nowell et al. (2013) and Liao et al. (2013), but the results have throughout a limited scope and we have found no comprehensive analysis of the limitations of SPA. An important result was obtained by Liu (2004), showing that an optimal "softness parameter", to be ap-

plied in a SPA framework, varies with frequency. The same conclusion has also been reached in indirect ways by others, as pointed out by Geer and Baordo (2014).

From the perspective of mass retrievals it is most practical to characterise the size of the particles through their equivalent mass ice sphere diameter, d_e:

$$d_\mathrm{e} = \sqrt[3]{\frac{6m}{\rho_i \pi}}, \tag{1}$$

where m is the particle mass and ρ_i is the density of (solid) ice. We define the size parameter, x, correspondingly:

$$x = \frac{\pi d_\mathrm{e}}{\lambda}, \tag{2}$$

where λ is the wavelength at which the measurement is performed.

In microwave sounding, the mass is inferred from estimated extinction or back-scattering coefficients. Any type of such coefficient, γ, can be expressed as

$$\gamma = \int_0^\infty N(d_\mathrm{e})\overline{\sigma_\gamma}(d_\mathrm{e})\,\mathrm{d}d_\mathrm{e}, \tag{3}$$

where $N(d_\mathrm{e})$ is the particle size distribution (PSD) and $\overline{\sigma_\gamma}(d_\mathrm{e})$ is the local average cross-section for particles having a mass matching d_e. In its turn, Eq. (3) implies that trying to estimate $\overline{\sigma_\gamma}(d_\mathrm{e})$ from observed satellite data (as done in e.g. by Kulie et al., 2010; Geer and Baordo, 2014) requires a good knowledge of both the mass of frozen hydrometeors and the PSD.

Another common way to express particle size is by the maximum diameter, d_m. We start the study by using d_e, because usage of d_m demands that the relation between d_m and particle mass must be introduced. Such relationships depend on particle shape, and for the basic purpose of this study that is a problematic complication. By using d_e,

Discussion Paper | Discussion Paper | Discussion Paper | Discussion Paper |

particle shape only influences $\overline{\sigma_\gamma}(d_e)$. However, as d_m is probably more frequently used than d_e, this alternative to characterise particle sizes is considered as last step of the study (Sect. 7).

In summary, our scope is the approximation of particle shape in microwave retrievals of the mass of pure ice hydrometeors. Focus is put on SPA and the basic conclusion of Geer and Baordo (2014). Both passive and active measurements are considered as merging information from different sensor types is already a fact (e.g. Rydberg et al., 2009; Kulie et al., 2010), and such synergies should in the future just grow in importance. The practical aim can be seen as finding a shape model that gives a good estimate of $\overline{\sigma_\gamma}(d_e)$, for relevant optical properties, over a large range of particle sizes, frequencies, measurement techniques and possible habit mixes. Existing DDA data are reviewed and used as reference. Only complete random orientation is treated because most established publicly available DDA databases are currently limited to this assumption on orientation.

Further, compared to earlier similar works, much higher attention is given to frequencies above 200 GHz. Ice mass retrievals are already performed at sub-millimetre wavelengths using limb sounding (Wu et al., 2008; Rydberg et al., 2009; Millán et al., 2013) and airborne sensors (Evans et al., 2012). Additionally, a strong motivation for this assessment are upcoming sub-millimetre instruments: the European ISMAR (International SubMillimetre Airborne Radiometer) airborne instrument and the ICI (Ice Cloud Imager) sensor to be part of the next series of Metop satellites. ICI is a down-looking sub-millimetre cloud ice sensor, a concept that has already been described in several articles (Evans and Stephens, 1995a; Buehler et al., 2007, 2012), but for which so far no actual satellite sensor has been available. This study is part of our overall effort to build the scientific foundation for the analysis of first the ISMAR airborne and then eventually the ICI satellite data.

2 Refractive index

Any calculation of single scattering properties, i.e. independently if Mie, T-matrix or DDA calculations are performed, requires that the refractive index is specified. Parameterisations and expressions related to the refractive index of ice at microwave frequencies are reviewed in this section. Both the real (n') and imaginary (n'') part of the complex refractive index n are relevant. Some relationships are more easily expressed in terms of the (relative, complex) dielectric constant, ϵ. Neglecting magnetic effects, which is a good assumption here, this quantity is related to the (complex) refractive index as:

$$n = \sqrt{\epsilon} \tag{4}$$

2.1 Pure ice models

Providing complex refractive index practically over the complete electromagnetic spectrum in the form of data tables, Warren (1984), in the following referred to as W84, has been a long-term standard in atmospheric science for the refractive index of pure water ice. Hufford (1991, H91) developed a parameterisation for microwave frequencies up to 1 THz based on Debye and Lorenz theories with parameters fitted from measured data. The parameterisation was incorporated in the MPM93 atmospheric propagation model by Liebe et al. (1993). Compared to W84, H91 generally predicts lower n'' for frequencies < 350 GHz (see Fig. 1, right panel). Consistent with measurements it predicts a stronger increase of n'' with temperature than W84 at sub-millimetre frequencies.

In the advent of sub-millimetre observation techniques, Jiang and Wu (2004, J04) added a higher order frequency term, as suggested by Mishima et al. (1983), to H91 in order to cover frequencies up to 3 THz. Resulting n'' agree well with H91 till about 1 THz as shown in Fig. 1. Beyond 1 THz, where H91 claims no validity, J04's n'' exhibits the frequency and temperature dependence pattern expected from measured far-infrared behaviour of n''. Zhang et al. (2001, Z01) did the first measurements of both n' and n'' at sub-millimetre frequencies and atmospheric temperatures. For n'' they found a linear temperature dependence of about 1 % K^{-1}. The measurements agree quite well with the H91 and J04 models. However, the Z01 model falls short of reproducing their own measurements – it predicts very low values over all frequencies (see Fig. 1) and all temperatures.

Mätzler et al. (2006, M06) introduced a permittivity parameterisation that consolidates most earlier models and measurements. Regarding imaginary part, it agrees well with the J04 model, particularly at microwave frequencies, deviating at maximum by 5 % at higher frequencies and high temperatures. The largely revised and updated version of W84, the Warren and Brandt (2008, W08) data, incorporates the M06 model at $T = -7\,^{\circ}\mathrm{C}$ and proposes M06 as the model of choice at wavelengths beyond 200 µm when temperature dependence should be considered.

J04 found their model to be within 12 % of the imaginary permittivity measurements for frequencies below 800 GHz, and within 15–40 % above 800 GHz. M06 estimated the uncertainty of their model from the SDs of measurements to 5 % at 270 K and 14 % at 200 K. W08 state the uncertainty of their n'' data to be 10 % ($T = -7\,^{\circ}\mathrm{C}$). Compared to recent models, the once quasi-standard model W84 strongly overestimates n'' at millimetre wavelengths (up to a factor of 5), underestimates it at sub-millimetre wavelengths (up to a factor of 2) and overestimates it in the far-infrared (up to a factor of 2).

In contrast to n'', n' is generally considered to be known with higher accuracy and to vary little to negligibly with both temperature and frequency. The measurements by Z01 confirm the small frequency dependence (0.3 % over 250–1000 GHz) and do not show significant temperature dependence. The different models mentioned above provide slightly different relations of n' with frequency and temperature. However, we find refractivity ($n' - 1$) from all models to agree with M06 within 1.3 %, according to the left panel of Fig. 1. Based on estimates on propagation of n' uncertainty to optical properties, we conclude that the uncertainty in n' is not a limiting factor and choice of model is not critical.

In summary, M06 seems the best choice for microwave to far-infrared imaginary refractive index data. In view of the effects that errors in imaginary refractive index

have on cloud optical properties, we strongly suggest to no longer use the Warren (1984) data in future.

2.2 Mixing rules

The parameterisations reviewed above deal with solid ice, while in the soft particle approximation (Sect. 5) the particles are treated to consist of a homogeneous mixture of ice and air. The standard procedure to assign a refractive index to the mixture is by applying a so called mixing rule. In this paper we compare some commonly used mixing rules from a purely practical perspective, a more theoretical review of mixing rules is provided by Sihvola (2000).

Throughout, we will assume the refractive index of air to be $1 + i0$, in other words we assume that the optical properties of air are like those of vacuum. Of course, for the radiative transfer problem as a whole both absorption and refraction by air matter strongly. But given the much larger refractive index of ice we neglect this in the calculation of the single scattering properties, as commonly done also by other authors.

Three mixing rules are considered: “Maxwell–Garnett” (Garnett, 1906), “Bruggeman” (Bruggeman, 1935) and “Debye” (Debye, 1929). All these formulas operate with dielectric constants. The Debye mixing rule is

$$\frac{\epsilon_e - 1}{\epsilon_e + 2} = \frac{f_1^v(\epsilon_1 - 1)}{\epsilon_1 + 2} + \frac{(1 - f_1^v)(\epsilon_2 - 1)}{\epsilon_2 + 2}, \tag{5}$$

where ϵ_e is the “effective” dielectric constant of the mixture, f_1^v is the volume fraction of medium 1 ($f_1^v + f_2^v = 1$), and ϵ_1 and ϵ_2 are ϵ for medium 1 and 2, respectively. The expression for Bruggeman is

$$\frac{f_1^v(\epsilon_1 - \epsilon_e)}{\epsilon_1 + 2\epsilon_e} + \frac{(1 - f_1^v)(\epsilon_2 - \epsilon_e)}{\epsilon_2 + 2\epsilon_e} = 0. \tag{6}$$

The Debye and Bruggeman expressions are symmetric with respect to the two media. Maxwell–Garnett differs in this respect as this rule makes a distinction between the "matrix" ($\epsilon = \epsilon_\mathrm{m}$) and the "inclusion" ($\epsilon = \epsilon_i$):

$$\epsilon_\mathrm{e} = \epsilon_\mathrm{m} + 3 f_i^\mathrm{v} \epsilon_\mathrm{m} \frac{(\epsilon_i - \epsilon_\mathrm{m})}{\epsilon_i + 2\epsilon_\mathrm{m} - f_i^\mathrm{v}(\epsilon_i - \epsilon_\mathrm{m})}, \tag{7}$$

where is f_i^v is the volume fraction of the inclusion medium ($f_m^\mathrm{v} + f_i^\mathrm{v} = 1$). That is, for Maxwell–Garnett we have two cases "air in ice" and "ice in air", below shortened to $\mathrm{MG_{ai}}$ and $\mathrm{MG_{ia}}$, respectively, that result in different ϵ_e depending on if air is set to be the matrix or inclusion medium.

For completeness, the effective density (ρ_e) matching f_1^v is

$$\rho_\mathrm{e} = f_1^\mathrm{v} \rho_1 + (1 - f_1^\mathrm{v}) \rho_2, \tag{8}$$

where ρ_1 and ρ_2 are the density of medium 1 and 2, respectively. In terms of mass fraction of medium 1 (f_1^m), ρ_e is

$$\rho_\mathrm{e} = \frac{\rho_1 \rho_2}{f_1^\mathrm{m} \rho_2 + (1 - f_1^\mathrm{m}) \rho_1}. \tag{9}$$

An example comparison between the mixing rules is shown in Fig. 2. A first observation is that the Debye and the "ice in air" version of Maxwell–Garnett ($\mathrm{MG_{ia}}$) give identical results (for $\epsilon_\mathrm{m} = \epsilon_\mathrm{air} = 1 + i0$ the two formulas are mathematically identical). Hence, the Debye rule is not explicitly discussed below, but is represented by the identical $\mathrm{MG_{ia}}$. $\mathrm{MG_{ia}}$ gives consistently the lowest refractive index, for both real and imaginary part. The difference to the other two rules is the highest at air fractions around 0.45. The highest values are throughout found for $\mathrm{MG_{ai}}$, and Bruggeman falls between the two Maxwell–Garnett versions. Repeating the calculations for other frequencies and temperatures (e.g. Johnson et al., 2012, Fig. 2), i.e. other ice refractive indices, shows that these patterns are of general validity, and are not specific to our example.

The deviations between the mixing rules are significant. For example, Johnson et al. (2012) conducted a sensitivity analysis for frequencies between 2.8 and 150 GHz regarding the choice of mixing rule. The differences when using $\mathrm{MG_{ai}}$ or $\mathrm{MG_{ia}}$ were found to be ~ 2 dB for radar reflectivity and reach at least 10 K for brightness temperature.

Some mixing rule can be optimal for representing a true homogeneous ice-air spherical particle, as studied by Petty and Huang (2010), but this is not the crucial point in this context. In Sect. 5.1 we instead pragmatically test if any of the mixing rules leads to a simpler approximation of realistically shaped particles.

3 Existing DDA databases

The Discrete Dipole Approximation (DDA) is the most widely used method for computing the scattering properties of arbitrarily shaped particles. In the DDA method, a particle is represented by an array of dipoles in a cubic lattice with a given inter-dipole spacing. This spacing must be adequately small relative to the incident wavelength in order to obtain desired accuracy, which requires large computer memory and long calculation time for large particles.

Despite the wide usage of the method, the publicly available DDA data for microwave scattering of ice particles are limited. The three databases that are used in this study are the ones of Liu (2008); Hong et al. (2009) and Nowell et al. (2013). The main properties of these databases are summarised in Table 1.

The only other open source of microwave DDA data that we know about is www.helsinki.fi/~jktyynel/database.html, where data used in Tyynelä and Chandrasekar (2014) and some other publications were recently made available. These data, covering frequencies up to 220 GHz, are not included in this paper as they deal with partly oriented particles, while the other databases all are valid for completely random orientation.

3.1 Liu

Liu (2008) applied the DDA code of Draine and Flatau (2000), denoted as DDSCAT, and computed single scattering properties (i.e. scattering cross section, absorption cross section, back-scattering cross section, asymmetry parameter, and phase function) of

Discussion Paper | Discussion Paper | Discussion Paper | Discussion Paper |

eleven types of ice particle crystal shapes, at 22 frequencies (3, 5, 9, 10, 13.4, 15, 19, 24.1, 35.6, 50, 60, 70, 80, 85.5, 90, 94, 118, 150, 166, 183, 220 and 340 GHz) and for five different temperatures. To not clutter the figures below, we include only six of the eleven particle types. The ignored shapes are: short column, block column, thin plate and 4 and 5-bullet rosettes; included shapes are pointed out in the figure legends.

The particles were treated to have random orientation. The phase function is provided for 37 equally spaced scattering angles between 0 and 180°. In terms of the "phase matrix" required for vector radiative transfer, only the (1,1) element is given. The refractive index of ice applied in the DDA calculation was taken from Mätzler et al. (2006).

3.2 Nowell

A new snowflake aggregation model is introduced in Nowell et al. (2013). The 6-bullet rosette is a frequently observed crystal shape and therefore was selected by Nowell et al. (2013) as constituent crystals of the simulated snowflake aggregates. The aggregates were allowed to grow in three dimensions, following an algorithm resulting in quasi-spherical snowflakes following the diameter-density parameterisation of Brandes et al. (2007). The representation of the bullet rosettes is somewhat coarse, based on cubic blocks with size of ≈ 50 µm. Only particles with a maximum diameter above 1 mm are included in our figures to make sure that the aggregates consist of a relatively high number of building blocks.

The single scattering properties of an ensemble of randomly generated aggregates were calculated by the DDSCAT code. Calculations for ten frequencies (10.65, 13.6, 18.7, 23.8, 35.6, 36.5, 89, 94, 165.5, and 183.31 GHz) and a single temperature (263 K) were performed, with refractive index taken from Mätzler et al. (2006). The phase function is not included in this database, only the corresponding asymmetry parameter is stored.

3.3 Hong

Also Hong et al. (2009) used DDSCAT, to compute the scattering properties (extinction efficiency, absorption efficiency, single scattering albedo, asymmetry parameter, and scattering phase matrix) of six randomly oriented non-spherical ice particles at 21 frequencies (90, 118, 157, 166, 183.3, 190, 203, 220, 243, 325, 340, 380, 425, 448, 463, 487, 500, 640, 664, 683, and 874 GHz) for a temperature of 243 K. All six independent elements of the phase matrix are reported, in steps of 1° between 0° and 180°.

The geometrical information of the six ice particle shapes is detailed in Table 1 of Hong (2007). To obtain the properties of randomly oriented particles, β, θ, and φ are varied in ranges of $0-2\pi$, $0-\pi$, and $0-2\pi$, and scattering quantities are averaged over different combinations of orientations. Refractive index of ice was taken from Warren (1984), that according to Sect. 2.1 is not the optimal choice with respect to particle absorption.

3.4 Comparison of the databases

Example DDA data are found in Fig. 3, for one of the few frequencies that is found in all three databases (183 GHz). All three aggregate types in the Nowell database are plotted with the same symbol. The abscissa of the figure is size parameter according to Eq. (2), implying that the radiative properties are compared between particles having the same mass. Absorption, scattering and back-scattering are reported as the corresponding efficiency, Q, calculated with respect to d_e as

$$Q = \frac{4\sigma}{\pi d_e^2}, \tag{10}$$

where σ is the cross-section of concern. Even though usage of Q provides some normalisation of the data, compared to if cross-sections would be plotted, the ordinates in the first three panels of Fig. 3 still span several orders of magnitude. In Fig. 4 another normalisation is applied, that brings out differences at lower size parameters:

Discussion Paper | Discussion Paper | Discussion Paper | Discussion Paper |

The optical cross-sections are divided by the corresponding optical cross-section of the equivalent mass solid ice sphere with same ice refractive index.

Although we discuss the soft particle approximation in depth only in Sect. 5, solid and soft spheroids are already included in the figures here for reference. We also already make some remarks on their optical properties here, but postpone the explanation of how the soft-spheroid results were generated to the dedicated section later.

The Hong data have systematically a higher absorption than Liu. This can be discerned in Fig. 3 and is expected due to the higher imaginary part of the refractive index (n'') in W84 (used by Hong) compared to M06 (used by Liu) for frequencies below 400 GHz, as shown in Fig. 1. This deviation is removed in Fig. 4 as the normalisation is done with respect to Mie calculations with the refractive index set to match the DDA data. Without this adjustment of the refractive index, there would be a much higher variability in the absorption ratios in Fig. 4, with the different DDA databases at different mean levels. Droxtal particles are quasi-spherical and the fact that these particles obtain ratios very close to one in Fig. 4 confirms that a correct normalisation has been applied. This similarity in shape explains also why the droxtals end up close to the data for solid spheres for all quantities in Fig. 3.

It is well known that the impact of shape on the extinction efficiency increases with particle size. Accordingly, for x below ~ 0.5 there is a comparably low spread between different particles, for both absorption and scattering. In terms of the ratio in Fig. 4, the data are mainly inside 1.2 ± 0.2. On the other hand, at $x = 2$ the difference between the lowest and highest scattering, for particles having the same mass, is about a factor of five (Fig. 3). These remarks consider also 340 GHz (not shown) where the same particles result in higher size parameters.

The back-scattering efficiency shows a similar pattern as the scattering one, but the variation above $x = 2$ is considerably higher, about a factor of ten. This is the case as the back-scattering depends on the phase function for a particular direction, resulting in a higher sensitivity to the exact shape of that function, while the overall scattering extinction corresponds to the integrated phase function.

There is a significant spread in the asymmetry parameter (g) from about $x = 0.5$ and above. Above $x \approx 1.5$, the difference between highest and lowest g is about 0.3, where the Nowell aggregates and the Liu bullet rosettes throughout cause the highest and lowest values, respectively. The 6-bullet rosettes in the Hong database show the same tendency of low g for combinations of size and frequency resulting in $x > 1.5$. On the other hand, at lower x the Hong rosettes tend to give the highest g among all of the particles, then also higher than the corresponding Liu rosette. That is, the different 6-bullet rosette models used by Liu and Hong result in significantly different optical properties.

Figure 3 was inspired by Fig. 7 of Nowell et al. (2013), comparing that database with solid and soft particle calculations in the same way. Nowell et al. (2013) used a higher air fraction for their soft particles and it is not clear if the MG_{ai} or MG_{ia} version of the Maxwell–Garnett mixing rule was used, but there are still some clear deviations between the two figures for soft particles. For example, the scattering efficiency of soft particles in our Fig. 3 is quite close to the data from Nowell et al. (2013), while in their Fig. 7 the soft particles give significantly lower scattering. In addition, we obtain basically identical scattering efficiencies for soft spheres and spheroids, while Nowell et al. (2013) got lower scattering for spheroids. We have carefully checked our calculations and our results seem to fit better with what has been found elsewhere. For example, in Fig. 5 of Liao et al. (2013) a good agreement with the aggregates of Nowell et al. (2013) is obtained by soft particles having a density of $0.2\,\mathrm{g\,m^{-3}}$ (the air fraction of 0.75 in Fig. 3 matches $0.23\,\mathrm{g\,m^{-3}}$), and basically identical results are obtained between spheres and both prolate and oblate spheroids.

4 Relevance of absorption and asymmetry parameter

To judge the performance of a soft particle approximation or some "shape model", a basic consideration is in what detail the single scattering properties must be compared? The main issue is that the phase function (describing the angular redistribution of scat-

Discussion Paper | Discussion Paper | Discussion Paper | Discussion Paper |

tered radiation, also denoted as the scattering function) can be very complex and is basically unique for all particles where not Rayleigh conditions apply. However, it is normally not required to compare the phase function in full detail. For example, it is in general only the direct back-scattering that is of interest for radar applications. This is valid until multiple scattering becomes significant, when also the phase function starts to be relevant.

For passive measurements, the standard choice is to give an overall description of the phase function by using the parameter g. The asymmetry parameter is known to have a strong influence in radiative transfer of solar radiation (e.g. Kahnert et al., 2008). The quantity is also frequently reported in connection to passive microwave radiative transfer (e.g. Liu, 2004; Kim, 2006), but, to our best knowledge, the actual influence of g for such applications has not been investigated in a general manner. A simple test of this type is found in Fig. 5. Satellite measurements at 150 GHz and an incidence angle of 45° were simulated. Temperature and gas profiles were taken from a standard tropical scenario (Fascod), and a 2 km thick "cloud" layer, centred at 10 km, was added. A single particle size (monodispersive PSD) was used for each simulation, and the number of particles was adjusted to obtain the specified zenith optical depths. Spherical particles with an air fraction of 0.4 were assumed, and d_e was varied to obtain a range of g.

The solid lines in Fig. 5 show how the radiance changes with g when the cloud optical depth is kept constant and all particle absorption is suppressed. The basic pattern is that the cloud impact on measured radiance decreases with increasing g. This makes sense as high g means that the up-welling emission from the lower troposphere is less redirected, compared to the case of more isotropic scattering at low g. See Buehler et al. (2007) for a schematic figure and discussion of the radiative transfer for this measurement geometry. It is hard to see in the figure, but there actually are some "wiggles" around $g = 0.65$, showing that the relationship to g is not completely monotonic. That is, several values of g can result in the same radiance.

In Fig. 5 the cloud impact for $g = 0$ and $g = 0.6$ differs by a factor of about 2. That is, changing g with 0.1 results in a $\sim 10\,\%$ change in cloud impact. For low optical thickness the relationship between scattering cross-section (σ_s) and radiance impact is close to linear. Accordingly, a 10 % error in σ_s and a 0.1 error in g are in rough terms equally important. The test displayed in Fig. 5 was repeated for other frequencies and cloud altitudes. The absolute values of the cloud impact change, primarily following the magnitude of the gas absorption at the altitudes around the cloud layer, but the mentioned relation between σ_s and g was found to be relatively constant.

There is also some uncertainty regarding the importance of ice particle absorption for passive measurements. It is well known that absorption is most significant for smaller particles, i.e. the single scattering albedo increases with particle size (e.g. Evans and Stephens, 1995b; Eriksson et al., 2011b). Figure 5 confirms this as the difference between considering absorption (dashed lines) and neglecting it (solid lines) is high for small x, for all cloud optical depths. This aspect is especially important for limb sounding, as in this observation geometry focus is put on higher altitudes where smaller particles are more frequent, and it has been shown that the measured signal can even be dominated by absorption (Wu et al., 2014).

Figure 5 shows also the less obvious fact that absorption increases in importance with increasing cloud optical thickness. For an optical thickness of 2.0 absorption is significant up to at least $x = 1.2$, while for small optical depths (such as 0.1) the absorption can be neglected for x above ~ 0.5. This is a consequence of that the probability of absorption increases when multiple scattering becomes more prominent. The changed conditions caused by multiple scattering implies that the relevance of absorption can not be judged alone from the single scattering albedo parameter. In addition, the observation geometry matters for the relative importance of absorption and scattering, as discussed in Eriksson et al. (2011b).

In summary, it is confirmed that the quantities normally considered (σ_a, σ_s, σ_b, and g) are all relevant, but to a varying degree. Most importantly, the relevance of absorption decreases with size parameter.

Discussion Paper | Discussion Paper | Discussion Paper | Discussion Paper |

5 Approximation by soft particles

The soft particle approach (SPA) is based on two main simplifications. Firstly, the particle is treated to consist of a homogeneous mix of air and ice, and also water if mixed-phase particles are considered (e.g. Galligani et al., 2013). The air fraction of the mix is either set to a constant value, or is obtained by assuming an effective density of the particle, likely varying with particle maximum size. A single refractive index is assigned to the mix by applying a mixing rule (Sect. 2.2). Secondly, the particles must be set to have some specific shape, to allow that the single scattering properties can be determined with a limited calculation burden. As mentioned, the T-matrix method allows that e.g. soft columns and plates are possible options, but the standard choices are to model the particles as spheres or spheroids. A much more careful description of SPA is provided by Liao et al. (2013).

5.1 Selection of mixing rule

As a first step, we examined if the choice of mixing rule is critical in any way for SPA. The difference between mixing rules can in general be compensated by selecting different air fractions, but exceptions exist. This is most clearly seen for the absorption and scattering cross-section at smaller x, as exemplified in Fig. 4. In the figure, the absorption of soft particles when using Maxwell Garnet with "ice in air" (MG_{ia}) is throughout lower than the DDA results. This in contrast to when using the Bruggeman or the "air in ice" version of Maxwell Garnett mixing rule (MG_{ai}), where the soft particle absorption matches some of the DDA data points. The same pattern is found also for the scattering cross-section, but for a smaller range of x.

The low bias in Fig. 4 of MG_{ia}, compared to DDA data, can not be removed by modifying the air fraction, as shown in Fig. 6. In this figure, the ratios of Fig. 4 are calculated for air fractions between 0 and 0.95 and the ratios obtained when using MG_{ia} are throughout below 1. Ratios around at least 1.2 are required to represent the average values of the DDA data in Fig. 4. For $x < 0.5$ such ratios, and even much

higher values, can be obtained by selecting the MG_{ai} mixing rule. Ratios when using Bruggeman (not shown) reach 1.25 for absorption and 1.15 for scattering, which is on the limit to fit the DDA data. For MG_{ai} the ratios switch from being > 1 to < 1 around $x = 1$, that below is shown to be the general behaviour of DDA data.

The conclusion of Figs. 4 and 6 is that using the MG_{ia} mixing rule leads to a systematic underestimation of the absorption and scattering at some size parameter ranges. The same applies to the Debye mixing rule as it is identical to MG_{ia}. The Bruggeman rule gives higher values, but is not capable of reproducing the highest DDA-based ratios found in Fig. 4. These remarks do not depend on if soft spheres or spheroids are used. Accordingly, MG_{ai} appears as the best choice in this context, and only this mixing rule is considered below.

5.2 Selection of particle shape

Solid spheres are known to exhibit resonance features for x above ~ 1, which are reflected as oscillations in the properties displayed in Fig. 3 (blue solid lines). An individual spheroid would give similar oscillations, but the assumption of completely random orientation partly averages out those patterns for the spheroids (see Fig. 3, red solid lines). The resonance phenomena are dampened when going to soft particles. This results in a marginal difference in extinction (absorption and scattering cross-sections) and g between soft spheres and spheroids (dashed lines). However, there is a significant difference for the back-scattering, where soft spheres give even stronger oscillations than solid spheres. The soft spheroids show a more smooth variation with x, and should allow a better fit to the DDA data. Liao et al. (2013) made the same observations for soft particles, and showed that extinction and g are basically unaffected by the aspect ratio of the spheroids, or if they are oblate or prolate. They found also that the oscillations in size dependence of the back-scattering decrease when the aspect ratio moves away from one.

That is, soft spheroids are to prefer over soft spheres, primarily due to the difference with respect to back-scattering. For complete random orientation the selection of aspect ratio is not critical, and only oblate spheroids with an axial ratio of 0.6 are considered below, following Hogan et al. (2012). In terms of the nomenclature used in the T-matrix code, this equals an aspect ratio of 1.67.

5.3 Selection of air fraction

As shown in the above figures, for a given size parameter there is a spread of the particle optical properties over the different habits. Hence, it is not possible to match all particle shapes on the same time with a soft particle approximation. The ambition is instead to approximately mimic the average properties. Figure 3 shows that solid spheres and spheroids do not meet this criterion as they e.g. for $x > 4$ systematically underestimate scattering cross-section and g.

5.3.1 Relevance of the reference data

A more detailed analysis requires some consideration of the occurrence frequency of the different particles in the DDA databases. For example, the Hong database contains droxtals having a maximum diameter, d_m, up to 2 mm, while the general view is that this shape is only representative for smallest ice crystals (Baran, 2012). In fact, Schmitt and Heymsfield (2014) found that cloud ice particles with a d_m above 250 µm are mainly of aggregate type, implying that also single plates and columns having dimensions above this size are relatively rare. The aggregate types discussed by Schmitt and Heymsfield (2014) appear to be relatively similar to the aggregates in the Hong database.

For the representation of particles of snow type, the Liu database offers two shapes (dendrite and sector-like snowflakes) both having high aspect ratios, while the aggregates of the Nowell database (claimed to represent snowflakes) have an aspect ratio close to 1. This difference in aspect ratio results particularly in deviations in the scattering cross-section and g of those particles (Fig. 3). If "snow" is understood as everything from the classical single-crystal snowflake to graupel, both these assumptions on aspect ratio are realistic, but it is clear that particles having intermediate aspect ratios

also exist and, hence, they are not yet covered by the DDA databases. The Hong aggregates could potentially also work as proxy for snow particles, but data for d_m above 2 mm are lacking.

5.3.2 Fit of single scattering data

Figure 3 exemplifies a fit of the available DDA data using soft particles having an air fraction (AF) of 0.75. For the frequency of concern (183 GHz) the soft particles, compared to the solid ones, give indeed a better general fit of absorption and scattering efficiencies. For g at $x > 1.5$, the soft particles agree well with the Nowell aggregates, while all other particle shapes are better approximated with solid spheres or a comparably low AF. That is, for e.g. the Liu sector-like snowflake, the AF that gives the best fit with scattering efficiency is not the same AF that is needed to match g.

Example results for other frequencies are found in Fig. 7. This figure, together with Fig. 4 covering 183 GHz, indicate that the MG_{ai} mixing rule combined with an AF of 0.25 give an acceptable fit of absorption and scattering for size parameters below 0.5, independently of frequency. At higher x, AF = 0.25 is not optimal, it gives a fairly good fit at 874 GHz (Fig. 7), but at e.g. 90 GHz this AF results in too high values for both absorption and scattering. For $x > 1$ and lower frequencies, a fit of absorption and scattering efficiencies requires higher AFs. For example, mimicking the scattering efficiency at 90 GHz requires an AF on the order of 0.75–0.9, depending on if all or just snow-type particles should be fitted.

These remarks show three facts. Firstly, there is in general not a single AF that simultaneously gives a fit of all four optical property parameters. Secondly, at least when operating at lower frequencies, the AF to apply in a soft particle approximation must be allowed to vary with particle size. Thirdly, the best AF has a frequency dependence (at least for larger x). The third point is well-known, it has been shown by e.g. Liu (2004).

The soft particle AF is frequently set to follow some density parameterisation. This gives the AF a variation with size in line with the second point. However, already the known fact that an optimal AF varies with frequency (point 3) signifies that using true densities can not work as a general approach with respect to optical properties. This is the case as density-based AFs are independent of frequency. In addition, for larger particles standard density parameterisations result in much higher AFs than the ones giving a match of single scattering data around 100 GHz and above. As an example, the particle model of Hogan et al. (2012) is included in Fig. 7. This particle model is based on the frequently used density parameterisation of Brown and Francis (1995), that leads to AFs close to 1 for the largest DDA particles. In fact, the scattering efficiency at 90 GHz becomes too low already at $x \approx 0.5$. Also, back-scattering is underestimated at x above ≈ 0.5, even at lower frequencies (Fig. 8). All other density parameterisations we have tested show the same general feature, to produce, in this context, too high AFs for larger particles. For more recent parameterisations the density goes below 100 kg m^{-3} at $d_m \approx 800$ µm (Cotton et al., 2013, Fig. 6).

Hogan et al. (2012) was selected as it provides a clearly defined particle model. However, it should be noted that Hogan et al. (2012) treat the spheroids to be aligned with the maximum dimension in the horizontal plane, while we apply completely random orientation.

5.3.3 Test radiative transfer simulations

Absorption, scattering and asymmetry parameter interact for simulations of passive observations, as shown in Sect. 4. Some test simulations were performed in order to check if the different tendencies for these quantities combine in a positive or negative manner. These simulations, shown in Fig. 9, were performed for the same scenario as used for Fig. 5. Again, a monodispersive PSD was used, but here the number of particles was adjusted to obtain a specified vertical column of ice mass, or ice water path (IWP). The IWP for each frequency was selected to give a maximum cloud induced brightness temperature change of 5–10 K, in order to get a significant response but still avoiding a high degree of multiple scattering.

The calculations were done with the DOIT module of the ARTS radiative transfer model (Emde et al., 2004; Eriksson et al., 2011a), that requires the full phase function

and no results for the Nowell database could be generated. For Fig. 9 a more strict selection of the DDA particles was done, roughly matching the discussion in Sect. 5.3.1 in order to just keep the most realistic particles. Column, plates and 3-bullet rosettes having d_m above 1 mm were excluded. For droxtals the limit was set to 200 µm. The black solid lines show a polynomial fit (in linear scale) of the simulations based on the remaining DDA particles.

As expected from the discussion above, the different DDA particles give little spread of simulated brightness temperatures for $x < 0.5$. On the other hand, there is a strong variation at larger size parameters. For example, the Liu dendrite snowflakes, and around $x = 1$ also the Hong 6-bullet rosettes, have particularly low influences. This is a combined effect of relatively low scattering efficiency and high g (Fig. 4). The same combination enhances also the differences between the Liu sector-like and dendrite snowflakes, compared to the differences for scattering efficiency alone. The relative influence between the particles is not the same for all frequencies. For example, the Hong aggregates are found on the high side for 90 and 166 GHz, but are rather on the low side for 874 GHz.

Figure 9 shows that the selection of the soft particle AF is not highly critical for size parameters below 0.5. This is partly due to compensating errors. A too high AF gives an overestimation of both absorption and scattering, but this is counteracted by an overestimation of g. At higher size parameters, the frequency dependence of the "optimal" AF noted above is seen also here. For example, at 340 GHz, an AF of 0.25–0.50 is required to match the fit of the DDA results (black line), while for 90 GHz a suitable AF is above 0.75. For 874 GHz, only covered by the Hong database, an AF around 0.25 gives best agreement. The systematic deviation between the soft particle and the DDA-based results seen for 874 GHz and low x is due to the refractive index differences discussed in Sect. 2.1.

6 Approximation by a single representative shape

Based on poor experience of using the SPA at ECMWF (the European Centre for Medium-Range Weather Forecasts), Geer and Baordo (2014) attacked the representation of particle shape in microwave radiative transfer from another angle. Their application is data assimilation for numerical weather prediction, but the basic problem is the same as for direct retrieval of frozen hydrometeors. Their approach is simple, to try to find a particle type, for which DDA calculations are at hand, that minimises the average deviation to actual observations. They compared to measurements from the TMI and SSMIS sensors, for frequencies between 10 and 190 GHz. The Hong database does not cover the lower end of this frequency range, and only the Liu database was considered.

They performed global simulations, for latitudes between 60° S and 60° N. Simulated brightness temperatures were obtained with RTTOV-SCATT, a radiative transfer tool making use of several approximations. The atmospheric data were taken from the ECMWF 4D-var assimilation system, likely having biases in ice mass amounts varying between regions, land/ocean and the different hydrometeor types. Further, a PSD must be assumed for the simulations. The tropical version of the PSD of Field et al. (2007) was found to give the best overall fit with observations, among the three PSDs considered. These aspects introduce problems for a clear identification of the best overall proxy particle shape, as discussed in detail by Geer and Baordo (2014).

The final recommendation of Geer and Baordo (2014) is to apply the Liu sector-like snowflake, for all classes of both cloud ice and snow. A somewhat better fit could be obtained by some combinations involving the 6-bullet rosettes and dendrite snowflake particles, but the improvement was not sufficiently large to motivate a more complicated particle shape model. Our results corroborate the selection of the sector-like snowflake as the general proxy shape particle. First of all, this particle type does not stand out in any obvious way, it shows in general intermediate values. In fact, the best match with the polynomial fit of the DDA-based simulations in Fig. 9 (black lines) is given by the

sector-like snowflakes for both 90 and 166 GHz. A good fit is also obtained by the Liu 6-bullet rosette, another particle type that Geer and Baordo (2014) had as a strong candidate. The sector-like snowflake tends to be on the high end for x around 0.7, but on the low side at higher x. If these happen to be true biases, they are partly averaged out in PSD-weighted bulk properties.

The Liu sector-like snowflakes exhibit average properties also at 340 GHz, above the frequency range considered by Geer and Baordo (2014). The pattern is very similar to the lower two frequencies, with some tendency to "overshooting" around $x = 1$. If the upper limit for plates and columns would have been set to a lower value, such as 500 µm, the sector-like snowflakes would even have shown outlier behaviour around $x = 1$. This results in that for 340 GHz an even better agreement with the polynomial fit is obtained with the Hong aggregates. This particle type is throughout below the fitting line at 874 GHz, but this result depends heavily on a strong influence on the polynomial fit of columns and plates with $d_e \approx 500$ µm. The Hong bullet rosette seems not to be a candidate for the role as general proxy shape because it has a very low scattering efficiency around $x \approx 1.5$, which is also reflected in Fig. 9.

Figures 2 and 3 of Geer and Baordo (2014) complement the figures of this paper by reporting bulk optical properties of the Liu particles as function of ice mass and frequency. A bit surprising is that the sector-like snowflake is found to have the lowest bulk g, seemingly for all frequencies and ice masses. This shape has also the lowest g among the Liu particles in Fig. 3, but only up to $x = 1$. On the other hand, the SPA spheres applied are found to give very high bulk g. Geer and Baordo (2014) explain this as a result of the Mie theory, but according to our Fig. 3 the high g is rather a result of the low density assumed. The snow hydrometeor class is set to have a density of 100 kg m^{-3}, corresponding to an AF $\approx$ 0.9. We can not easily judge the exact impact of this high AF for several reasons, e.g. Geer and Baordo (2014) used a mixing rule not considered by us. Another complication is that the Field et al. (2007) PSD operates with d_m. Hence, also differences in the relationship between particle mass and d_m between the particles affect the data derived by Geer and Baordo (2014). There is a much more intuitive mapping of our findings to bulk properties if the PSD is based on d_e.

Geer and Baordo (2014) analysed only passive observations, while it would be highly beneficial if the representative shape selected also can be applied for radar measurements. Figure 8 indicates that this is the case. The back-scattering of the sector-like snowflake follows its pattern for the scattering efficiency (Fig. 7). This shape has a ratio (as defined in discussed figures) above one up to a somewhat higher size parameter than the other particles, more pronounced at 35.6 GHz than at 94 GHz, but besides this, its properties are of average character also with respect to back-scattering.

7 Is using maximum dimension a better option?

Up to this point, we have compared radiative properties between particles having equal d_e (thus also having the same mass), for reasons discussed in the introduction. The second main measure for the size of individual particles is the maximum dimension, d_m. In fact, there are likely more particle size distributions (PSDs) using d_m than d_e. Hence, it is useful to also understand how the radiative properties vary with d_m, and such an overview for 183 GHz is given in Fig. 10. This figure was produced as Fig. 3, but with d_e replaced by d_m in the definition of size parameter and absorption and scattering efficiencies. The panels for asymmetry parameter in Figs. 3 and 10 are quite similar, besides that the range of x is extended when using d_m. On the other hand, there are clear differences for both absorption and scattering efficiencies. There is a much more compact relationship between d_e and these radiative properties than what is found for d_m. In the case of using d_m as size measure, relatively compact particles (droxtals, plates, columns and spheres) obtain especially high absorption and scattering efficiencies, while particles having high aspect ratios (dendrite and sector-like snowflakes) exhibit especially low efficiencies. The stronger influence of particle morphology and aspect ratio causes that the ratio between highest and lowest efficiency is about ~ 100

(besides for smallest particles). This is in clear contrast to Fig. 3, where the same ratios are around or below 10 when using d_e (Sect. 3.4).

However, the higher variability in absorption and scattering efficiencies is not directly mapped to the same variability in bulk optical properties, i.e., the optical properties of the distribution as a whole. The reason for this is that particles with high aspect ratio have a lower mass as a function of d_m. This aspect deserves careful examination, so we analyse it in the remainder of this section. As a measure for the bulk optical properties we select the scattering extinction coefficient.

As an example of a d_m-based PSD we selected the tropical version of the PSD by Field et al. (2007), below denoted as F07. The extinction coefficients were derived with a setup basically identical to the one described by Geer and Baordo (2014), which also used the F07 PSD: only particles with $d_m \geq 100\,\mu$m were included (as the PSD does not cover smaller particles), and the PSD was rescaled as described in their Appendix C to compensate for the truncation in particle size.

An additional aspect of the Field et al. (2007) size distribution is that it uses two additional input parameters, a and b. They originate from the common way to express the relationship between d_m and particle mass, m, as

$$m = a d_m^b. \tag{11}$$

There are some issues around how to derive a and b for a set of particles, which are discussed in Appendix B of Geer and Baordo (2014). We selected to set the parameters by performing a fit restricted to the particles with $d_m \geq 100\,\mu$m. A reason to ignore the smaller particles in the fit is that for them Eq. (11) may result in $d_m < d_e$ (corresponding to density higher than the one of solid ice) in cases where $b < 3$.

Few d_m-based PSDs take a and b into account. To investigate the impact of this negligence, bulk scattering was also derived with F07 and applying fixed a and b values for all particles, namely $a = 0.069$ and $b = 2$. These are values supported by Wilson and Ballard (1999) and Field et al. (2007). For both fitted and fixed a and b parameters, they were only used when deriving the F07 PSD, the following calculation steps (including rescaling of the PSD) used the actual particle masses from the DDA database.

Since we want to compare d_m-based and d_e-based bulk extinction coefficients, we also need an example of a d_e-based PSD. For this we selected the PSD by McFarquhar and Heymsfield (1997, below MH97). A comparison between F07 and MH97 is found in Fig. 11, where F07 is rescaled to d_e-basis. Two combinations of a and b are considered where the first combination (0.0015/1.55) matches the sector-like snowflakes, having the lowest b among all the particles in the Liu database, and the second combination (480/3) represents solid spheres and thus also the upper limit of b. The rescaling to match specified ice water content has a marginal impact on F07. On the other hand, MH97 puts a much larger fraction of the mass below 100 µm and the rescaling gives a small but not negligible change, therefore this PSD is displayed both before and after the rescaling. Like F07, MH97 is also a PSD targeting tropical conditions, and the agreement with F07 is relatively high for $a = 0.0015, b = 1.55$, while for $a = 480, b = 3$ the two PSDs deviate strongly.

Using the discussed PSDs, bulk scattering extinction coefficients can be calculated by adding up extinction coefficients for individual particles with appropriate weights. Figure 12 shows the results, total extinction coefficients for the two different PSDs, the d_m-based F07 at the top and the d_e-based MH97 at the bottom. For F07, results for fitted and fixed a and b parameters are shown separately by straight and solid lines, respectively.

As the top panel with the F07 results clearly demonstrates, the general pattern seen for the individual particles (Fig. 10) persists in bulk extinction: The more compact particles are at the upper end and the less compact (more "snowflake-like") particles are at the lower end. However, as expected, the ratio between highest and lowest value is decreased, from ~ 100 when considering individual particles to ~ 10 when considering bulk extinction. A similar spread in bulk extinction was obtained by Geer and Baordo (2014, see their Figs. 2 and 3).

Still discussing the top panel of Fig. 12, we now turn to the issue of using fitted or fixed a and b parameters for the F07 PSD. For fixed parameters, the extinction obtained for particular shapes is changed, but the spread of the values is roughly maintained. It should here be noted that keeping a and b fixed only has the consequence that the PSD gets the same basic shape for all particles. The rescaling to ensure that specified mass is matched maintains the relative fraction between particles having different d_m.

While all the discussion so far related to the top panel of Fig. 12, we will now turn to the bottom panel. It shows that particle shape indeed has a much lower impact on bulk scattering for the d_e-based MH97 PSD, compared to the d_m-based F07 PSD. The factor between highest and lowest extinction in case of MH97 is ~ 2.5. This can not be a consequence of that MH97 puts highest weight on completely different particle sizes, as the extinction using MH97 ends up inside the range resulting from F07. Furthermore, the relative variability over the different habits is close to constant with ice water content, for both F07 and MH97, and already Fig. 11 showed that MH97 ends up inside the range covered by F07 when a and b are varied. All in all, F07 and MH97 do a quite similar relative weighting between different particle size ranges. We therefore conclude that the difference in spread seen between upper and lower panel of Fig. 12 is a direct consequence of the fact that the scattering cross-section is more closely linked to d_e than to d_m.

The difference between d_e and d_m, exemplified by Fig. 12, seems to be of general validity for frequencies up to ~ 200 GHz. If anything, the difference increases when going down in frequency (not shown). At higher frequencies a somewhat different pattern is found for the d_m case, as shown in Fig. 13. Here at 340 GHz, the spread in extinction of the different DDA particles is overall lower, compared to Fig. 12, and is particularly low at high ice water content, where it is even smaller than when using d_e. This with the exception of the dendrite snowflake particles, which is maybe an indication that this particular shape should be avoided for higher frequencies. Anyhow, the deviating results for the dendrite snowflake show that the low spread in extinction between the other particles may be a coincidence, not necessarily indicating that using d_m ensures

Discussion Paper | Discussion Paper | Discussion Paper | Discussion Paper |

low uncertainty in extinction for high frequencies and high ice water content. Comparing usage of d_e and d_m at high frequencies is presently complicated by the fact that the Hong database is limited to $d_m \leq 2$ mm, and this size truncation can easily cause artefacts in the comparison.

At the end of this section, we want to briefly mention two more general aspects of the problem to represent bulk particle optical properties. Firstly, our analysis assumed that F07 and MH97 give an equally good representation of the mix of particle sizes. If in situ probes provide better data for either d_e or d_m this should result in higher systematic errors for PSDs based on the more poorly measured particle size.

Secondly, besides possible systematic errors in the PSDs, the variability around average conditions must be considered. For example, it could be the case that there is a lower PSD variation (between locations, day-to-day, etc.) as a function of d_m than as a function of d_e. This situation would decrease, or reverse, the advantage of using d_e. If the opposite was true, that PSDs tend to be more stable in d_e, this would enhance the advantage of selecting d_e in favour of d_m. As far as we know, this important aspect of PSD variability has not been studied so far.

8 Summary and conclusions

We have reviewed the two most established databases of DDA calculations for microwave atmospheric radiative transfer, Liu (2008) and Hong et al. (2009). Nowell et al. (2013) is associated with the Liu database and was also considered. All three databases assume completely random particle orientation. The databases have different frequency coverage, Novel from 10 to 183 GHz, Liu from 3 to 340 GHz, and Hong from 90 to 874 GHz. Liu is the only database providing data for more than one temperature. Scripts to convert the Hong and Liu data to the format expected by the ARTS forward model can be obtained by contacting the authors.

We noted clear systematic differences in absorption between the Hong and Liu databases. The deviations are explained by the fact that the refractive indices are based

on different sources. Hong et al. (2009) used the data from Warren (1984), that now are considered to be outdated. That is, we judge the only easily accessible DDA data above 340 GHz to be inaccurate on particle absorption. In the update of Warren and Brandt (2008), the parameterisation of Mätzler et al. (2006) is recommended for the microwave region, and this is also the source of refractive index used by Liu (2008) and Nowell et al. (2013). Another problematic aspect of the Hong database is the restriction to $d_m \leq 2$ mm.

We mainly compared optical properties between particles having the same mass, and defined the size parameter (x) accordingly (Eq. 2). For small x, below ≈ 0.3, the variation of absorption and scattering between the particles is about 20 % (1.2 ± 0.2 in terms of the ratio used in Figs. 4, 7 and 8). Going towards higher x the variation increases, most quickly for back-scattering, followed by scattering and most slowly for absorption. At higher x, the ratio between lowest and highest value is ~ 10, ~ 5 and ~ 2.5 for those three radiative properties, respectively. The range in scattering is in general generated by the fact that particles of solid types have comparably high scattering, while shapes of "snow" character result in low scattering. Kim (2006) found that solid spheres are representative up to $x = 2.5$ (back-scattering not considered, and clearly allowing some systematic errors), but we, using a larger set of DDA calculations, find that this limit is found somewhere around $x = 0.5$.

We also scrutinised the soft particle approximation (SPA). A first conclusion was that the selection of mixing rule can lead to systematic errors at low x. A mixing rule giving comparably high refractive index, for given air fraction, is needed to avoid this systematic error. We selected the Maxwell–Garnett with ice as matrix and air as inclusion media. With this selection of mixing rule, combined with an air fraction of about 0.25, SPA is applicable up to about $x \approx 0.5$ across the considered frequency range. This gives for absorption and scattering cross-sections a maximum deviation to individual DDA calculations of ≈ 30 %.

On the other hand, usage of SPA at higher x seems problematic. Each individual property calculated by DDA can likely be reproduced by adjusting the air fraction, but it is in general not possible to achieve a fit with several radiative properties simultaneously. Anyhow, even fitting a single property, such as back-scattering, requires that the air fraction is decreased when moving to higher frequencies. Thus, selecting the air fraction based on some standard density parameterisation can in best case only work in a small frequency range. Our results indicate that this frequency range then is found below 35 GHz as this approach leads to high AFs, passing 0.9 at $d_m \sim 1$ mm. At very high frequencies, such as 874 GHz, an air fraction of 0.25 could potentially be applied for all particle sizes, but at lower frequencies the air fraction must also be adjusted with size, from about 0.25 at low x (see paragraph above) to a higher value at higher x, for example, 0.7–0.9 at 90 GHz. That is, applying SPA across the microwave region requires a model with a high number of tuning variables, to give the air fraction the needed variation with frequency and size, while at the same time the resulting particle densities have no physical basis.

Inspired by Geer and Baordo (2014), we investigated also a second way to represent average radiative properties. The idea is simple, if any of the particles covered by the DDA databases exhibits average properties, use this particle shape to represent true habit mixes. Geer and Baordo (2014) compared the particles of the Liu database using real passive observations, but they were then forced to involve assumptions on particle size distribution (PSD) and ice mass concentration, while we mainly compared the basic radiative properties directly. However, some radiative transfer calculations were required to assess how differences in scattering cross-section and asymmetry parameter combine in simulations of downward-looking passive measurements, but these calculations did not involve any additional assumptions. The critical part in our approach is the judgement how representative the different DDA particles are with respect to the mean conditions in the atmosphere.

Due to the lack of reference data, we selected to not push the analysis too far at this point and discussed only in general terms which particle shapes show overall average properties. It is of course possible to use the same methodology to, e.g., select a rep-

resentative shape separately for “cloud ice” and “snow”, or targeting different cloud types.

Interestingly, both Geer and Baordo (2014) and we find that the sector-like snowflake particles, among the shapes found in the Liu database, best represent average properties. This was found valid also for higher frequencies than considered by Geer and Baordo (2014), as well as for application in radar retrievals. For frequencies above 340 GHz, where the selection is restricted to the Hong database, an aggregate model appears to be a suitable choice. However, solid conclusions can not yet be drawn, as the amount of reference data so far is quite limited. More data of optical properties of aggregate and snow-type particles are needed to get a more robust basis for studies like this. In its turn, this requires new algorithms for generating realistic particle models, to be used as input to DDA or similar calculation methods. If new databases are created, the limitations of present databases in temperature, particle size, and frequencies should be avoided.

Besides the “shape model”, we also investigated the representation of particle size. Most importantly, it is demonstrated that there is a much more compact relationship between absorption and scattering properties with mass equivalent diameter (d_e) than with maximum dimension (d_m). With the exception of small x, the spread of absorption and scattering efficiencies is at least a factor of 10 higher when d_m is used to define the size parameter, compared to when using d_e. The difference is decreased when summing up individual values to obtain bulk properties, but using a d_m-based PSD gives still a higher uncertainty in the extinction for a given ice water content compared to using a d_e-based PSD. Below 200 GHz, the uncertainties are roughly a factor 10 and 3 for the d_m and d_e case, respectively. Scattering extinction at 340 GHz shows a somewhat different pattern, and perhaps indicates that the difference between d_m and d_e could vanish at even higher frequencies. In any case, it would be highly beneficial if future in-situ measurement campaigns could target to provide PSDs in terms of d_e, such measurements seem to be much less frequent than ones of d_m.

Finally, we stress that the entire study was performed assuming completely random particle orientation. This is probably the main limitation of the conclusions made above. It can not be ruled out that, e.g., the spread of scattering and the difference between using d_m and d_e is highly dependent on particle orientation. That is, a main consideration for future databases of ice hydrometeor optical properties is to make it possible to study the radiative properties when assuming different distributions of horizontal orientation.

Acknowledgements. Financial support for this study was provided by the Swedish National Space Board. Furthermore, we want to express our high appreciation to the persons behind the publicly available DDA databases. Michael Kahnert, Bengt Rydberg and Manfred Brath are thanked for helpful comments.

References

Austin, R. T., Heymsfield, A. J., and Stephens, G. L.: Retrieval of ice cloud microphysical parameters using the CloudSat millimeter-wave radar and temperature, J. Geophys. Res., 114, D00A23, doi:10.1029/2008JD010049, 2009. 12876

Baran, A. J.: From the single-scattering properties of ice crystals to climate prediction: a way forward, Atmos. Res., 112, 45–69, 2012. 12893

Baran, A. J., Connolly, P. J., Heymsfield, A., and Bansemer, A.: Using in situ estimates of ice water content, volume extinction coefficient, and the total solar optical depth obtained during the tropical ACTIVE campaign to test an ensemble model of cirrus ice crystals, Q. J. Roy. Meteor. Soc., 137, 199–218, 2011. 12876

Bauer, P., Moreau, E., Chevallier, F., and O'keeffe, U.: Multiple-scattering microwave radiative transfer for data assimilation applications, Q. J. Roy. Meteor. Soc., 132, 1259–1281, 2006. 12877

Bennartz, R. and Petty, G. W.: The sensitivity of microwave remote sensing observations of precipitation to ice particle size distributions, J. Appl. Meteorol., 40, 345–364, 2001. 12877

Boukabara, S.-A., Garrett, K., Grassotti, C., Iturbide-Sanchez, F., Chen, W., Jiang, Z., Clough, S., Zhan, X., Liang, P., Liu, Q. Islam, T., Zubko, V., and Mims, A.: A physical approach for a simultaneous retrieval of sounding, surface, hydrometeor, and cryospheric parameters from SNPP/ATMS, J. Geophys. Res., 118, 12–600, 2013. 12876

Brandes, E. A., Ikeda, K., Zhang, G., Schönhuber, M., and Rasmussen, R. M.: A statistical and physical description of hydrometeor distributions in Colorado snowstorms using a video disdrometer, J. Appl. Meteorol. Clim., 46, 634–650, 2007. 12885

Brown, P. R. and Francis, P. N.: Improved measurements of the ice water content in cirrus using a total-water probe, J. Atmos. Ocean. Tech., 12, 410–414, 1995. 12895

Bruggeman, V. D.: Berechnung verschiedener physikalischer Konstanten von heterogenen Substanzen. I. Dielektrizitätskonstanten und Leitfähigkeiten der Mischkörper aus isotropen Substanzen, Ann. Phys. (NY), 416, 636–664, 1935. 12882

Buehler, S. A., Jiménez, C., Evans, K. F., Eriksson, P., Rydberg, B., Heymsfield, A. J., Stubenrauch, C., Lohmann, U., Emde, C., John, V. O., Sreerekha, T. R., and Davis, C. P.: A concept for a satellite mission to measure cloud ice water path and ice particle size, Q. J. Roy. Meteor. Soc., 133, 109–128, doi:10.1002/qj.143, 2007. 12875, 12879, 12889

Buehler, S. A., Defer, E., Evans, F., Eliasson, S., Mendrok, J., Eriksson, P., Lee, C., Jiménez, C., Prigent, C., Crewell, S., Kasai, Y., Bennartz, R., and Gasiewski, A. J.: Observing ice clouds in the submillimeter spectral range: the CloudIce mission proposal for ESA's Earth Explorer 8, Atmos. Meas. Tech., 5, 1529–1549, doi:10.5194/amt-5-1529-2012, 2012. 12879

Cotton, R., Field, P., Ulanowski, Z., Kaye, P. H., Hirst, E., Greenaway, R., Crawford, I., Crosier, J., and Dorsey, J.: The effective density of small ice particles obtained from in situ aircraft observations of mid-latitude cirrus, Q. J. Roy. Meteor. Soc., 139, 1923–1934, 2013. 12895

Davis, C. P., Wu, D. L., Emde, C., Jiang, J. H., Cofield, R. E., and Harwood, R. S.: Cirrus Induced Polarization in 122 GHz Aura Microwave Limb Sounder radiances, Geophys. Res. Lett., 32, L14806, doi:10.1029/2005GL022681, 2005. 12875

Debye, P.: Polar Molecules, The Chemical Catalog Company, Inc., New York, 1929. 12882

Doherty, A., Sreerekha, T., O'Keeffe, U., and English, S.: Ice hydrometeor microphysical assumptions in radiative transfer models at AMSU-B frequencies, Q. J. Roy. Meteor. Soc., 133, 1205–1212, 2007. 12877

Draine, B. T. and Flatau, P. J.: Discrete-dipole approximation for scattering calculations, J. Optical Soc. Am., 11, 1491–1499, 1994. 12877

Draine, B. T. and Flatau, P. J.: User Guide for the Discrete Dipole Approximation Code DDSCAT (Version 5a10), arXiv preprint astro-ph/0008151, 2000. 12884

Emde, C., Buehler, S. A., Davis, C., Eriksson, P., Sreerekha, T. R., and Teichmann, C.: A polarized discrete ordinate scattering model for simulations of limb and nadir longwave measurements in 1D/3D spherical atmospheres, J. Geophys. Res., 109, D24207, doi:10.1029/2004JD005140, 2004. 12895

Eriksson, P., Buehler, S. A., Davis, C. P., Emde, C., and Lemke, O.: ARTS, the atmospheric radiative transfer simulator, Version 2, J. Quant. Spectrosc. Ra., 112, 1551–1558, doi:10.1016/j.jqsrt.2011.03.001, 2011a. 12895

Eriksson, P., Rydberg, B., and Buehler, S. A.: On cloud ice induced absorption and polarisation effects in microwave limb sounding, Atmos. Meas. Tech., 4, 1305–1318, doi:10.5194/amt-4-1305-2011, 2011b. 12875, 12890

Evans, K. F. and Stephens, G. L.: Microwave radiative transfer through clouds composed of realistically shaped ice crystals, Part II. Remote sensing of ice clouds, J. Atmos. Sci., 52, 2058–2072, 1995a. 12875, 12879

Evans, K. F. and Stephens, G. L.: Microwave radiative transfer through clouds composed of realistically shaped ice crystals, Part I: single scattering properties, J. Atmos. Sci., 52, 2041–2057, 1995b. 12890

Evans, K. F., Wang, J. R., O'C Starr, D., Heymsfield, G., Li, L., Tian, L., Lawson, R. P., Heymsfield, A. J., and Bansemer, A.: Ice hydrometeor profile retrieval algorithm for high-frequency microwave radiometers: application to the CoSSIR instrument during TC4, Atmos. Meas. Tech., 5, 2277–2306, doi:10.5194/amt-5-2277-2012, 2012. 12877, 12879

Field, P. R., Heymsfield, A. J., and Bansemer, A.: Snow size distribution parameterization for midlatitude and tropical ice clouds, J. Atmos. Sci., 64, 4346–4365, 2007. 12897, 12898, 12900, 12925, 12926

Galligani, V. S., Prigent, C., Defer, E., Jiménez, C., and Eriksson, P.: The impact of the melting layer on the passive microwave cloud scattering signal observed from satellites: a study using TRMM microwave passive and active measurements, J. Geophys. Res., 118, 5667–5678, doi:10.1002/jgrd.50431, 2013. 12891

Garnett, J. M.: Colours in metal glasses, in metallic films, and in metallic solutions, II, Philos. T. R. Soc. Lond., 237–288, 1906. 12882

Geer, A. J. and Baordo, F.: Improved scattering radiative transfer for frozen hydrometeors at microwave frequencies, Atmos. Meas. Tech., 7, 1839–1860, doi:10.5194/amt-7-1839-2014, 2014. 12877, 12878, 12879, 12897, 12898, 12899, 12900, 12901, 12905, 12906

Gong, J. and Wu, D. L.: CloudSat-constrained cloud ice water path and cloud top height retrievals from MHS 157 and 183.3 GHz radiances, Atmos. Meas. Tech., 7, 1873–1890, doi:10.5194/amt-7-1873-2014, 2014. 12876

Hall, M. P., Goddard, J. W., and Cherry, S. M.: Identification of hydrometeors and other targets by dual-polarization radar, Radio Sci., 19, 132–140, 1984. 12875

Heymsfield, A. and McFarquhar, G.: Mid-latitude and tropical cirrus: Microphysical properties, Cirrus, 78–101, 2002. 12876

Hogan, R. J., Francis, P., Flentje, H., Illingworth, A., Quante, M., and Pelon, J.: Characteristics of mixed-phase clouds, I: lidar, radar and aircraft observations from CLARE'98, J. Molec. Struct., 129, 2089–2116, 2003. 12875

Hogan, R. J., Tian, L., Brown, P. R., Westbrook, C. D., Heymsfield, A. J., and Eastment, J. D.: Radar scattering from ice aggregates using the horizontally aligned oblate spheroid approximation, J. Appl. Meteorol. Clim., 51, 655–671, doi:10.1175/JAMC-D-11-074.1, 2012. 12876, 12893, 12895, 12921

Hong, G.: Parameterization of scattering and absorption properties of nonspherical ice crystals at microwave frequencies, J. Geophys. Res., 112, D11208, doi:10.1029/2006JD008364, 2007. 12886

Hong, G., Yang, P., Baum, B. A., Heymsfield, A. J., Weng, F., Liu, Q., Heygster, G., and Buehler, S. A.: Scattering database in the millimeter and submillimeter wave range of 100-1000 GHz for nonspherical ice particles, J. Geophys. Res., 114, D06201, doi:10.1029/2008JD010451, 2009. 12884, 12886, 12903, 12904, 12914, 12917, 12926

Hufford, G.: A model for the complex permittivity of ice at frequencies below 1 THz, Int. J. Infrared Milli., 12, 677–683, 1991. 12880, 12915

Jiang, J. H. and Wu, D. L.: Ice and water permittivities for millimeter and sub-millimeter remote sensing applications, Atmos. Sci. Lett., 5, 146–151, doi:10.1002/asl.77, 2004. 12880, 12915

Jiménez, C., Buehler, S. A., Rydberg, B., Eriksson, P., and Evans, K. F.: Performance simulations for a submillimetre wave cloud ice satellite instrument, Q. J. Roy. Meteor. Soc., 133, 129–149, doi:10.1002/qj.134, 2007. 12875

Johnson, B. T., Petty, G. W., and Skofronick-Jackson, G.: Microwave properties of ice-phase hydrometeors for radar and radiometers: Sensitivity to model assumptions, J. Appl. Meteorol. Clim., 51, 2152–2171, 2012. 12883

Kahnert, M., Sandvik, A. D., Biryulina, M., Stamnes, J. J., and Stamnes, K.: Impact of ice particle shape on short-wave radiative forcing: a case study for an arctic ice cloud, J. Quant. Spectrosc. Ra., 109, 1196–1218, 2008. 12889

Discussion Paper | Discussion Paper | Discussion Paper | Discussion Paper |

Kim, M.-J.: Single scattering parameters of randomly oriented snow particles at microwave frequencies, J. Geophys. Res., 111, D14201, doi:10.1029/2005JD006892, 2006. 12877, 12889, 12904

Kulie, M. S., Bennartz, R., Greenwald, T. J., Chen, Y., and Weng, F.: Uncertainties in microwave properties of frozen precipitation: implications for remote sensing and data assimilation, J. Atmos. Sci., 67, 3471–3487, 2010. 12877, 12878, 12879

Liao, L., Meneghini, R., Nowell, H. K., and Liu, G.: Scattering computations of snow aggregates from simple geometrical particle models, IEEE J. Sel. Top. Appl., 6, 1409–1417, 2013. 12877, 12888, 12891, 12892

Liebe, H. J., Hufford, G. A., and Cotton, M. G.: Propagation modeling of moist air and suspended water/ice particles at frequencies below 1000 GHz, in: AGARD 52nd Specialists' Meeting of the Electromagnetic Wave Propagation Panel, 1–10 March, Palma de Mallorca, Spain, 1993. 12880

Liu, G.: Approximation of single scattering properties of ice and snow particles for high microwave frequencies, J. Atmos. Sci., 61, 2441–2456, 2004. 12877, 12889, 12894

Liu, G.: A database of microwave single-scattering properties for nonspherical ice particles, B. Am. Meteorol. Soc., 89, 1563, doi:10.1175/2008BAMS2486.1, 2008. 12877, 12884, 12903, 12904, 12914, 12917

Liu, Q., Xue, Y., and Li, C.: Sensor-based clear and cloud radiance calculations in the community radiative transfer model, Appl. Optics, 52, 4981–4990, 2013. 12876

Mätzler, C.: Thermal microwave radiation: applications for remote sensing, IET electromagnetic waves series, Institution of Engineering and Technology, 52, ISBN 9780863415739, 2006. 12881, 12885, 12904, 12915, 12917

McFarquhar, G. M. and Heymsfield, A. J.: Parameterization of tropical cirrus ice crystal size distribution and implications for radiative transfer: results from CEPEX, J. Atmos. Sci., 54, 2187–2200, 1997. 12901, 12925, 12926

Meirold-Mautner, I., Prigent, C., Defer, E., Pardo, J. R., Chaboureau, J.-P., Pinty, J.-P., Mech, M., and Crewell, S.: Radiative transfer simulations using mesoscale cloud model outputs: comparisons with passive microwave and infrared satellite observations for midlatitudes, J. Atmos. Sci., 64, 1550–1568, 2007. 12877

Millán, L., Read, W., Kasai, Y., Lambert, A., Livesey, N., Mendrok, J., Sagawa, H., Sano, T., Shiotani, M., and Wu, D. L.: SMILES ice cloud products, J. Geophys. Res., 118, 6468–6477, doi:10.1002/jgrd.50322, 2013. 12876, 12879

Mishchenko, M. I., Travis, L. D., and Mackowski, D. W.: T-matrix computation of light scattering by nonspherical particles: a review, J. Quant. Spectrosc. Ra., 55, 535–575, doi:10.1016/0022-4073(96)00002-7, 1996. 12876

Mishima, O., Klug, D. D., and Whalley, E.: The far-infrared spectrum of ice Ih in the range 8–25 cm^{-1}, sound waves and difference bands, with application to Saturn's rings, J. Comp. Phys., 78, 6399–6404, doi:10.1063/1.444700, 1983. 12880

Nowell, H., Liu, G., and Honeyager, R.: Modeling the microwave single-scattering properties of aggregate snowflakes, J. Geophys. Res., 118, 7873–7885, doi:10.1002/jgrd.50620, 2013. 12877, 12884, 12885, 12888, 12903, 12904, 12914, 12917

Petty, G. W. and Huang, W.: Microwave backscatter and extinction by soft ice spheres and complex snow aggregates, J. Atmos. Sci., 67, 769–787, 2010. 12884

Rydberg, B., Eriksson, P., Buehler, S. A., and Murtagh, D. P.: Non-Gaussian Bayesian retrieval of tropical upper tropospheric cloud ice and water vapour from Odin-SMR measurements, Atmos. Meas. Tech., 2, 621–637, doi:10.5194/amt-2-621-2009, 2009. 12876, 12879

Schmitt, C. G. and Heymsfield, A. J.: Observational quantification of the separation of simple and complex atmospheric ice particles, Geophys. Res. Lett., 41, 1301–1307, 2014. 12893

Sihvola, A.: Mixing rules with complex dielectric coefficients, Journal of Subsurface Sensing Technologies and Applications, 1, 393, doi:10.1023/A:1026511515005, 2000. 12882

Skofronick-Jackson, G. M., Gasiewski, A. J., and Wang, J. R.: Influence of microphysical cloud parameterizations on microwave brightness temperatures, IEEE Geosci. Remote S., 40, 187–196, 2002. 12877

Tyynelä, J. and Chandrasekar, V.: Characterizing falling snow using multifrequency dual-polarization measurements, J. Geophys. Res., 119, 8268–8283, doi:10.1002/2013JD021369, 2014. 12884

Warren, S.: Optical constants of ice from the ultraviolet to the microwave, Appl. Optics, 23, 1206–1225, doi:10.1364/AO.23.001206, 1984. 12880, 12882, 12886, 12904, 12915

Warren, S. G. and Brandt, R. E.: Optical constants of ice from the ultraviolet to the microwave: A revised compilation, J. Geophys. Res., 113, D14220, doi:10.1029/2007JD009744, 2008. 12881, 12904, 12915

Wilson, D. R. and Ballard, S. P.: A microphysically based precipitation scheme for the UK Meteorological Office Unified Model, Q. J. Roy. Meteor. Soc., 125, 1607–1636, 1999. 12900

Wu, D. L., Jiang, J. H., Read, W. G., Austin, R. T., Davis, C. P., Lambert, A., Stephens, G. L., Vane, D. G., and Waters, J. W.: Validation of the Aura MLS cloud ice water content measurements, J. Geophys. Res., 113, D15S10, doi:10.1029/2007JD008931, 2008. 12876, 12879
Wu, D. L., Lambert, A., Read, W. G., Eriksson, P., and Gong, J.: MLS and CALIOP cloud ice measurements in the upper troposphere: A constraint from microwave on cloud microphysics, J. Appl. Meteorol. Clim., 53, 157–165, doi:10.1175/JAMC-D-13-041.1, 2014. 12890
Zhang, C., Lee, K.-S., Zhang, X.-C., Wei, X., and Shen, Y.: Optical constants of ice Ih crystal at terahertz frequencies, Appl. Phys. Lett., 79, 491–493, doi:10.1063/1.1386401, 2001. 12880, 12915
Zhao, L. and Weng, F.: Retrieval of ice cloud parameters using the Advanced Microwave Sounding Unit, J. Appl. Meteorol., 41, 384–395, 2002. 12876

Table 1. Overview of considered DDA databases.

Database	Frequency range [GHz]	Temperatures [K]	Particle sizes [µm, max. dim.]	Particle shapes
Liu (2008)	3.0–340	233, 243, 253, 263 and 273	50–12 454	Columns, plates, rosettes, sector and dendrite snowflakes.
Nowell et al. (2013)	10.65–183.31	263	200–12 584	Three aggregate types, consisting of 200 and/or 400 µm 6-bullet rosettes.
Hong et al. (2009)	90–874	243	2–2000	Solid and hollow columns, plates, 6-bullet rosettes, droxtals and one type of aggregate.

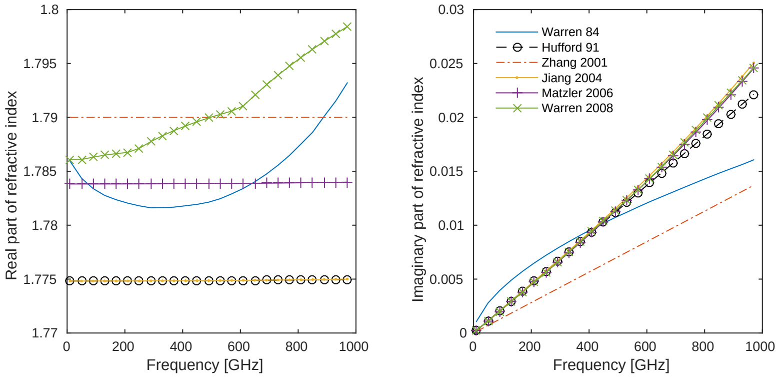

Figure 1. Real (left) and imaginary (right) part of the refractive index of pure ice, as a function of frequency, according to Warren (1984), Hufford (1991), Zhang et al. (2001), Jiang and Wu (2004); Mätzler et al. (2006) and Warren and Brandt (2008). The temperature is set to 266 K.

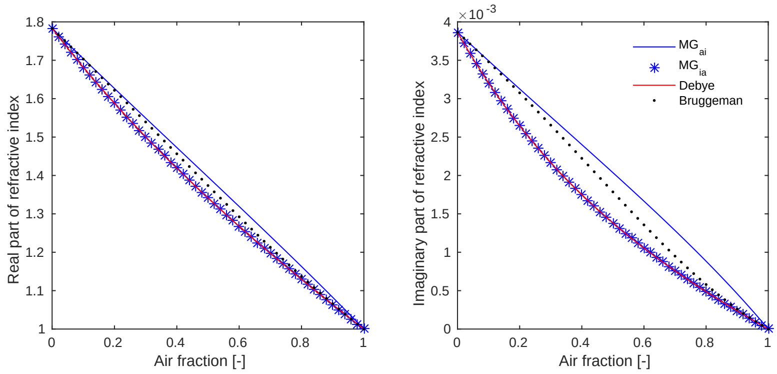

Figure 2. Real (left) and imaginary (right) part of the effective refractive index of a mixture of ice and air, as a function of air volume fraction according to some mixing rules. The refractive index of ice at 183 GHz and 263 K, $n_{ice} = 1.7831 + i0.0039$, was used, and the refractive index of air was set to $n_{air} = 1 + i0$.

Discussion Paper | Discussion Paper | Discussion Paper | Discussion Paper |

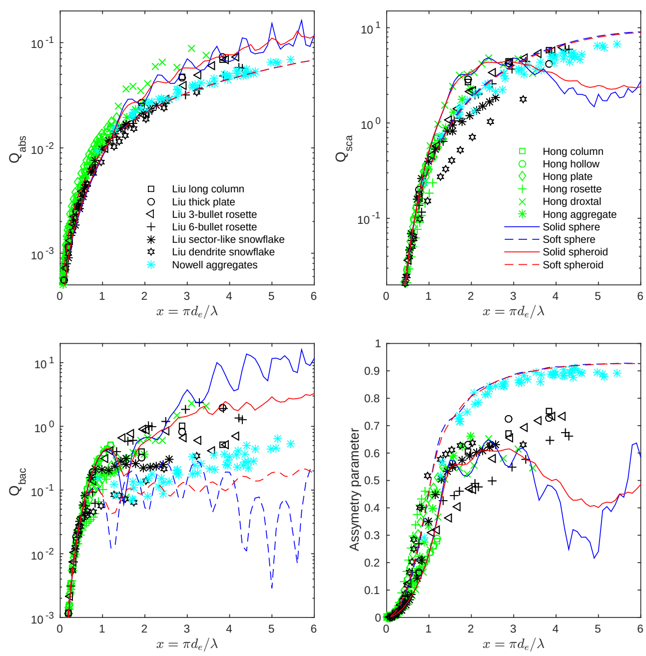

Figure 3. DDA-based single scattering properties at 183 GHz from the databases of Liu (2008); Nowell et al. (2013) and Hong et al. (2009). Absorption, scattering and back-scattering efficiencies (Eq. 10) and asymmetry parameter are displayed. The combined legends are valid for all panels. The figure includes also data of solid and soft spheres and spheroids, with refractive index following Mätzler et al. (2006). The soft particles have an air fraction of 0.75, with the effective refractive indices derived by the MG_{ai} mixing rule. The spheroids are oblate with an aspect ratio of 1.67. All results are valid for 183 GHz and 243 K, except Nowell et al. (2013) that are for 263 K.

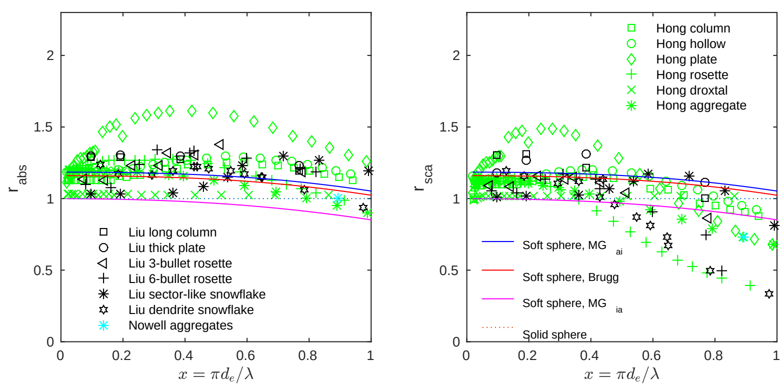

Figure 4. Absorption (left) and scattering (right) cross-sections of DDA data and soft spheres at 183 GHz. The cross-sections are reported as the ratio to the corresponding cross-section of the equivalent mass sphere, with the same refractive index as used for the preparation of the DDA data. That is, the dotted straight line at $r = 1$ represents solid ice spheres. Database source and particle shapes of the DDA data are found in figure legends (same as in Fig. 3). The soft spheres have an air fraction of 0.25, where results for three different mixing rules (MG_{ia}, Bruggeman and MG_{ia}) are included (solid lines).

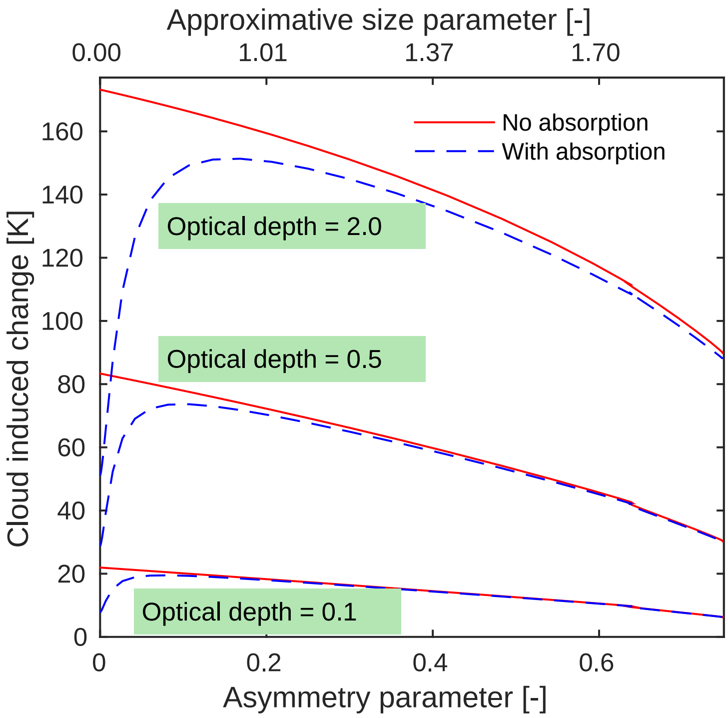

Figure 5. Test of importance of absorption and asymmetry parameter for passive microwave radiative transfer. The brightness temperature deviation from simulations with no cloud layer is reported. The stated optical depths refer to the zenith extinction of the cloud layer. For solid lines, the imaginary part of the refractive index was set to zero, resulting in no cloud particle absorption. The simulations are described further in the text.

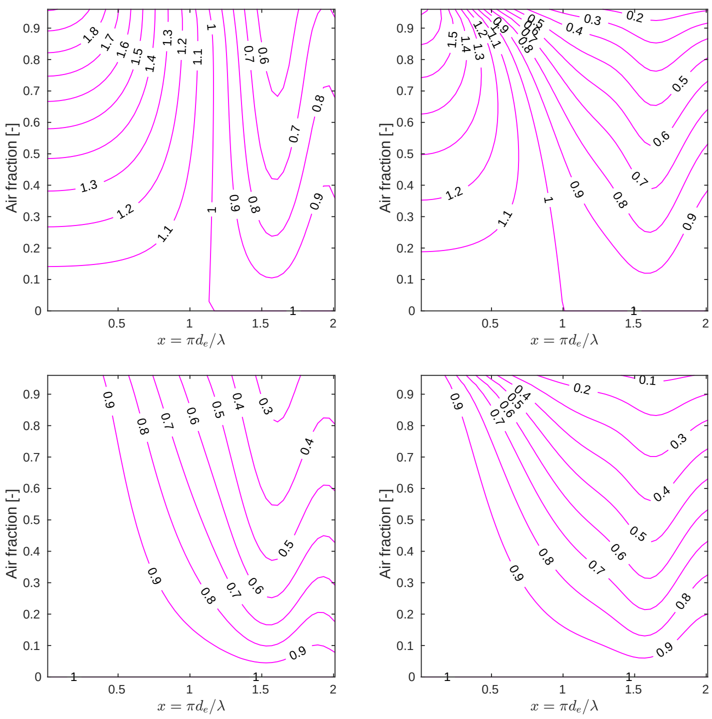

Figure 6. Absorption (left) and scattering (right) cross-sections of soft spheres (183 GHz and 243 K), normalised by the equivalent mass ice sphere absorption or scattering cross-section as in Fig. 4, as a function of size parameter and air fraction. The two top panels are calculated using the MG_{ai} (air in ice) mixing rule, while the two lower panels are calculated using the MG_{ia} (ice in air) mixing rule.

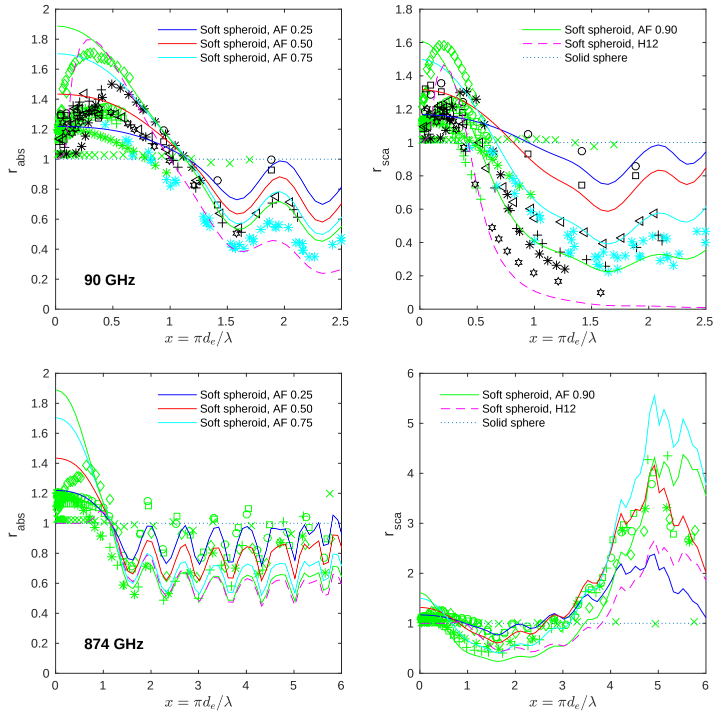

Figure 7. Normalised absorption (left) and scattering (right). The top row includes 90 GHz Hong/Liu and 89 GHz Nowell data, while the bottom row covers 874 GHz. The soft spheroids have either a fixed air fraction (AF) or follow Hogan et al. (2012), denotes as H12. Normalisation and plotting symbols used for DDA data as in Fig. 4.

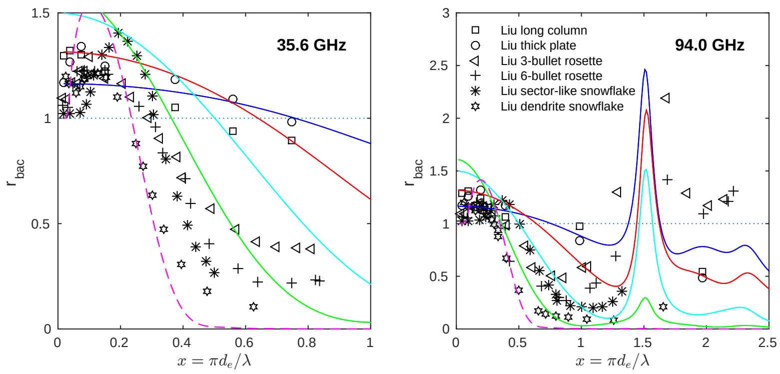

Figure 8. Normalised back-scattering of the Liu particles at two frequencies. As in Figs. 4 and 7, the normalisation is performed with respect to the back-scattering cross-section of the solid sphere having the same mass. For 94 GHz and $x \approx 1.5$ some data points have a ratio above 3, partly due to a minimum of the solid sphere back-scattering at that size parameter. Solid and dotted lines are the same as in Fig. 7.

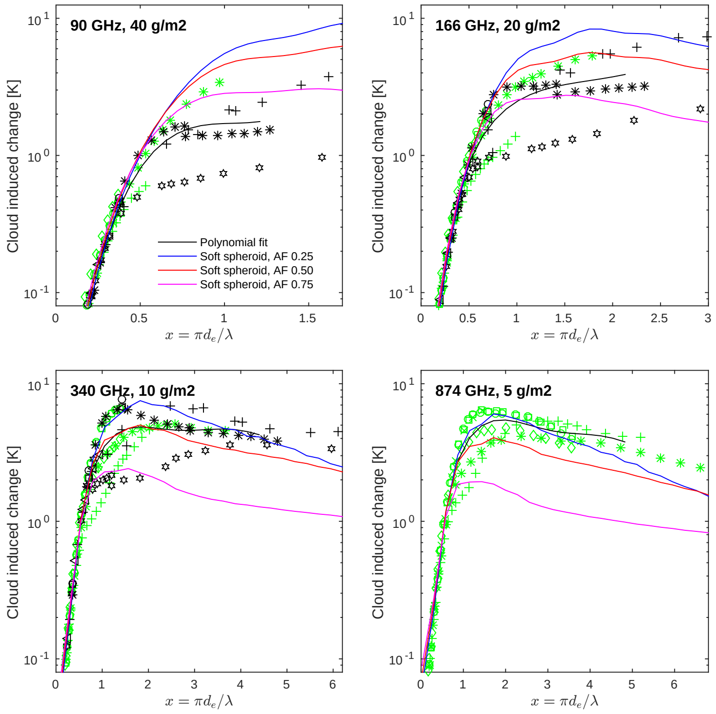

Figure 9. Radiative transfer simulations at different frequencies. General conditions as in Fig. 5, i.e. a 2 km thick cloud layer at 10 km is simulated. A single particle type is included in each simulation where the number density was adjusted to obtain the stated ice water paths. The black solid line is a high-order polynomial fit of the DDA-based results, while other lines are results for soft spheroids with constant air fraction (AF).

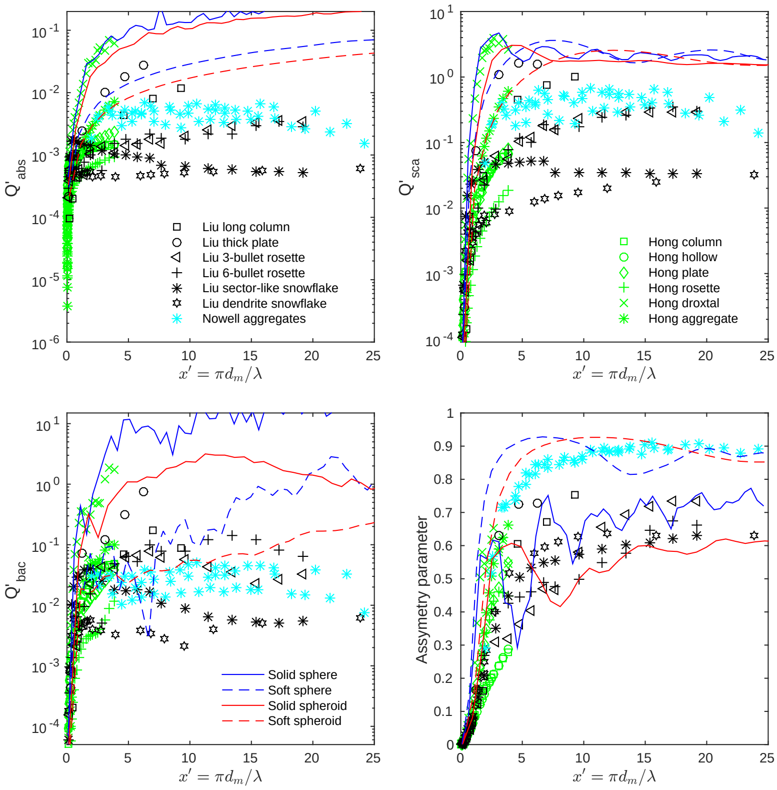

Figure 10. As Fig. 3, but using the maximum dimension (d_m) as characteristic size. That is, the size parameter is here defined as $x' = \pi d_m/\lambda$ and absorption and scattering efficiencies are defined as $Q' = (4\sigma)/(\pi d_m^2)$. As in Fig. 3, the frequency is 183 GHz.

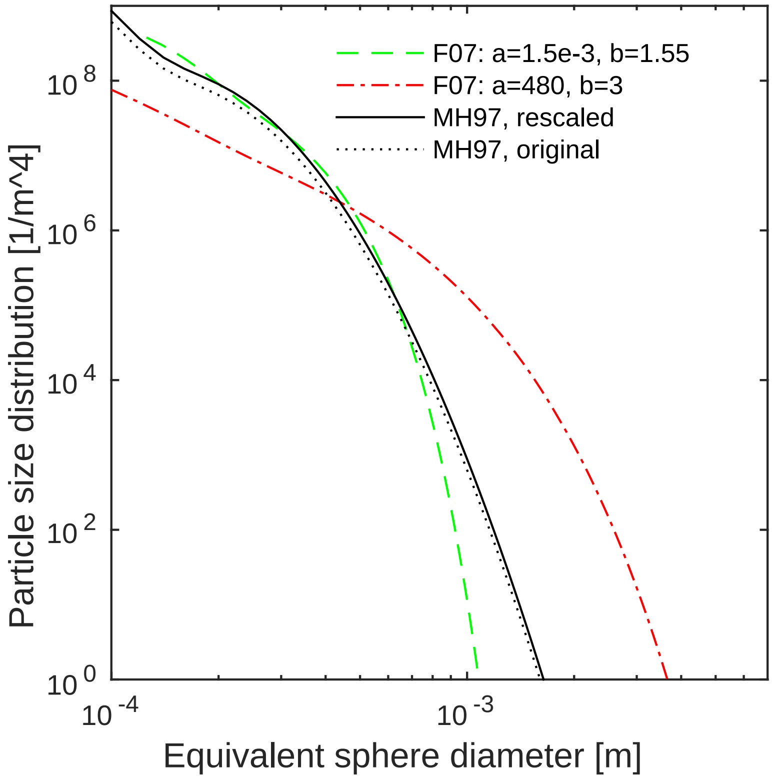

Figure 11. Ice particle size distributions for 0.1 g m^{-3}, according to Field et al. (2007, F07) and McFarquhar and Heymsfield (1997, MH97). The F07 PSD is converted from d_m to d_e for two combinations of *a* and *b* (Eq. 11).

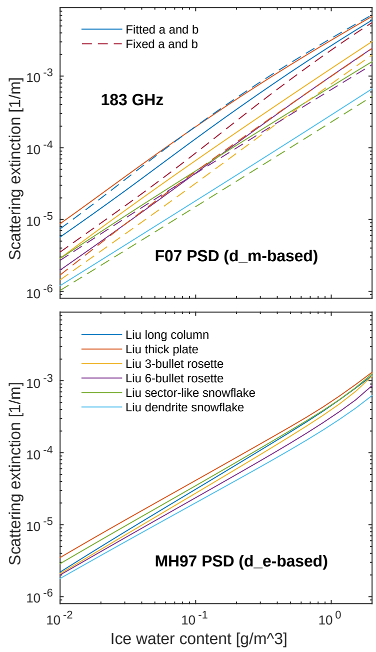

Figure 12. Scattering extinction as a function of ice water content at 183 GHz, for some of the particles of the Hong et al. (2009) DDA database. The particle size distribution applied in the upper and lower panels is F07 (Field et al., 2007) and MH97 (McFarquhar and Heymsfield, 1997), respectively. Dashed lines in the upper panel show results for the F07 distribution with fixed $a = 0.069$ and $b = 2$.

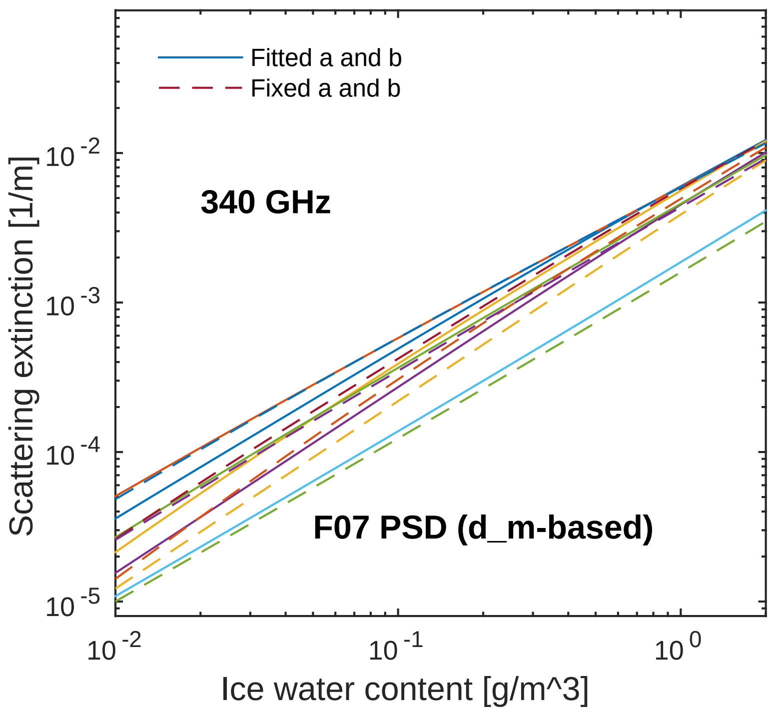

Figure 13. As Fig. 12, but for 340 GHz. The results for MH97 are not shown as they show the same general pattern as in Fig. 12 (just shifted in mean level in same way as the results for F07).